Université catholique de Louvain
Ecole Polytechnique de Louvain
Institute of Condensed Matter and Nanosciences (IMCN)
Bio- and Soft Matter (BSMA)

Electrical and Structural Properties of Nano-imprinted Ferroelectric Polymers

Hailu Gebru Kassa

Supervisor: Prof. Alain M. Jonas

Thesis submitted in partial fulfilment of the
requirements for the degree of
Docteur en Sciences de l'ingénieur

May 2014

Université catholique de Louvain
Ecole Polytechnique de Louvain
Institute of Condensed Matter and Nanosciences (IMCN)
Bio- and Soft Matter (BSMA)

Electrical and Structural Properties of Nano-imprinted Ferroelectric Polymers

Hailu Gebru Kassa

Dissertation Jury:

Prof. Alain M. Jonas (UCL), supervisor
Prof. Bart Goderis (KUL), member
Prof. Bernard Nysten (UCL), member
Prof. Jacques Devaux (UCL), President
Prof. Jean-Pierre Raskin (UCL), member
Prof. Philippe Ghosez (ULG), member

Summary

Silicon and other inorganic materials are the most developed and used materials for applications in the area of electronic memory technology. Recently, organic electronics has been able to find some complementary roles, that silicon based integrated circuits cannot reach, like in areas where flexibility and price matter more than performance. Furthermore, the molecular structures of polymer materials can be changed easily to tune the macroscopic properties. Here, we studied ferroelectric polymers that can be used to fabricate cheap, flexible, and low voltage nonvolatile memory devices. Interestingly, the physical properties of nano-confined polymers can be significantly different from the bulk. In this context, crystallizing ferroelectric polymers in the cavities of nano-imprinting molds was found to enhance the ferroelectric performance of copolymers like those based on vinylidene fluoride and trifluoroethylene, P(VDF-TrFE). The exact reason for this effect was however not fully elucidated. The objectives of this thesis were then to make progress into this issue by investigating the correlation between the material, the nanoconfinement process, and subsequent structural or ferroelectric properties.

First, we have fabricated, as part of this thesis work, nano-imprinting hard molds of different size and shape by electron beam lithography (EBL), followed by lift-off and reactive ion etching procedures. The depth of the cavities was controlled during the etching process.

Then, we used the hard molds to produce confined nanoobjects of different shape, height, and lateral dimensions by nano-imprint lithography (NIL). The

structural properties of the resulting nano-patterns were studied using Fourier transform infrared spectroscopy (IR) and atomic force microscopy (AFM), whereas the local ferroelectric properties were monitored by piezoresponse force microscopy (PFM); the latter technique was studied in more details, being an important tool for our work. We observe that nano-processing conditions like imprinting temperature, size and shape of mold cavities, and presence or not of a thin residual layer between the pillars are very critical in determining both the structural and electrical properties of P(VDF-TrFE) in the resulting nanostructures.

Finally, we compare the thermal behavior of fully confined nanodots to those of continuous thin films and bulk samples of P(VDF-TrFE) by PFM. Our results show that the thermal stability is well preserved for fully confined nanodots with dimensions and height in the range of few tens of nanometer only, demonstrating no significant difference. To summarize, our findings indicate the complexity of the effect of nano-confinement on the structure and properties of P(VDF-TrFE), and provide useful practical insights for the realization of high density non-volatile ferroelectric memories.

Table of Contents

Acknowldegments

First and foremost I would like to express my thanks to Prof. Alain Jonas, my advisor, for giving me this opportunity to carry out PhD under his supervision. This PhD thesis would not have been possible without his time, effort, and support. More importantly, the enthusiasm he has for his research and his optimistic attitude have been a great inspiration for me.

I would like to thank Prof. Bernard Nysten for his support during my experimental works on PFM. I would like to thank Mr. Andre Crahay, Mr. Christian Renaux, Dr. Romain Delamare, and Mr. Mathieu Vanden Bulcke for their constant support in the cleanroom facility of UCL. I would like to also thank my colleagues at BSMA, but I do not want to risk missing someone by listing all individually. It has been a great experience and a pleasure to work with all members of the lab both in terms of research and daily life. I also have to thank the members of my PhD committee for their helpful advice and suggestions.

Finally, I would like to thank my families who have always been on my side throughout my study period.

Abbreviations

AFM	Atomic force microscopy
BCL	Block copolymer lithography
E_c	Coercive field
CMOS	Complementary metal-oxide-semiconductor
T_c	Curie temperature
DSC	Differential scanning calorimetry
DRAM	Dynamic random access-memory
EBL	Electron beam lithography
FeFET	Ferroelectric field-effect transistor
FeRAM	Ferroelectric random access memories
FTIR	Fourier transform infrared spectroscopy
IC	Integrated circuit
IPA	Isopropyl alcohol
KAI	Kolmogorov-Avrami-Ishibashi model
PZT	Lead zirconium titanate
MRAM	Magnetoresistive random access-memory
T_m	Melting temperature
MIBK	Methyl isobutyl ketone
NIL	Nano-imprint lithography
PDA	Personal digital assistants
PFM	Piezoresponse force microscopy
PHL	Piezoresponse hysteresis loop
P3HT	Poly(3-hexylthiophene)
PMMA(8.5)MAA	poly(methylmetacrylate-co-methylacrylic acid)

PS-b-P4VP	Poly(styrene-b-4-vinylpyridine)
PVDF	Poly(vinylidene fluoride)
P(VDF-TrFE)	Poly(vinylidene fluoride-*ran*-trifluoroethylene)
PMMA	Polymethyl methacrylate
PF_3E	Polytrifluoroethylene
RAM	Random-access memory
P_r	Remanent polarization
$NaKC_4H_4O_6.6H_2O$	Rochelle salt
SEM	Scanning electron microscopy
SPM	Scanning probe microscopy
SNR	Signal-to-noise ratio
SiO_2	Silicon oxide
P_s	Spontaneous polarization

Chapter 1

Introduction

A device or recording medium that retains retrievable digital data over a time interval is referred to as a memory. It is one of the basic components of all modern computers and electronic systems. There is an ever increasing demand on increasing the storage capacity of memory devices, while decreasing their energy payload. For example, personal wireless connectivity applications that are battery driven, such as cellular phones and personal digital assistants (PDA), demand large amounts (multiple megabytes) of non-volatile storage to retain accessed Internet Web pages, voice, and data. The need for high density and energy efficient data writing and reading is one of the factors driving the availability of better performing memory devices in the market. At the same time the memories should be light, robust, low-power and low-cost. Currently, conventional memories which are semiconductor-based integrated circuits, such as transistors and capacitors, are used in electronic systems [1]. However, it is now becoming increasingly costly to scale down and increase the efficiency of existing memory devices based on semiconductors [2]. Therefore, other types of memory devices are emerging, not based on the current memory technologies

which make use of memory effects associated with a special cell structure. The new technologies are based on bi-stability of materials arising from changes in certain intrinsic properties, such as magnetism, polarity, phase, and conformation in response to an applied electric or magnetic field.

Organic electronics is emerging as an active research topic in recent years. Polymer materials are promising candidates for future molecular-scale memory applications. Thus, polymer memories have the potential to be an alternative or supplementary technology to the silicon based memory technology [3]. It has been demonstrated that individual or small packets of molecules, mounted within addressable orientations, can conduct and switch electrical currents, and can retain electrical bits of information [4]. Simplicity in device structure, good scalability, low-cost potential, low-power operation, 3D stacking capability and large capacity for data storage are some of the advantages of polymer memories [5-10].

Superior features such as short programming time and low power consumption are the two main reasons for interest in non-volatile ferroelectric random access memories (FeRAM) [11]. Ferroelectric materials are those belonging to a special class of dielectrics which have a spontaneous electrical polarization. The polarization of these materials can be reversed by an external electric field [12]. A ferroelectric crystal such as $Pb(Zr,Ti)O_3$ maintains a permanent electric polarization that can be repeatedly switched between two stable states by an external electric field [13]. This bi-stability is ideal to make a non-volatile memory. Nowadays, inorganic ferroelectric crystals of perovskite structures are commonly used for FeRAMs. The difficulty and higher cost of their processing makes their use not easy for micro- or nano-electronic applications. In contrast, ferroelectric polymers such as poly(vinylidene fluoride) and its copolymers with

trifluoroethylene, P(VDF-TrFE), hereafter denoted as P(VDF-TrFE), do not suffer from these limitations [1]. Unfortunately, these ferroelectric polymers exhibit a relatively low melting point (150–200^{o}C), low stiffness, and the polymorphous structure of solvent-processed samples [14, 15]. Nevertheless, they offer the possibility to fabricate highly flexible, low cost and easily producible memories which are attractive for applications in all-organic flexible electronics.

However, reasonable ferroelectric parameters which are critical for the realization of polymer FeRAMs are not yet obtained. For example, the coercive field of P(VDF-TrFE) (~50 MV/m) is higher by an order of magnitude than typical values for ferroelectric oxide materials [15]. Recently, our group in UCL used nano-imprint lithography (NIL) to fabricate high-density arrays of ferroelectric polymer cells [16]. NIL is a hot-melt embossing process where the mold is placed in contact with a spin-coated film of PVDF; after evacuation, the polymer is molten and the mold pressed into the film under pressure. The mold cavities fill, and the polymer is cooled down and crystallizes within the nano-cavities of the mold. By using nano-imprint lithography, patterns down to a few tens of nanometres can be imprinted (Figure 1.1) [17, 18].

In our group's study, the coercive field was found to decrease by a factor of 5 and the orientation of the chain axis (or *c*-axis) was aligned parallel to the substrate, easing the switching of the polarization. Even though this study is promising, the details of NIL and the reasons for the dramatic improvement of performance after nano-imprinting are not fully understood. Moreover, no attempt was performed to tune the structure of the ferroelectric polymer by playing with processing parameters or chain structure, and to check its effect on

the efficiency of ferroelectric memories, although it is known that such parameters are critical [19, 20].

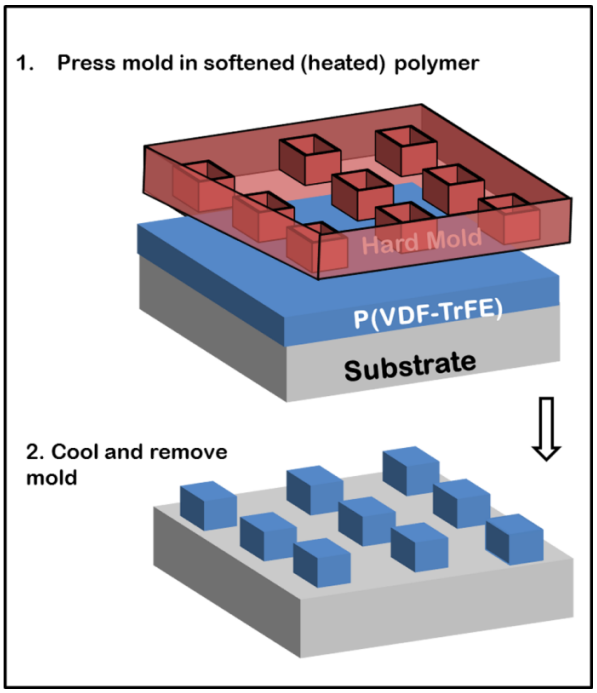

Figure 1.1: Scheme of nano-imprint lithography (NIL) procedure.

For example, the composition of PVDF copolymer, optimum processing conditions and different external variables like temperature and pressure could be controlled. Most importantly, the exact reasons for the dramatic improvement of performance after nano-imprinting are not yet known. This thesis aims precisely at providing answers to these issues.

Chapter 1

Objective of the Thesis

In this frame, the objective of this thesis was then at making the link between the different material/processing variables and the ferroelectric properties of poly(vinylidene fluoride) copolymers. This link will be made for thin films and nano-imprinted PVDF samples. In this context, the processing conditions and film structure are manipulated to study their effect on the morphology and ferroelectric properties of the material. Furthermore, in order to control ferroelectricity at a very local scale, we develop methods to measure ferroelectric properties at this scale. As stated above, increasing the crystalline perfection and orientation of ferroelectric domains by nano-imprinting provides interesting properties. However, measuring them is a real technological challenge, since each nano-cell has a side on the order of 300 nm or below and lies in a larger array containing typically a few hundred cells, which requires finding a way to measure their collective behaviour. The classical ferroelectric characterization techniques of the Sawyer - Tower circuit [21] and the switching current technique [22] are not applicable to study imprinted nanostructures. The development of ferroelectric characterization techniques for the nano-patterns is thus also one of the objectives of our study.

The other objective of this thesis was to study the thermal stability of the nanostructures produced by NIL. In other words, investigating the impact of temperature on the ferroelectric properties of nanostructures compared with thin and bulk films will be done. The reported decrease on the coercive field of imprinted nanostructures should be monitored at higher temperatures and the ferroelectric transition temperature measured. The results obtained in this thesis will be useful for other projects led in our laboratory, aiming at fabricating non-

volatile memory devices based on diode and transistors from mixed nanoimprinted ferroelectric P(VDF-TrFE) polymers and semiconducting layers.

Methodology

The general methodology of this work is given in Figure 1.2. We essentially play with the processing parameters (which include the pressure and geometrical constraints imposed by the nano-imprinting process), and characterize the resulting microstructure by a range of techniques. The ferroelectric and structural properties are investigated in parallel, in order to obtain a general picture of ferroelectric properties of nano-imprinted P(VDF-TrFE) films. This knowledge about the contribution of NIL processing parameters on the ferroelectric properties and the thermal stability of imprinted P(VDF-TrFE) is of direct interest for the fabrication of ferroelectric-based memory devices. In the following paragraphs, we present more details on some of these strategies.

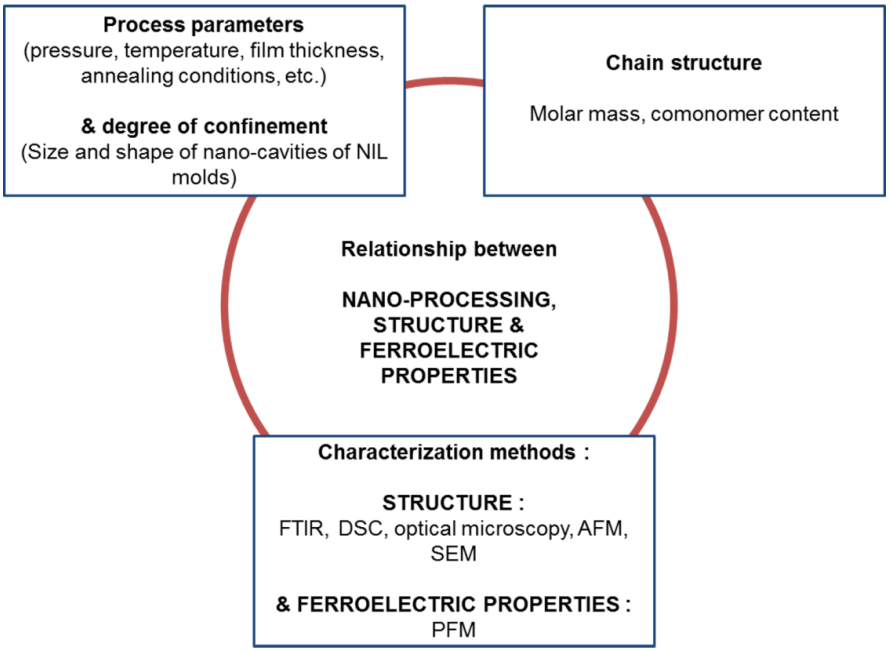

Figure 1.2: General scheme and strategy of the thesis.

1. Nano-imprinting processing conditions. Here, essentially the temperature of annealing during or after imprinting is investigated. The nature of the substrate will be also investigated in a restricted range, mainly bare silicon oxide and amino-propyl silanized silicon wafers, surfaces which can hydrogen-bind to the fluorine atoms of PVDF thereby ensuring proper adhesion. Among the processing parameters, the effect of nano-confinement is studied in detail. Examples of the parameters that were initially planned to explore are given in Figure 1.3. As will be shown, only some of these structures could be realized. The imprinting molds are produced by electron-beam lithography using standard lift-off and etching techniques.

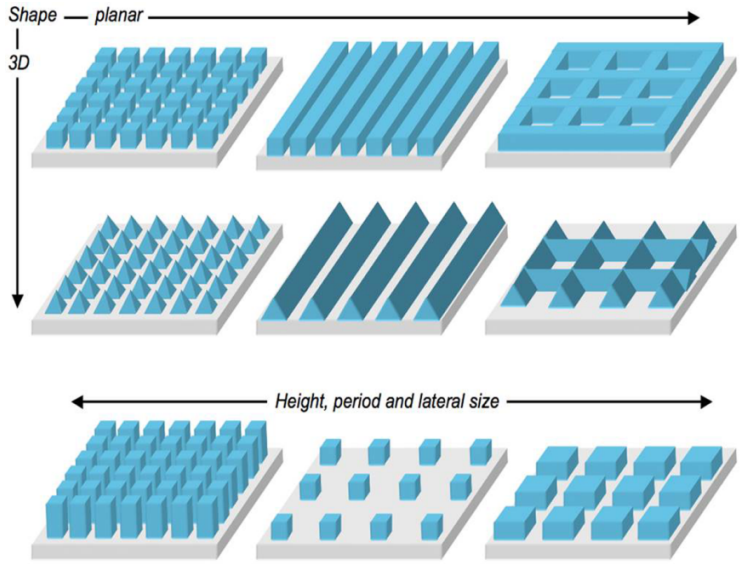

Figure 1.3: Some geometries of nanocells that were initially proposed for this study.

Another interesting parameter that has to be controlled is the residual film thickness, i.e., the thickness of the film that remains between the surface of the substrate and the topmost part of the mold, when the mold is fully pressed in the film. It is known that this residual thickness has a critical role to play when crystallizing polymers in nano-confinement [23].

2. Characterization techniques.

a. Structure. The effect of the aforementioned parameters and processes on the morphology of the material is studied one by one. Explicitly, the surface of

continuous thin films and arrays of nanostructures is imaged by atomic force microscopy (AFM). To further study the preferential orientation of P(VDF-TrFE) chains Fourier transform infrared (IR) is used. From the knowledge of IR bands, we can study the interaction of the transition dipole moments with an applied electric field, which provides information on the orientation of the chains and thus on the crystal orientation. Scanning electron microscopy (SEM) is used to inspect the fabrication of imprinting hard molds by electron beam lithography (EBL).

b. Ferroelectric properties. As explained earlier this part is one of the technological challenges. Here, we use piezoresponse force microscopy (PFM) to get information about the local polarization. PFM is based on an AFM system, where a conductive metal-coated silicon cantilever tip is placed in contact with the sample surface area to measure the electromechanical response. By applying a biased voltage on the AFM tip, the topography, PFM amplitude and PFM phase images of ferroelectric samples can be acquired simultaneously. The magnitude of the AFM cantilever deflection reflects the local electromechanical response of the sample surface. On the other hand, the phase shifts between the applied a.c. voltage and cantilever oscillation yields information about the local polarization direction below the AFM tip. By this way, it is also possible to compare ferroelectric properties of imprinted nanostructures and continuous thin films of different samples. Using PFM, it is also possible to make piezoresponse hysteresis loops (PHL's) which reflect the switching behaviour of the average dipole moment underneath the polarized tip. From the knowledge of PFM switching conditions, it is then possible to obtain important characteristics such as coercive voltage and work of switching [24, 25]. The thermal stability of the ferroelectric storage in nano-imprinted structures is also evaluated by PFM. Initially, the ferroelectric samples are poled by a polarized bias. Subsequently, the sample is heated progressively. In this way, the ferroelectric response of the heated nanostructures

can be compared with the differential scanning calorimetry (DSC) thermogram of the bulk P(VDF-TrFE) copolymers.

To summarize, these experimental techniques enable us to understand better the effect of nano-confinement on both structure and properties of ferroelectric polymers. The improved ferroelectric parameters and best processing conditions can then be used to realize polymer memories like non-volatile memory diodes. This thesis is divided into six chapters:

The **second chapter** gives an overview of organic electronics with particular attention to organic ferroelectric materials. The properties and applications of polymers with particular attention to (PVDF-TrFE), the material used in this thesis, are summarized. Advantages of ferroelectric polymers over inorganic ones are described. A review of the advances made in ferroelectric-based organic memories is also given.

The **third chapter** presents the methods of fabrication and characterization of arrays of nanostructures. The fabrication step starts by producing imprinting hard molds using electron beam lithography (EBL). Fabrication of P(VDF-TrFE) nano-patterns by nano-imprint lithography (NIL) follows using the hard molds made by EBL. These fabrication steps are supported by AFM and SEM images where necessary. Then the structural and ferroelectric characterization techniques are presented with special focus on piezoresponse force microscopy (PFM), which was developed for the first time in our laboratory in the frame of this thesis.

In chapter 4, the effect of nano-processing conditions on the structural and ferroelectric properties of P(VDF-TrFE) is presented in detail. Arrays of nanopatterns of P(VDF-TrFE) copolymers with different size and shape that are produced by NIL are compared with continuous thin films. The influence of

imprinting temperature, initial film thickness, size, and shape on the structural properties is first detailed. Then, the study of the ferroelectric properties of these samples by PFM follows. A correlation between the microstructure and ferroelectric performances is also described.

In **Chapter 5** the thermal stability of imprinted nano-cubes is compared with the bulk sample. Specifically, the Curie transitions of the confined nanostructures with lateral sizes from 500 nm up to nano-pillars of lateral size below 100 nm are studied using the PFM technique. Imprinted and continuous ultrathin films of P(VDF-TrFE) are heated successively and the resulting ferroelectric properties are investigated in comparison with the thermal history of bulk P(VDF-TrFE) samples.

The final chapter summarizes the main findings and discussions of this thesis and presents a perspective for future work based on nano-imprinted arrays of ferroelectric crystals and the nanoimprinting lithography technology.

Chapter 1

Bibliography

1. Pinnow, C.-U. and T. Mikolajick, *Material Aspects in Emerging Nonvolatile Memories.* Journal of the Electrochemical Society, **2004**. 151, K13-K19.

2. Ling, Q.-D., D.-J. Liaw, C. Zhu, D.S.-H. Chan, E.-T. Kang, and K.-G. Neoh, *Polymer electronic memories: Materials, devices and mechanisms.* Progress in Polymer Science, **2008**. 33, 917-978.

3. Ling, Q.-D., D.-J. Liaw, E.Y.-H. Teo, C. Zhu, D.S.-H. Chan, E.-T. Kang, and K.-G. Neoh, *Polymer memories: Bistable electrical switching and device performance.* Polymer, **2007**. 48, 5182-5201.

4. Reed, M.A., C. Zhou, C.J. Muller, T.P. Burgin, and J.M. Tour, *Conductance of a Molecular Junction.* Science, **1997**. 278, 252-254.

5. Service, R.F., *Organic Device Bids to Make Memory Cheaper.* Science, **2001**. 293, 1746.

6. Yang, Y., J. Ouyang, L. Ma, R.J.H. Tseng, and C.W. Chu, *Electrical Switching and Bistability in Organic/Polymeric Thin Films and Memory Devices.* Advanced Functional Materials, **2006**. 16, 1001-1014.

7. Brondijk, J.J., K. Asadi, P.W.M. Blom, and D.M. de Leeuw, *Physics of organic ferroelectric field-effect transistors.* Journal of Polymer Science Part B: Polymer Physics, **2012**. 50, 47-54.

8. Heremans, P., G.H. Gelinck, R. Müller, K.-J. Baeg, D.-Y. Kim, and Y.-Y. Noh, *Polymer and Organic Nonvolatile Memory Devices.* Chemistry of Materials, **2010**. 23, 341-358.

9. Naber, R.C.G., K. Asadi, P.W.M. Blom, D.M. de Leeuw, and B. de Boer, *Organic Nonvolatile Memory Devices Based on Ferroelectricity.* Advanced Materials, **2010**. 22, 933-945.

10. Youn Jung, P., B. In-sung, K. Seok Ju, C. Jiyoun, and P. Cheolmin, *Control of thin ferroelectric polymer films for non-volatile memory applications.* Dielectrics and Electrical Insulation, IEEE Transactions on, **2010**. 17, 1135-1163.

11. Sheikholeslami, A. and P.G. Gulak, *A survey of circuit innovations in ferroelectric random-access memories.* Proceedings of the IEEE, **2000**. 88, 667-689.

12. Scott, J.F., *Applications of modern ferroelectrics.* Science, **2007**. 315, 954-959.

13. Setter, N., D. Damjanovic, L. Eng, G. Fox, S. Gevorgian, S. Hong, A. Kingon, H. Kohlstedt, N.Y. Park, G.B. Stephenson, I. Stolitchnov, A.K. Taganstev, D.V. Taylor, T. Yamada, and S. Streiffer, *Ferroelectric thin films: Review of materials, properties, and applications.* Journal of Applied Physics, **2006**. 100, 051606-051606.

14. Weiss, R., *Flash memory takes over.* Electron Des, **2001**. 49, 56-64.

15. Naber, R.C.G., C. Tanase, P.W.M. Blom, G.H. Gelinck, A.W. Marsman, F.J. Touwslager, S. Setayesh, and D.M. de Leeuw, *High-performance*

solution-processed polymer ferroelectric field-effect transistors. Nature Materials **2005**. 4, 243-248.

16. Hu, Z., M. Tian, B. Nysten, and A.M. Jonas, *Regular arrays of highly ordered ferroelectric polymer nanostructures for non-volatile low-voltage memories.* Nature Materials **2009**. 8, 62-67.

17. Chou, S.Y., P.R. Krauss, and P.J. Renstrom, *25-nanometer resolution.* Science272, **1996**, 85-87.

18. Chou, S.Y., P.R. Krauss, W. Zhang, L. Guo, and L. Zhuang, *Sub-10 nm imprint lithography and applications.* Journal of Vacuum Science & Technology B: Microelectronics and Nanometer Structures, **1997**. 15, 2897-2904.

19. Furukawa, T., *Ferroelectric properties of vinylidene fluoride copolymers.* Phase Transitions, **1989**. 18, 143-211.

20. Matsushige, K., S. Imada, and T. Takemura, *Temperature Effect on Ferroelectric Polarization Switching in Poly(vinylidene fluoride).* Polymer Journal, **1981**. 13, 493-499.

21. Sawyer, C.B. and C.H. Tower, *Rochelle Salt as a Dielectric.* Physical Review, **1930**. 35, 269-273.

22. Jesse, S., A.P. Baddorf, and S.V. Kalinin, *Switching spectroscopy piezoresponse force microscopy of ferroelectric materials.* Applied Physics Letters, **2006**. 88, 062908-062908.

23. Hu, Z., G. Baralia, V. Bayot, J.-F. Gohy, and A.M. Jonas, *Nanoscale Control of Polymer Crystallization by Nanoimprint Lithography*. Nano Letters, **2005**. 5, 1738-1743.

24. Sergei, V.K., N.M. Anna, C. Long Qing, and J.R. Brian, *Local polarization dynamics in ferroelectric materials.* Reports on Progress in Physics, **2010**. 73, 056502.

25. Elisabeth, S., *Piezoresponse force microscopy (PFM).* Journal of Physics D: Applied Physics, **2011**. 44, 464003.

Chapter 2

Ferroelectric Polymers for Memory Applications

The current renewed interest in ferroelectric polymers essentially stems from the development of organic electronics and the need to develop cheap non-volatile memories. Therefore, in this chapter, we first introduce the main types of memories and the interest of ferroelectric materials in this context. We then turn to organic ferroelectric materials with particular attention on poly(vinylidene fluoride) and its copolymers with trifluoroethylene, P(VDF-TrFE), which is the material of this thesis. Finally, three typical ferroelectric polymer based non-volatile memory architectures are summarized, to give to the reader a better view of how ferroelectric polymers can be used practically.

Chapter 2

2.1 Electronic Memories

During the last decades, rapid progress has been made in the introduction and use of information technology and portable computing devices that have transformed daily life. These technological advancements have been supported by the emergence of new materials and the ability to fabricate ultra-small transistors and integrated electronic circuitry. A key element of these progresses includes the development of high performance electronic data storage devices. Electronic memories are devices or recording medium that can retain retrievable digital data over a given time interval. Understandably, to satisfy the unprecedented demand of portable computing and sophisticated microelectronic devices, major advances in the field of electronic memories needs to be achieved, since they are one of the fundamental components of all modern computers and electronic systems. These kinds of applications necessitate the use of electronic memories that are fast in response and compact in size, and that can read and write when connected to a central processing unit [1].

Information in the majority of electronic devices is stored in the form of binary logic (bit) where digital data are represented as either “0” or “1” values [2]. This is an easy and robust way to store data and make it understandable by digital integrated circuits (ICs). In fact, the notion of binary data storage dates back a couple of centuries. As an example, book music (programmed musical instruments) was used to make pianos and organs play automatically since the 18^{th} century. These mechanical storage media were made of folded books consisting of holes: notes were played when there was a hole (“1”) or not (“0”). Furthermore, the evolution of storage medium passed different stages including the bulky and expensive magnetic core memory (ferromagnetic memory), which

comprises of a regular array of tiny magnetic cores that can be magnetized in one of two opposite directions, therefore, storing binary data in the form of a magnetic field (Figure 2.1) [3]. Nevertheless, technologies like ferromagnetic memories were the cradle for the innovation of modern electronic memories that are in every electronics media nowadays [4]. To visualize how far the electronic memory technology has come through, and to compare them with the recent memory technologies that are presented in the following sections, a typical ferromagnetic core memory is shown in Figure 2.1.

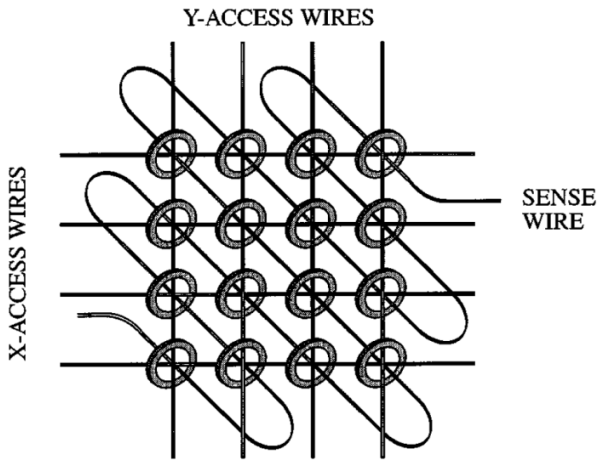

Figure 2.1: Schematic circuit design of the early two-dimensional magnetic core memory [3].

It should however be mentioned here that there are also other forms of data storage, which are often referred as mechanical storage devices, because unlike the electronic memories they require mechanical equipment (drivers) to convert optical, magnetic or other signals to electrical signals for the central processing system to recognize them [5]. Some examples of mechanical storage devices include CD, DVD, floppy disk, hard disk, and video/audio tapes.

Chapter 2

Volatile and Non-volatile Electronic Memories

On the basis of data volatility, electronic memories can be divided into two categories: volatile and non-volatile memories [6]. Volatile electronic memories that are often found in computers need a constant power supply to retain the stored information, and the stored data will be lost as soon as the system is turned off. On the other hand, the non-volatile memories can retrieve the stored information even when the electrical power supply is turned off, making them compulsory in applications that cannot perform constant memory refresh operations to prevent loss of data [1, 5, 7, 8]. Most storage devices, whether volatile or not, are based on random-access memories (RAMs). In the case of RAMs any piece of data can be written to or read in any order, independent of its physical location and whether or not it is related to the previous piece of data [2, 3]. In the subsequent paragraphs the advantages and limitations of some typical examples of volatile and nonvolatile memories are discussed briefly.

One typical electronic device that can be classified as volatile is dynamic random access-memories (DRAM), which is often used to store temporary data and programs for processing in computers [2]. In DRAM each bit of data is stored in a simple and separate capacitor connected to transistors, accounting for some of their main advantages, which are structural simplicity, high density and fast operation, and thus ultimately making them one of the most often produced integrated Circuits (IC) [6]. Nevertheless, because the capacitors leak charge, the stored data eventually fades, necessitating a periodic refreshing of the capacitor charge.

One example of nonvolatile memory is flash memory, which consists of cells that are a kind of transistor switched by a process of quantum tunneling of

electrons through a very thin dielectric layer [8]. However, unlike DRAMs that can undergo many trillions of write and read operations, flash memory technologies are limited by the leaky tunneling barriers as a result of the multiple switching events. In addition, flash memories on flexible plastic substrates using organic transistors with a floating gate embedded in hybrid dielectrics has been reported in 2009 [9]. However, the data retention is far less than the silicon based flash memories due to a lack of properly insulating organic materials. Flash memories are widely used in portable electronic systems, such as mobile PCs and memory cards [6]. One other class of nonvolatile memory is known as magnetoresistive random access-memory (MRAM), thanks to the recent developments in the physics of spin electronics (spintronics) [10]. As the name itself suggests, in MRAM, data is no longer stored by electrical charges, as in the case of semiconductor memories, but by two opposite directions of the magnetization vector in a small magnetic nanostructure [11]. The main potential of using magnetic states for data storage is that the magnetic polarization does not leak away with time like charge does, so the information is stored even when the power is turned off, which in effect make them classed as the nonvolatile memories [12].

In today's technology there is no single memory technology that can satisfy all requirements of low cost, high density, low energy, and high endurance. For this reason, there is always a need to explore a new memory technology. One typical electronic memory that can be considered as an emerging class of nonvolatile memory is ferroelectric random-access memory (FeRAM), which has the potential to supplement the already existing electronic memories [13-15]. Since the aim of this thesis is also studying one of the promising candidates that can be used in the fabrication of ferroelectric nonvolatile memories, a bit of detail is

presented in the next section focusing on the basic operation and developments in FeRAMs.

2.2 Ferroelectric Random-access Memories (FeRAM)

In some respect ferroelectric memories share with dynamic random-access memories architectural features such as being in the form of a capacitor, however, the dielectric medium in between the electrodes is a ferroelectric material rather than an insulator which is the case of DRAMs [3]. The working principle of nonvolatile ferroelectric random-access memory (FeRAMs) is based on the electrical polarization of a ferroelectric material that can be repeatedly switched between two stable states by an external electric field [15, 16]. The binary information digits “0” and “1” are then associated with the two states of polarization that are equally stable. Moreover, because no applied voltage is required to sustain these states, a memory device based on ferroelectric materials is classified as nonvolatile [17]. Some promising features of FeRAMs compared with other classes of nonvolatile memories include superior write-access time, smaller power consumption, and easier embedding in integrated circuits [3, 16].

Some ferroelectric memory devices are constructed by ferroelectric capacitors which operate in destructive mode because the information must be rewritten after every read operation. On the other hand, there are also ferroelectric memories where the information can be read over and over again until the next write operation; these are classified as non-destructive devices and are in the form of field-effect transistors where the gate dielectric consists of a ferroelectric material [18]. Here, we will briefly present the basic working

principle of the first category of ferroelectric memories just for the sake of simplicity.

The first ferroelectric memory test chip integrated with silicon CMOS (complementary metal-oxide-semiconductor) technology was reported in 1988, and has demonstrated the potential to be a practical memory [19]. This 256 bits initial memory was made up of two PZT (Lead Zirconate Titanate) ferroelectric capacitors and six-transistors as a typical static random-access memory cell. A typical 1T-1C (one transistor, one capacitor) ferroelectric memory cell is shown in Figure 2.2.

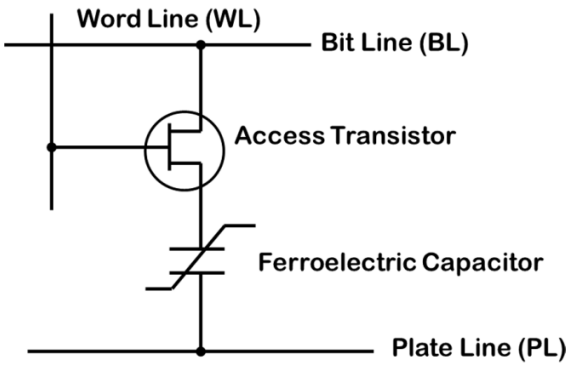

Figure 2.2: Schematic representation of a 1T1C ferroelectric memory cell structure, consisting of a single ferroelectric capacitor that is connected to a plate line (PL) at one end, via an access transistor, and to a bit line (BL) at the other end. In this kind of architecture, the memory cell is accessed by applying voltage on the word line (WL) and hence turning ON the access transistor.

The amount of charge accumulated on the capacitor plates depends on the direction of the applied voltage with respect to the initial direction of polarization in the ferroelectric capacitor, since polarization switching is normally accompanied by (compensating) charge flow (or not) onto a reference capacitor [3]. Writing "0" or "1" into the memory cell is then dependent on whether compensating charge flows or not to the capacitor. On the other hand, sensing (determining) the current transient when an external voltage is applied will enable us to read the stored information [16, 17, 19].

The conventional materials used in FeRAMs have often been inorganic ferroelectric crystals. However, recently, organic ferroelectric materials are getting a significant attention because they are promising candidates for the future not only for their attractive features of low-cost, easy processibility, and simplicity in device structures, but also for their potential in the realization of molecular and organic memories [6, 13, 14, 18, 20-24]. The different designs and progress made in the field of organic based ferroelectric memories is presented at the end of this chapter. In the next section; however, an introduction about ferroelectricity followed by the different types of ferroelectric materials, with a particular emphasis on ferroelectric polymers, is presented.

2.2 Ferroelectric Polymers

2.2.1 Introduction

Ferroelectric materials can be broadly defined as a special class of dielectrics with two or more stable states of different nonzero polarization that are permanent, meaning thermodynamically stable [3, 15, 17]. In addition, the

spontaneous electric polarization must be switchable, repeatedly, between the two states by the application of an external electric field [18]. The first ferroelectric material reported was Rochelle salt ($NaKC_4H_4O_6.6H_2O$) which was discovered in 1921 by Valasek [25]. Since then, a lot of new ferroelectric materials, both inorganic ones like barium titanate ($BaTiO_3$), and those somewhat different from the traditional ones, namely ferroelectric organic materials like polyvinylidene fluoride (PVDF) and its copolymers, were discovered [17, 26]. Ferroelectricity, that can persists up to 127^{o}C, has also been reported recently in organic molecules of crystalline croconic acid, $H_2C_5O_5$ [27], and in chemically stable biological systems such as benzimidazoles [28].

Because of the switchability of the spontaneous polarization, the plot of the electric displacement versus the electric field of those ferroelectric materials exhibits a significant hysteresis loop (Figure 2.3(b)) contrarily to most dielectric materials for which the polarization varies linearly with an increase of electric field (Figure 2.3(a)). However, it should be noted here that all hysteresis loops do not confirm the ferroelectricity of the material; for instance, a recent provocative paper of Scott [29] show that even a banana slice can exhibit some kind of hysteresis loop. However, the electric hysteresis loops of a real ferroelectric material should saturate at large electric field and the shape should be concave.

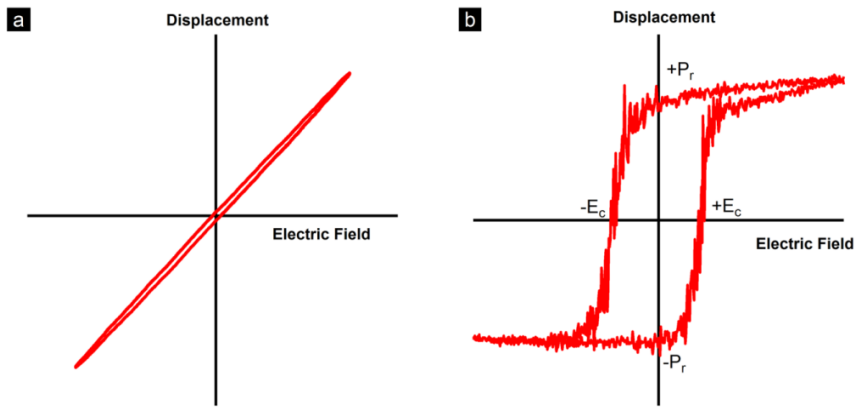

Figure 2.3: Displacement versus electric field of a normal dielectric (a), and (b) of a typical ferroelectric material.

From the intercept of a saturated electric hysteresis loop like the one shown in Figure 2.3(b) with the displacement (polarization) axis, the magnitude of the zero-field remanent polarization, P_r can be readily obtained. In fact, the presence of this remanent polarization is the physical basis for the application of ferroelectric materials in the fabrication of memory devices. In addition, the intercept of the hysteresis loop with the applied electric field axis is known as the coercive field, the minimum value of the electric field necessary to return the polarization to zero, E_c [18, 26]. In practice, larger voltages need to be applied to increase the switching rate.

Another important characteristics of most ferroelectric materials is that they show a phase transition at higher temperature. Above the transition temperature (called Curie temperature, T_c), the crystalline structure of ferroelectric materials changes into a less ordered or disordered non-ferroelectric one, termed as paraelectric phase. This phase transition is reversible when the temperature is

lowered through the Curie point, i.e., from the paraelectric to the ferroelectric state.

In the absence of electric field, the polarization of the material is homogeneous in ferroelectric domains of smaller sizes, separated by domain walls. Upon application of an electric field, nucleation and growth of domains of larger size and uniform polarization is observed, leading to macroscopic polarization of the material. Due to the significant energy resulting from the field created by this macroscopic polarization, the material depolarizes upon removal of the field, unless the polarization charges are screened by mobile charges such as found in metallic electrodes [30]. This is the case for the configuration of ferroelectric materials in a capacitor (Figure 2.4). Two stable polarization states can be defined for this configuration with the total electric field outside and inside the capacitor being null, except for stray, fringe fields. Switching between the two states results in a current that flows from one electrode to the other, which serves to detect the starting polarization states in capacitor memory devices [31].

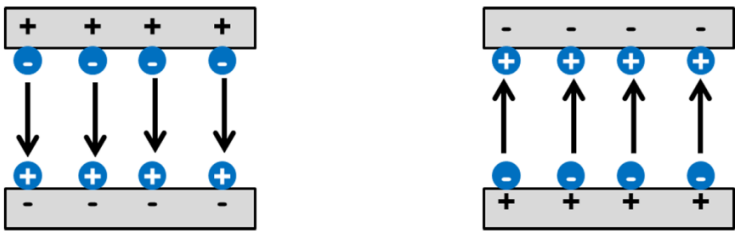

Figure 2.4: The two stable states of a polarized ferroelectric material in a capacitor, in the absence of external electric field.

It should be mentioned that all ferroelectric materials are piezoelectric, though the reverse is not true. Piezoelectrics belong to a class of materials where an applied force (mechanical stress) changes the polarization of the material and vice versa [32]. Piezoelectricity is found only in few materials and depends greatly on the molecular arrangement of the material, requiring its crystal structure not having a center of symmetry. In these kinds of crystals, the applied mechanical stress will modify the separation between the positive and negative charge sites in each elementary cell leading to a net polarization at the crystal surface, which is often referred to as the direct piezoelectric effect [33]. This effect is linear, i.e. the change in polarization ($\Delta \boldsymbol{P}_i$) varies directly with the applied stress σ_{jk}, and can be expressed mathematically as

$$\Delta \boldsymbol{P}_i = d_{ijk}\, \sigma_{jk} \quad \ldots\ldots\ldots\ldots\ldots\ldots\ldots (2.1)$$

where $\boldsymbol{P}_i$ is the polarization vector (i = 1, 2, 3), and d_{ijk} is a third-rank tensor and are the piezoelectric strain coefficients which make a third rank tensor. On the other hand, the converse piezoelectric effect expresses the linear relationship between the strain (ε_{jk}) and the applied electric field (E_i) as follows:

$$\varepsilon_{jk} = d^c{}_{ijk}\, \boldsymbol{E}_i \quad \ldots\ldots\ldots\ldots\ldots\ldots\ldots (2.2)$$

where $d^c{}_{ijk}$ are the converse piezoelectric coefficients. Usually a more simplified notion of the stress tensor is made from some assumptions and symmetry reasons. For example, in the particular case of polymers like PVDF, the major components of piezoelectric strain coefficients are d_{31}, d_{32}, and d_{33}, the first subscript defining the electric field direction and the second that of mechanical stress (in the usual convention for a stretched film sample, direction 1 is the stretching direction, 2 the transverse direction, and 3 is perpendicular to

the film surface) [34]. Typically for the β-phase of PVDF d_{33} is *ca*. -30 pC/N. The negative value means that a stress applied normal to the film increases its thickness, thus decreasing the polarization.

2.2.2 Inorganic Ferroelectrics

The origin of spontaneous polarization in these materials is due to the atomic arrangement of ions in crystals with a polar space group. Nevertheless, because the two stable polarization states should be switchable for the material to be considered as ferroelectric, all polar crystals are not ferroelectric [15]. Specifically for inorganic ferroelectric materials, the presence of displaced polar atoms creates a noncentrosymmetric arrangement of ions in its unit cell, producing an electric dipole moment that can be switched between two stable positions [3]. One typical example for these classes of ferroelectrics is the perovskite structure, having a formula of ABO_3 shown in Figure 2.5.

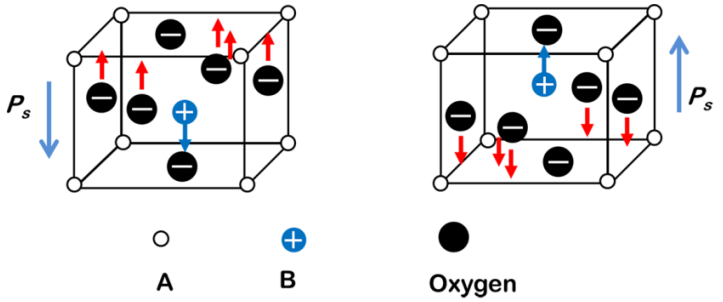

Figure 2.5: The crystal structure of a typical inorganic ferroelectric material showing the unit cell of an ABO_3 perovskite structure. The central blue-filled circles are typically cations (like titanium, Ti^{4+} or zirconium Zi^{4+}). The displacement of the central atom either "up" (right) or "down" (left) is the reason for the presence of spontaneous polarization (P_s). These polarization states can be reversed by the application of an electric field in the opposite direction.

Creating high density arrays of ferroelectric memories that work at low voltage necessitates the use of extremely thin films of ferroelectric materials [17, 35]. There are already inorganic-based high density nonvolatile ferroelectric memories on the market; however, due to the desire for an even denser, more flexible, cheaper, and low voltage memories, ferroelectric polymers are gaining a lot of attention as an alternative, and are the topic of the next section [14, 36-39].

2.2.3 Organic Ferroelectrics

Another class of ferroelectric materials is made of those that are commonly known as ferroelectric polymers. Unlike inorganic ferroelectric materials where atoms constitute ordered crystal lattices, organic ferroelectric materials have a strikingly different and complex structure [34, 40]. Typically ferroelectric polymers are macromolecules, comprising of crystalline and amorphous regions with lower degree of symmetry. The first found organic polymer having ferroelectric property was polyvinylidene fluoride (PVDF), which was earlier known for its piezoelectricity only [41]. In this case, the polarization originates from the strong dipole moment of the $-(CH_2-CF_2)-$ repeating unit, resulting from the electronegativity of the F atoms. Thereafter, a number of other organic ferroelectric materials were discovered, such as odd nylons [42]. Nylon is a name given to polymers containing a planar $-CH_2-$ backbone with polar amide (CO)−(NH) dipoles connecting them as a repeating unit [40]. Nylons are often named after the number of carbon atoms in the repeating unit of the polymer backbone. Thus, odd nylons mean that the corresponding chemical structure contains odd numbers of carbon atoms in the repeating unit. The reason that only odd nylons are referred to as ferroelectric polymers is because the dipoles (carbonyl groups) in odd nylons are aligned in the same direction (where all chains are in all-trans conformation), resulting in a large spontaneous polarization in the unit cell of the crystalline phase [42]. However, due to the hydrogen bonding between the =O and −NH− on neighboring chains, polarization or switching is difficult in odd nylon systems [43].

Other ferroelectric materials are liquid crystalline polymers, consisting of rodlike or disklike molecules [44]. As their name implies, the state of matter of liquid crystals is in-between those of liquids and crystals, exhibiting a fourth

state of matter. Among others, the ordering of crystals can be in *smectic phases* (layered structures) or *nematic* phases (parallel orientation) [42]. The origin of and the requirement for the presence of spontaneous polarization in liquid crystals is associated with the presence of tilted molecules relative to the normal to the plane of the layers, and the details can be found in the literature [40, 42, 44].

Table 1: Properties of typical ferroelectric polymers compared with those of inorganic compounds [45].

Materials	**Curie transition temperature (ºC)**	**Dielectric constant**	**Spontaneous polarization, P_s (μC cm^{-2})**	**Coercive field, E_c (kV cm^{-1})**
Organic molecules				
$VDF_{0.65}$–$TrFE_{0.35}$	90	20	8	500
Nylon-11	-	-	5	600
Inorganic compounds				
$BaTiO_3$	108	$5x10^3$	26	10
$PbTiO_3$	490	210	75	7

To give some perspective on organic ferroelectrics, some of their typical properties are listed in Table 1 and compared with two selected ferroelectric compounds.

To date, polymers made of vinylidene fluoride (VDF) copolymerized with trifluoroethylene (TrFE) are the most studied ferroelectric polymers thanks to their large dipole moment and excellent polarization stability, and are used successfully in wide range of applications, making them also the logical choice

here to be used in this thesis [43]. In the next section, the discussion is focused on P(VDF-TrFE) including their structural and electrical properties, and recent advances made to improve their ferroelectric properties.

2.3 P(VDF-TrFE)

Polyvinylidene fluoride (PVDF) is a semicrystalline polymer which has a monomer unit of $–CH_2–CF_2–$, with good flexibility and chemical stability [34, 40-43]. The way the monomers are linked together during the preparation (polymerization) of PVDF directly influences the chain configuration. Usually the monomeric unit $–CH_2$ denoted as the "head" is linked with the $–CF_2$ (tail) in regular head-to-tail sequences. However a reversed monomer addition can also occur and results in head-to head or tail-to-tail configurations, leading to the creation of configurational defects. As it has been said before, the origin of ferroelectricity in PVDF is due to the presence of electric dipoles as a result of large difference in electronegativity between fluorine (4.0), carbon (2.5), and hydrogen (2.1) [32, 33, 46]. Contrarily to most polymers that have one regular conformation of lowest potential, PVDF can adopt different regular conformations. This is because the PVDF monomer unit ($–CH_2–CF_2–$) is intermediate between polyethylene (PE) $–(CH_2–CH_2)–$, which has low (easy) rotational barriers separating its possible conformations, and as a result reaching the all-*trans* as the lowest-energy conformation, and those of polytetrafluoroethylene (PTFE) $–(CF_2–CF_2)–$, where the rotation is hindered due to the presence of the bulkier fluorine atom, often leading to helical or quasi-helical conformations [34]. For this reason PVDF has multiple conformations. Typically, on the basis of conformation and packing of molecules, PVDF can have four different types of polymorphs, denoted as phase I (β), phase II (α),

phase III (γ), and phase IV (δ) [40, 42]. For example, melt-crystallization of PVDF produces a conformation TGTG' consisting of alternating *trans* (T) and *gauche* (G) C−C bonds packed in an antiparallel fashion (Figure 2.6, left), which is referred to as the α phase. This phase is not ferroelectric since the dipole moments of each chain cancel each other out. Among the aforementioned four polymorphs, the β phase has polymer chains in all-*trans* conformation (parallel) (Figure 2.6, right), and thus it is ferroelectric with a large spontaneous polarization [26, 47]. To make it more clear, for the all-*trans* conformations the substituents are 180° from each other and ± 60° for the *gauche* ($^{\pm}$) arrangement, though the actual torsional angles often deviate from these values [34].

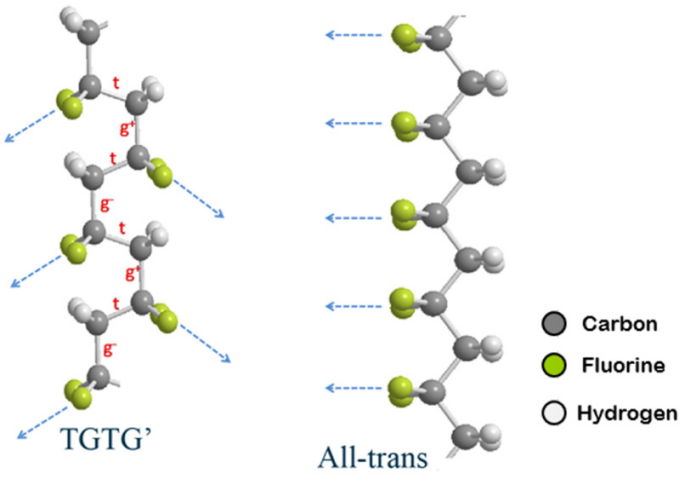

Figure 2.6: Schematic depiction of the two most common chain conformations in crystalline PVDF: TGTG' (left) and all-trans (right); the arrows indicate the $-CF_2$ dipole directions projected on planes defined by the carbon backbone [48].

The other polymorph of PVDF, which is intermediate between the α and β-phases, is the γ phase [49]. Chains in γ (TTTGTTTG') are packed in a polar fashion, and thus the material is ferroelectric [34]. The fourth polymorph of PVDF is the δ-phase, which is actually a polar version of the α-phase, and can be obtained by application of a high electric field to the α-phase. Recently, Li et al. have confirmed experimentally the existence of δ-phase by measuring the typical ferroelectricity characteristics such as the coercive field and the remanent polarization from hysteresis loops [49]. Interestingly, it is possible to transform one polymorph of PVDF into another one through rotation, of chain segments, using methodologies like heating, stretching, or by external electric fields [50-52]. Figure 2.7 illustrates some typical interrelations between the four polymorphs of PVDF.

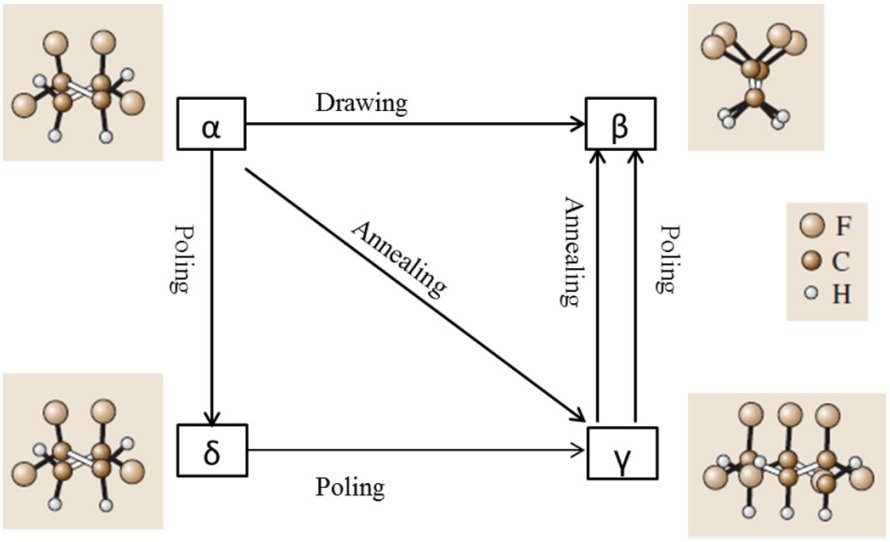

Figure 2.7: Transformation between the four well established polymorphs of PVDF [26].

Because the β phase is not thermodynamically the most stable one, it cannot be achieved by a direct deposition of thin films of PVDF on substrates, making this polymer difficult to use for some applications. To overcome this limitation, compositional modification of PVDF through copolymerization with trifluoroethylene (TrFE) was found to favor the all-trans (polar) phase directly from the melt or solution [40, 42, 43]. Figure 2.8 shows the chemical structure of P(VDF-TrFE) copolymer.

By adding TrFE in the PVDF, some smaller hydrogen atoms are randomly replaced by bigger fluorine atoms, inducing severe instability in the TGTG' conformation because of the close proximity of the fluorine atoms in a *gauche* arrangement [33]. To avoid this created instability, the P(VDF-TrFE) copolymer

takes all-*trans* conformation packing in a phase similar to the (polar) *β* phase of PVDF, in a certain range of composition [26]. More interestingly, in so doing the crystallinity of PVDF (50 %) can be enhanced up to 90 % in the copolymer [40]. Thus, the ferroelectric β phase with higher crystallinity can be achieved directly from the P(VDF-TrFE) solution or the melt, which is indeed crucial for some applications like organic electronic devices. In this thesis, all the discussions are then focused only on the polar β phase of P(VDF-TrFE) copolymers.

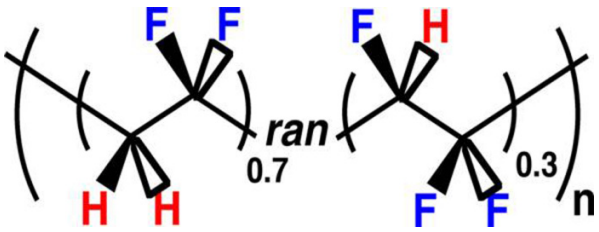

Figure 2.8: A typical chemical formula of P(VDF-TrFE) copolymer with 30 % molar TrFE content.

In addition, as a result of TrFE introduction, the Curie transition temperature is lower than the pure PVDF because the interactions between each unit cell and dipole-to-dipole are reduced [46, 53]. Of note, the Curie transition temperature of PVDF is above the melting temperature. However, for a typical P(VDF-TrFE) copolymer with 30 % TrFE content, the Curie temperature (T_{cur}) is around 117°C, whereas the melting temperature (T_m) is around 145°C (Figure 2.9). Upon heating the P(VDF-TrFE) above the Curie transition, the ordered all-*trans* conformation changes into a more random paraelectric phase. This phenomenon is reversible, i.e., the ferroelectric phase can be recovered upon cooling below

the Curie transition [54, 55]. In fact, this conformational change can be used to increase the crystallinity of the semicrystalline P(VDF-TrFE) copolymer with an annealing process at a temperature between the Curie and melting point; thereby the ferroelectric performance is enhanced [56]. The composition of TrFE content in the P(VDF-TrFE) copolymer is equally critical in determining the Curie temperature, and thus the ferroelectric properties. Figure 2.9 illustrates that when the composition of TrFE is increased from 30 to 44 molar %, T_{cur} decreases from 117 to 60°C. Furthermore, when the molar composition of the TrFE is larger than 56 %, T_{cur} vanishes, indicating a loss of ferroelectricity (Figure 2.9, red trace). This clearly demonstrates that copolymers of special interest are only those with a molar content in VDF about 70 % as evidenced from their clear Curie point, which is normally absent in pure PVDF.

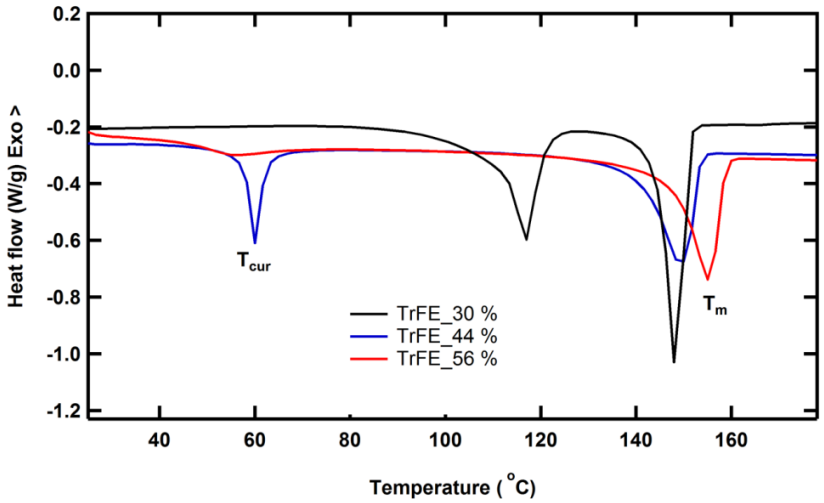

Figure 2.9: Differential scanning calorimetry (DSC) heating traces for P(VDF-TrFE) copolymers whose TrFE molar compositions are given in the figure.

The molecular and structural changes occuring at the ferroelectric/paraleectric phase transition of P(VDF-TrFE) copolymers upon heating and cooling have been studied by Lovinger et al. [53, 57] and Tashiro et al. [58] using X-ray diffraction and infrared spectroscopy. X-ray results showed that in the ferroelectric phase the P(VDF-TrFE) molecules are arranged in a compact hexagonal lattice [53]. However when the specimen is heated at a temperature above the Curie point, they rearrange to a much larger paraelectric lattice [59]. The observed changes in lattice spacing during the ferroelectric to paraelectric transition are shown to be correlated with conformational changes through the introduction of g^- and g^+ bonds resulting to a random sequence of tg^+ and tg^- groups in the paraelectric phase [60]. Lovinger et al. have shown that the transition from a conformation analogous to that of the β-PVDF phase (ferroelectric) to that of a more disordered one, which is similar to the helical conformation of PF_3E, is primarily a result of intramolecular conformational changes; these changes require further intermolecular lattice expansion to PF_3E-like spacings [53, 57]. However it should be mentioned that even though the chains of the paraelectric phase assume disordered conformations, they are still packed on a pseudo-hexagonal lattice [60]. Information about the microstructural changes and phase transformations of P(VDF-TrFE) were also obtained from the variation of mechanical strength (tensile modulus) as a function of increasing temperature [59, 60]. These studies show that upon heating the mechanical strength of P(VDF-TrFE) materials exhibit different values (slopes) corresponding to the various transition temperatures. Specifically, Murata et al. have shown that the tensile modulus of P(VDF-TrFE), with 30 mol% TrFE, decreases significantly from around 2 GPa in its ferroelectric phase to around 100 MPa in its paraelectric phase [59]. For comparison, the tensile modulus of a typical rubber is ~1-5 MPa. Overall, it can

be generalized that the fast decrease of tensile modulus with increasing temperature, above T_{cur}, is similar to that obtained for glassy polymers just above their glass transition temperature (T_g), well below the rubbery plateau [60]. This suggests that the high temperature paraelectric phase of P(VDF-TrFE) copolymer is definitely not a polymeric liquid, but rather a liquid-crystalline material with partial ordering and a reduced mechanical strength. Due to this lower strength, when the copolymer is pressed in its paraelectric phase at some pressure, like in the case of nano-embossing, the polymers chains can be pushed into the cavities of the embossing molds.

In the β phase, the polymer chains in all-*trans* conformation are normally packed in a quasi-hexagonal polar structure, generating a large spontaneous polarization [26, 43]. Figure 2.10 shows a typical 3D scheme for the packing of the chains in all-*trans* conformation, with the three lattice constants.

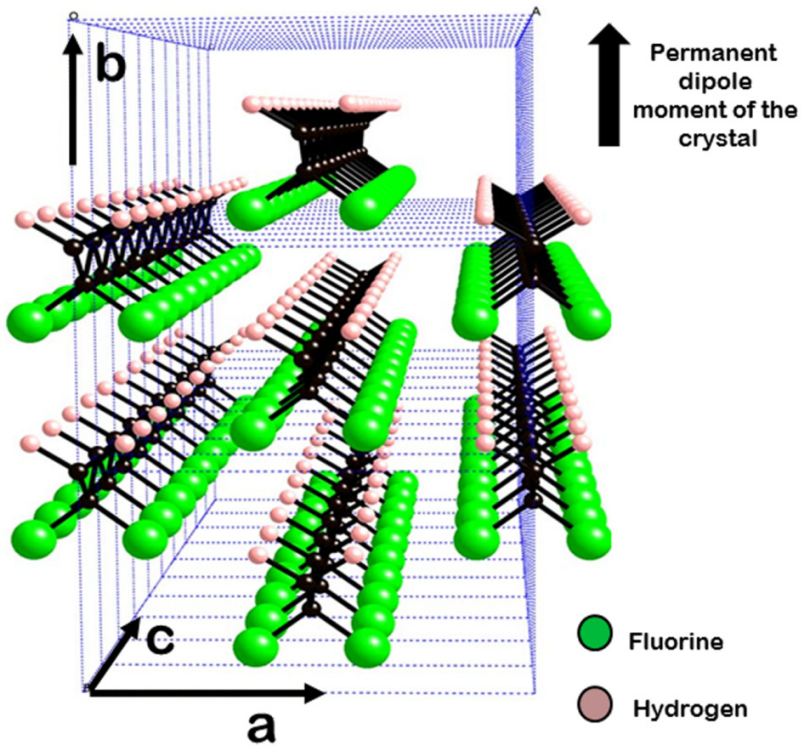

Figure 2.10: 3D-crystal structure of the polar β-phase of PVDF

When P(VDF-TrFE) copolymers crystallize, the polymer molecules are folded many times to form crystalline lamellae, and the lamellae in turn arrange in spherulites [40]. In spherulites, the lamellae are locally stacked, separated by amorphous regions consisting of tight and loose chain folds, tie molecules, or dangling chain ends as shown in Figure 2.11. It is worth to note that the polymer molecules are oriented perpendicular to the surface of the lamellae. The spontaneous polarization in P(VDF-TrFE) is along the *b* axis which is parallel to the C-F dipole moment, and perpendicular to the *c* axis (chain direction) as illustrated in Figure 2.10 [61]. The orientation of the crystallographic axes with

respect to the surface (substrate) is very important for some applications. Because dipole moment switching by applied electric field needs to be achieved for memory application, optimal coupling (along the same direction) between the polarization vector and the field is necessary.

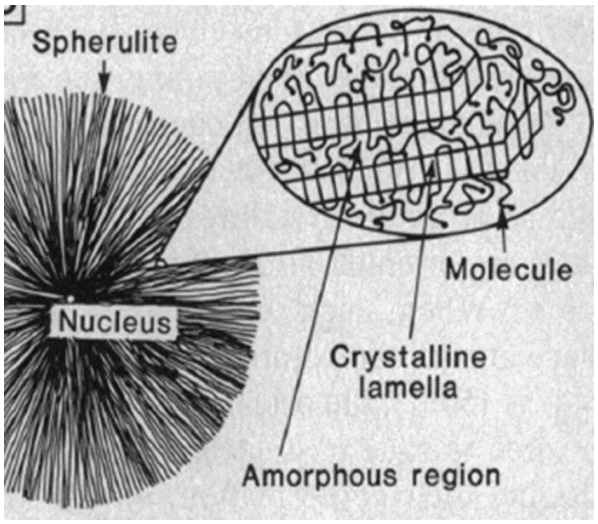

Figure 2.11: Schematic representation of the structure of polymer spherulites [34].

The orientation of the crystallographic axes of a particular P(VDF-TrFE) sample can be obtained from infrared (IR) spectroscopic investigations thanks to a change in the transition dipole moment of molecules with the electric field component of an incident infrared radiation. Since this knowledge of infrared active modes of P(VDF-TrFE) is very important to complement the subsequent chapters, a complete mode assignment for the ferroelectric phase of the P(VDF-TrFE) copolymer, based on theoretical and experimental work for the β-PVDF crystals, is given in Table 2 (from ref. [62]).

Table 2: Observed and calculated infrared active modes for PVDF and P(VDF-TrFE) polymers in the crystallographic β phase [62].

Observed PVDF (cm^{-1})	Observed Copolymer (cm^{-1})	Calculated Freq. (cm^{-1})	Attribution	Symmetry
3014	3012	3029	ν_a (CH_2)	B_2
2977	2977	2980	ν_s (CH_2)	A_1
	1453	(1456)	[δ (CH_2) in TG^+TG^- defect]	—
1430	1428	1423	δ (CH_2)	A_1
1400	1402	1396	ω (CH_2)	B_1
	1345	1334	[ν_s (CC) in TG^+TG^- segment]	—
1273	1291	1286	ν_s (CC)	A_1
1180		1182	ν_a (CF_2)	B_2
1071		1065	ν_a (CC)	B_1
983		Inactive	t (CH_2)	A_2
880	886	879	r (CF_2)or ν_s (CF_2)	B_2 or A_1
840	851	825	ν_s (CF_2)or r (CF_2)	A_1 or B_2
	780	(784)	[ν_s (CF_2) in TG^+TG^- defect]	—
	616	(621)	[ω (CF_2) in TG^+TG^- defect]	—
	571	—	(defect)	—
511	506	508	δ (CF_2)	A_1
477	472	470	ω (CF_2)	B_1
440	440	443	r (CF_2)	B_2
	413	(423)	[r (CF_2) in TG^+TG^- defect]	—
372	372	—	Head-to-head defect	—
350	350	Inactive	t (CF_2)	A_2
262	—	Inactive	t (CF_2)	A_2

The symbols ν_a and ν_s represent, respectively, antisymmetric and symmetric stretching modes. The other vibration modes mentioned in the table are: δ, bending; r, rocking, ω, wagging, and t, twisting. The calculated values into parentheses correspond to predicted modes in the TG^+TG^- conformation, which are indeed observed in α-PVDF.

Moreover, the orientation of molecules or lamellar crystals in the P(VDF-TrFE) ultrathin films can be affected by spatial confinement (thickness) and annealing conditions [63, 64]. For example, Wu et al. have recently shown that for ultrathin films (~ 40 nm) annealed in the paraelectric phase, the lamellar crystals tend to grow faster along the crystallographic *a* axis with an edge-on orientation, and the *c* axis in the plane of the substrate [65]. On the other hand, these authors [65] and others [66] have reported that recrystallizing P(VDF-TrFE) ultrathin films from the melt resulted in flat-on orientation (crystallographic *c* axis normal to the substrate). Furthermore, continuous thin films annealed in the paraelectric phase but with higher nominal thickness (~150 nm) have shown a more random orientation of crystals in the film [65]. These findings underline that the orientation of the crystal unit cell for thin films of P(VDF-TrFE) can be controlled by processes such as thermal treatment and film thickness.

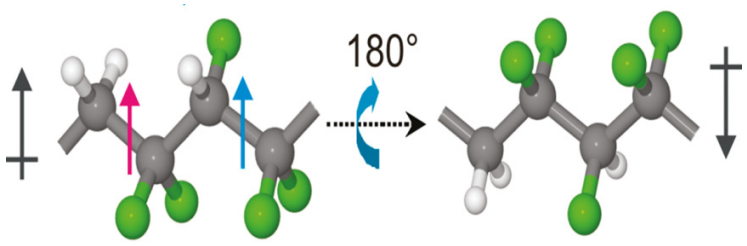

Figure 2.12: Ferroelectric switching mechanism in a single P(VDF-TrFE) chain (top), showing a 180° rotation of the polymer chain around its axis upon the application of a sufficiently large external electric field [23].

The other characteristic feature of ferroelectric P(VDF-TrFE) copolymers that needs special mention is their polarization reversal (Figure 2.12). Unlike the crystal inorganic ferroelectric materials, here the polarization switching

mechanism is not straight-forward, since it is governed by a rotation of the molecular chain in polycrystalline films [26]. As a result, there are a couple of models proposed to explain the polarization dipole reversal mechanism in ferroelectric polymers [40, 42, 46]. For example, Sharma et al. have shown that local polarization reversal proceeds through the formation of strongly irregular domains, which is attributed to the high degree of nonuniformity in the local switching potential due to the presence of defects in conformation and molecular packing [67]. Specifically for P(VDF-TrFE), the polarization switching has been described by an initial reversal of $CH_2{-}CF_2$ and $CHF{-}CF_2$ dipoles about the C−C molecular chain (Figure 2.12), followed by the expansion of rotated chains in the $a - b$ plane of the crystalline lamella, and finally throughout the film [26, 67]. In general, polarization reversal and switching time are controlled by two mechanisms, initial uniform reversal polarization nucleation (domain nucleation), followed by unrestricted expansion and domain wall motion throughout the sample, which is typically described by the classical Kolmogorov-Avrami-Ishibashi (KAI) model [46]. The switching time for each of the specific processes are different, since they have a different dependence on the electric field (E) [34, 42].

The switching time (τ_s) of a ferroelectric material has an exponential relationship with *E* and is expressed as

$$\tau_s = \tau_0 e^{(E_o/E)} \quad \text{..... (2.3)}$$

where E_o is the activation field, and τ_o is the switching time at infinite field *E*. Furukawa et al. have shown that for VDF(65)/TrFE(35) a linear relationship exists between log τ_s and 1/*E*, confirming the exponential law between τ_s and 1/*E* [26]. In addition, by extrapolating to an infinite field (1/E → 0) these

authors have reported a switching time (τ_0) of 10 nm. However, the switching kinetics of polycrystalline ferroelectric thin films, like those of (PVDF-TrFE), are not always met by one particular model like the KAI model, which works well for single crystal ferroelectric samples [46]. For this reason, alternative methods have been proposed to model the polarization switching kinetics of P(VDF-TrFE) thin films.

In polycrystalline ferroelectric samples the polarization switching mechanism in one region does not necessarily expands through the neighboring regions and switch the whole region. To address this issue Tagantsev et al. proposed a model called nucleation-limited-switching (NLS) [68]. This model is also often referred to as region-by-region switching model. In this model, the switching of each region is independently determined by its own nucleation rate and domain dimension. Moreover, unlike the KAI model in which the switching of the whole system is controlled by domain expansion, in the region-by-region model, the polarization switching of the whole system is controlled by the statistics of domain nucleation in each region [68]. This model is found to be a reasonable description of the ferroelectric switching process with a good agreement between the experimental data and the proposed model [46]. Another model proposed that the broadening of the switching time distribution is based on the significant surface roughness associated with decreased film thickness, which in turn leads to a non-uniform electric field distribution and thus resulting in different values of switching time in different regions [69]. For example, Nakajima et al. have shown that the switching time distribution of P(VDF-TrFE) (75/25) at electric field of 120 MV/m, is broader for a 50 nm thick film compared to a 330 nm thick film, in agreement with the proposed model [69]. In addition, these authors reported a switching time of 20 ns for a 50 nm thick sample with the above mentioned conditions.

The voltage required to reverse the polarization is proportional to the film thickness. Thus, for lower switching voltages, the film thickness has to be reduced. Two-dimensional ferroelectric P(VDF-TrFE) films as thin as 1 nm (two monolayers) are typically deposited by the Langmuir-Blodgett (LB) technique [70]. On the other hand, Zhang et al.[71] showed that below a certain critical thickness the ferroelectric property of P(VDF-TrFE) is deteriorated. Recently, our group and others have shown that by using a simple nano-imprint lithography technique, arrays of nano-dots of ferroelectric polymer can be fabricated [61, 72-75]. In doing so, not only nano-patterns are created, but also the orientation of the chain axis, about which the dipole moment rotates, is aligned in a direction parallel to the substrate [61]. As a result, the coercive field was found to decrease from ~50 MV/m to ~10 MV/m. These results can ultimately help to realize an easily processable, low-voltage, high-density (33 Gbits/in^2), and low-cost non-volatile ferroelectric memory. Confining ferroelectric polymers into nanocavities by wetting nanoporous alumina templates to produce nanorods has also shown an improvement of ferroelectric properties due to the favorable molecular orientation of P(VDF-TrFE).

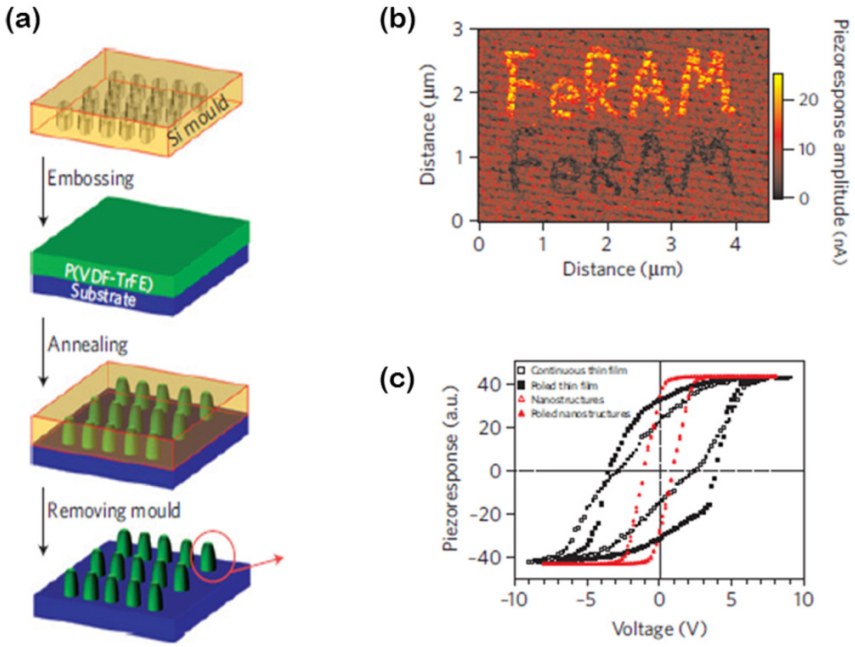

Figure 2.13: Nanostructures of P(VDF-TrFE) produced by nano-imprint lithography (a). Information can be written (polarized) and reversed by applying an opposing voltage, which remains stable after one day poling (b). The nanostructures have a lower coercive field (10 MV/m), i.e., well below the one of the continuous thin film (c) [61].

The appealing and promising findings like the one shown in Figure 2.13 are the driving reasons to begin this thesis, to study further the exact reasons for the dramatic improvement of molecular orientation during nanoconfinement and the resulting decreased coercive field. Before entering in the description of our

work, a short summary of ferroelectric-based organic memories is presented in the next section, in order to illustrate a typical use of this polymer.

2.4. Organic Ferroelectric Memories

As stated in the earlier sections of this chapter ferroelectric polymer memories have a large potential to enter into the memory market [15]. In recent years, with the better understanding and advances made about ferroelectric polymers, a variety of memory device architectures have been proposed [18, 20-22, 30]. Nevertheless, ferroelectric polymers are also proposed for other applications like in those of light emitting transistors [76] and flexible actuators [77]. In the subsequent section, a brief overview of the well developed and important memory elements based on ferroelectricity such as ferroelectric capacitor, field-effect transistor, and diodes are presented.

2.4.1 Ferroelectric Capacitors

A ferroelectric capacitor is the simplest memory device, fabricated by sandwiching a ferroelectric layer between two electrodes [78]. Information is stored by applying a sufficiently large bias to align the polarization in one of two stable states. The general working principle of ferroelectric capacitors was presented earlier in this chapter as one typical example of FeRAMs (see *section 2.2*). One of the challenges in these kinds of memories is the higher coercive voltage associated with larger thin film thickness [24, 79]. In order to decrease the coercive voltage, it is desirable to decrease the thickness, which is often accompanied by shortcuts between electrodes due to pinholes in the film.

Commonly used solutions include optimized annealing conditions [46] and finding specific spin-coating conditions [35].

For example, Muller et al. have shown that by using Si/SiO_2 as a bottom substrate and by mechanically pressing indium as a top electrode, the ferroelectric properties of spin-coated ultrathin (about 10 nm) films are well preserved [80]. In addition, using chemically inert elements like gold instead of the more reactive aluminum electrodes is reported to result in improved switching kinetics [30]. This was explained on the basis of the interaction of aluminum with the P(VDF-TrFE) forming nonferroelectric or "dead" layers. Another interesting finding to improve the ferroelectric properties of spin-coated P(VDF-TrFE) copolymers of sub-100 nm-thick film is using a conductive polymer as a bottom and top interface or using vapor-deposited gold as top electrode [81]. One disadvantage of using ferroelectric capacitors is related to the need for the reduction of capacitor area for higher memory density, since the charge displacement response (current during switching, I) scales with P_r, capacitor area A and switching time t as $I = (P_rA)/t$ [23, 30]. Thus, downscaling in area lowers the signal response, making it difficult to detect the signal reliably.

2.4.2 Ferroelectric Field-effect Transistors

Compared to capacitor-type designs, transistor memories provide non-destructive read-out for stable sensing, which originates from their working mechanism [37]. A typical ferroelectric field-effect transistor (FeFET) consists of a metal-ferroelectric-semiconductor layer stack, and source (S), drain (D), and gate (G) electrodes as illustrated in Figure 2.14 [21, 38, 82, 83]. In FeFETS the ferroelectric insulator serves as a gate dielectric. The need to use a ferroelectric

layer in the transistors arises from the presence of two stable polarization states (hysteresis), which induces positive or negative charges in the semiconductor layer [84].

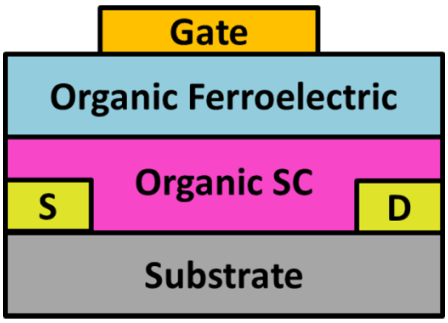

Figure 2.14: Schematic representation of a typical top-gate/bottom-contact organic ferroelectric field-effect transistor (FeFET). SC stands for semiconductor.

By applying sufficiently large gate bias, the ferroelectric polarizations induce either a high or a low semiconductor channel conductance, causing a positive or negative onset voltage shift of the transistor [23, 30]. Measuring the (drain) current response by applying a low drain voltage can be used to define the binary "0" and "1" states, providing the basis for nonvolatile memory functionality with nondestructive readout [20, 84]. In 2005 Naber et al. demonstrated a rewritable, non-volatile ferroelectric field-effect transistor (FeFET) memory device made with a P(VDF-TrFE) ferroelectric copolymer and a MEH-PPV (poly[2-methoxy-5-(2-ethyl-hexyloxy)-*p*-phenylene-vinylene]) as a semiconductor material, Figure 2.15 [21]. Nevertheless, the 60V and higher operating voltage is too large for the realization of low-voltage all-organic

memory device. For this reason various research activities are ongoing to reduce the programming voltage, which are summarized in the following review papers [23, 30] and in a recent Ph.D thesis [85]. Even if FeFETs possess good advantages as mentioned above, the device structure appears more difficult to fabricate large integrated memory than for example ferroelectric capacitors.

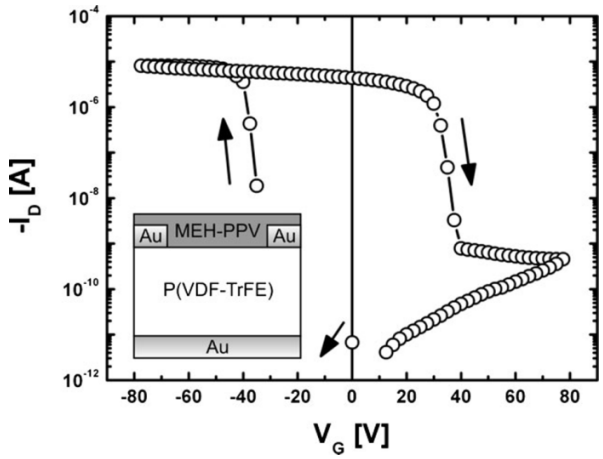

Figure 2.15: A transfer measurement on an organic FeFET using P(VDF-TrFE) as a gate dielectric material, demonstrating a high/low drain current corresponding to a negative/positive gate bias respectively [21].

2.4.3 Ferroelectric Diodes

The other type of ferroelectric memories consists of diodes that combine the architectural simplicity of ferroelectric capacitors, but uses a resistive reading scheme, making them a memory device with a non-destructive read-out capability like FeFETs [30]. A ferroelectric diode memory consisting of phase-separated films of P(VDF-TrFE) and polymer semiconductor P3HT [poly(3-hexylthiophene)] was demonstrated in 2008 by Asadi et al [39].

The working principle of ferroelectric diodes takes advantage of the polarization state to modulate the depletion width of the diode [86]. By applying a voltage higher than the coercive voltage, the ferroelectric layer gets polarized, by which opposite charges are accumulated at the ferroelectric-semiconductor interface, leading to band bending in the semiconductor, and subsequently enhanced charge injection [87, 88]. In other words, the increase or decrease of the current (resistance) response in diodes is attributed to changes in the charge injection barrier between the bottom/metal electrode and the semiconducting layer [39]. Thus, the binary states can be used to create nonvolatile memory effect. Like the aforementioned ferroelectric memories, low switching voltage in diodes can be achieved by enhancing the ferroelectric property of P(VDF-TrFE) layer. Therefore, nanoimprinted P(VDF-TrFE) nanostructures with low coercive field as mentioned earlier [61] have a huge potential to be used in these kind of memory device; during the course of this thesis, I collaborated to a project of fabrication of memory diodes made of nanoimprinted P(VDF-TrFE) combined with P3HT [89].

2.5 Summary

In this chapter, the state of the art about organic ferroelectric memories and materials was introduced. The different classes of electronic memories on the basis of their volatility were reviewed in the first part of the thesis. The potential of organic ferroelectric materials as an attractive storage media for non-volatile memories, owing to their high flexibility, low cost, ease of production was highlighted briefly. Then, ferroelectric materials were presented with particular attention to polymer ones. The most promising and studied ferroelectric polymer is P(VDF-TrFE) copolymer, and it is also used in the experimental part of this

thesis. Therefore, the structure and ferroelectric properties of P(VDF-TrFE) was described in more detail. The crystallization of P(VDF-TrFE) in nano-confinement by the method of nano-imprint lithography was disclosed as a promising breakthrough to improve the ferroelectric performance. Finally, three typical organic based ferroelectric architectures were presented to demonstrate low-cost solution-based memory devices, alongside the advantages and limitations of each technology. This places our work into the context of an active, albeit technological, research field.

Chapter 2

Bibliography

1. Pinnow, C.-U. and T. Mikolajick, *Material Aspects in Emerging Nonvolatile Memories.* Journal of the Electrochemical Society, **2004**. 151, K13-K19.

2. Martin, K.W. and K. Martin, *Digital integrated circuit design*. 2000: Oxford University Press; New York.

3. Sheikholeslami, A. and P.G. Gulak, *A survey of circuit innovations in ferroelectric random-access memories.* Proceedings of the IEEE, **2000**. 88, 667-689.

4. Kaufman, B.A., *The Special Issue on High-Speed Memories.* Electronic Computers, IEEE Transactions on, **1966**, 420-422.

5. Prince, B., *Semiconductor memories: a handbook of design, manufacture and application*. 1991: John Wiley & Sons Inc.

6. Ling, Q.-D., D.-J. Liaw, C. Zhu, D.S.-H. Chan, E.-T. Kang, and K.-G. Neoh, *Polymer electronic memories: Materials, devices and mechanisms.* Progress in Polymer Science, **2008**. 33, 917-978.

7. Sharma, A.K., *Advanced semiconductor memories: architectures, designs, and applications*. 2009: Wiley-IEEE Press, Dublin.

8. Asano, H., *Flash non-volatile memory*. 1995, U.S. Patent 5,406,529.

9. Sekitani, T., T. Yokota, U. Zschieschang, H. Klauk, S. Bauer, K. Takeuchi, M. Takamiya, T. Sakurai, and T. Someya, *Organic Nonvolatile Memory Transistors for Flexible Sensor Arrays.* Science, **2009**. 326, 1516-1519.

10. Daughton, J.M., *Magnetoresistive memory technology.* Thin Solid Films, **1992**. 216, 162-168.

11. Boeck, J.D., W.V. Roy, J. Das, V. Motsnyi, Z. Liu, L. Lagae, H. Boeve, K. Dessein, and G. Borghs, *Technology and materials issues in semiconductor-based magnetoelectronics.* Semiconductor Science and Technology, **2002**. 17, 342.

12. Daughton, J., *Chapter 4 - Magnetoresistive random access memories*, in *Magnetoelectronics*, M. Johnson, Editor. 2004, Academic Press: San Diego. p. 205-380.

13. Evans, P.R., X. Zhu, P. Baxter, M. McMillen, J. McPhillips, F.D. Morrison, J.F. Scott, R.J. Pollard, R.M. Bowman, and J.M. Gregg, *Toward Self-Assembled Ferroelectric Random Access Memories: Hard-Wired Switching Capacitor Arrays with Almost Tb/in.2 Densities.* Nano Letters, **2007**. 7, 1134-1137.

14. Das, S. and J. Appenzeller, *FETRAM. An Organic Ferroelectric Material Based Novel Random Access Memory Cell.* Nano Letters, **2011**. 11, 4003-4007.

15. Scott, J.F., *Applications of modern ferroelectrics.* Science, **2007**. 315, 954-959.

16. Takasu, H., *Ferroelectric memories and their applications.* Microelectronic Engineering, **2001**. 59, 237-246.

17. Dawber, M., K.M. Rabe, and J.F. Scott, *Physics of thin-film ferroelectric oxides.* Reviews of Modern Physics, **2005**. 77, 1083-1130.

18. Youn Jung, P., B. In-sung, K. Seok Ju, C. Jiyoun, and P. Cheolmin, *Control of thin ferroelectric polymer films for non-volatile memory applications.* Dielectrics and Electrical Insulation, IEEE Transactions on, **2010**. 17, 1135-1163.

19. Eaton, S.S., D.B. Butler, M. Parris, D. Wilson, and H. McNeillie. *A Ferroelectric Nonvolatile Memory*. in *Solid-State Circuits Conference, 1988. Digest of Technical Papers. ISSCC. 1988 IEEE International*. 1988.

20. Brondijk, J.J., K. Asadi, P.W.M. Blom, and D.M. de Leeuw, *Physics of organic ferroelectric field-effect transistors.* Journal of Polymer Science Part B: Polymer Physics, **2012**. 50, 47-54.

21. Naber, R.C.G., C. Tanase, P.W.M. Blom, G.H. Gelinck, A.W. Marsman, F.J. Touwslager, S. Setayesh, and D.M. de Leeuw, *High-performance solution-processed polymer ferroelectric field-effect transistors.* Nat Mater, **2005**. 4, 243-248.

22. Yang, Y., J. Ouyang, L. Ma, R.J.H. Tseng, and C.W. Chu, *Electrical Switching and Bistability in Organic/Polymeric Thin Films and Memory Devices.* Advanced Functional Materials, **2006**. 16, 1001-1014.

23. Heremans, P., G.H. Gelinck, R. Müller, K.-J. Baeg, D.-Y. Kim, and Y.-Y. Noh, *Polymer and Organic Nonvolatile Memory Devices.* Chemistry of Materials, **2011**. 23, 341-358.

24. Fujisaki, S., H. Ishiwara, and Y. Fujisaki, *Low-voltage operation of ferroelectric poly(vinylidene fluoride-trifluoroethylene) copolymer capacitors and metal-ferroelectric-insulator-semiconductor diodes.* Applied Physics Letters, **2007**. 90, -.

25. Valasek, J., *Piezo-Electric and Allied Phenomena in Rochelle Salt.* Physical Review, **1921**. 17, 475-481.

26. Furukawa, T., *Ferroelectric properties of vinylidene fluoride copolymers.* Phase Transitions, **1989**. 18, 143-211.

27. Horiuchi, S., Y. Tokunaga, G. Giovannetti, S. Picozzi, H. Itoh, R. Shimano, R. Kumai, and Y. Tokura, *Above-room-temperature ferroelectricity in a single-component molecular crystal.* Nature, **2010**. 463, 789-792.

28. Horiuchi, S., F. Kagawa, K. Hatahara, K. Kobayashi, R. Kumai, Y. Murakami, and Y. Tokura, *Above-room-temperature ferroelectricity and antiferroelectricity in benzimidazoles.* Nature Communications, **2012**. 3, 1308.

29. Scott, J.F., *Ferroelectrics go bananas.* Journal of Physics: Condensed Matter, **2008**. 20, 021001.

30. Naber, R.C.G., K. Asadi, P.W.M. Blom, D.M. de Leeuw, and B. de Boer, *Organic Nonvolatile Memory Devices Based on Ferroelectricity.* Advanced Materials, **2010**. 22, 933-945.

31. Asadi, K., M. Li, P.W.M. Blom, M. Kemerink, and D.M. de Leeuw, *Organic ferroelectric opto-electronic memories.* Materials Today, **2011**. 14, 592-599.

32. Kawai, H., *The piezoelectricity of poly (vinylidene fluoride).* Japanese Journal of Applied Physics, **1969**. 8, 975-976.

33. Kepler, R. and R. Anderson, *Ferroelectricity in polyvinylidene fluoride.* Journal of Applied Physics, **1978**. 49, 1232-1235.

34. Lovinger, A.J., *Ferroelectric Polymers.* Science, **1983**. 220, 1115-1121.

35. Setter, N., D. Damjanovic, L. Eng, G. Fox, S. Gevorgian, S. Hong, A. Kingon, H. Kohlstedt, N.Y. Park, G.B. Stephenson, I. Stolitchnov, A.K. Taganstev, D.V. Taylor, T. Yamada, and S. Streiffer, *Ferroelectric thin films: Review of materials, properties, and applications.* Journal of Applied Physics, **2006**. 100, 051606-051606-46.

36. Kusuma, D.Y. and P.S. Lee, *Ferroelectric Tunnel Junction Memory Devices made from Monolayers of Vinylidene Fluoride Oligomers.* Advanced Materials, **2012**. 24, 4163-4169.

37. Baeg, K.-J., D. Khim, J. Kim, B.-D. Yang, M. Kang, S.-W. Jung, I.-K. You, D.-Y. Kim, and Y.-Y. Noh, *High-Performance Top-Gated Organic Field-Effect Transistor Memory using Electrets for Monolithic*

Printed Flexible NAND Flash Memory. Advanced Functional Materials, **2012**. 22, 2915-2926.

38. Wen, Z., C. Li, D. Wu, A. Li, and N. Ming, *Ferroelectric-field-effect-enhanced electroresistance in metal/ferroelectric/semiconductor tunnel junctions.* Nat Mater, **2013**. 12, 617-621.

39. Asadi, K., D.M. de Leeuw, B. de Boer, and P.W.M. Blom, *Organic non-volatile memories from ferroelectric phase-separated blends.* Nat Mater, **2008**. 7, 547-550.

40. Kepler, R.G. and R.A. Anderson, *Ferroelectric polymers.* Advances in Physics, **1992**. 41, 1-57.

41. Nakamura, K.i. and Y. Wada, *Piezoelectricity, pyroelectricity, and the electrostriction constant of poly(vinylidene fluoride).* Journal of Polymer Science Part A-2: Polymer Physics, **1971**. 9, 161-173.

42. Nalwa, H.S., *Ferroelectric polymers: chemistry, physics, and applications*. Vol. 28. 1995: CRC Press.

43. Poulsen, M. and S. Ducharme, *Why ferroelectric polyvinylidene fluoride is special.* Dielectrics and Electrical Insulation, IEEE Transactions on, **2010**. 17, 1028-1035.

44. Meyer, R.B., L. Liebert, L. Strzelecki, and P. Keller, *Ferroelectric liquid crystals.* J. Physique Lett., **1975**. 36, 69-71.

45. Horiuchi, S. and Y. Tokura, *Organic ferroelectrics.* Nat Mater, **2008**. 7, 357-366.

46. Mao, D., B.E. Gnade, and M.A. Quevedo-Lopez, *Ferroelectric Properties and Polarization Switching Kinetic of Poly (vinylidene fluoride-trifluoroethylene) Copolymer*. Ferroelectrics - Physical Effects. 2011.

47. Kepler, R., *Saturation remnant polarization of polyvinylidene fluoride*. 1978, Sandia Labs., Albuquerque, N. Mex.(USA).

48. Huang, C., R. Klein, F. Xia, H. Li, Q.M. Zhang, F. Bauer, and Z.Y. Cheng, *Poly(vinylidene fluoride-trifluoroethylene) based high performance electroactive polymers*. Dielectrics and Electrical Insulation, IEEE Transactions on, **2004**. 11, 299-311.

49. Li, M., H.J. Wondergem, M.-J. Spijkman, K. Asadi, I. Katsouras, P.W.M. Blom, and D.M. de Leeuw, *Revisiting the δ-phase of poly(vinylidene fluoride) for solution-processed ferroelectric thin films*. Nat Mater, **2013**. 12, 433-438.

50. Davis, G.T., J.E. McKinney, M.G. Broadhurst, and S.C. Roth, *Electric-field-induced phase changes in poly(vinylidene fluoride)*. Journal of Applied Physics, **1978**. 49, 4998-5002.

51. Lando, J.B. and W.W. Doll, *The polymorphism of poly(vinylidene fluoride). I. The effect of head-to-head structure*. Journal of Macromolecular Science, Part B, **1968**. 2, 205-218.

52. Lando, J., H. Olf, and A. Peterlin, *Nuclear magnetic resonance and x‐ray determination of the structure of poly (vinylidene fluoride)*. Journal of Polymer Science Part A-1: Polymer Chemistry, **1966**. 4, 941-951.

53. Lovinger, A.J., T. Furukawa, G.T. Davis, and M.G. Broadhurst, *Curie transitions in copolymers of vinylidene fluoride.* Ferroelectrics, **1983**. 50, 227-236.

54. Park, Y.J., S.J. Kang, C. Park, K.J. Kim, H.S. Lee, M.S. Lee, U.-I. Chung, and I.J. Park, *Irreversible extinction of ferroelectric polarization in P(VDF-TrFE) thin films upon melting and recrystallization.* Applied Physics Letters, **2006**. 88, 242908-242908.

55. Yagi, T., M. Tatemoto, and J.-i. Sako, *Transition Behavior and Dielectric Properties in Trifluoroethylene and Vinylidene Fluoride Copolymers.* Polym J, **1980**. 12, 209-223.

56. Ma, W., J. Zhang, and X. Wang, *Crystallizaion and surface morphology of poly(vinylidene fluoride)/poly(methylmethacrylate) films by solution casting on different substrates.* Applied Surface Science, **2008**. 254, 2947-2954.

57. Lovinger, A.J., T. Furukawa, G.T. Davis, and M.G. Broadhurst, *Crystallographic changes characterizing the Curie transition in three ferroelectric copolymers of vinylidene fluoride and trifluoroethylene: 2. Oriented or poled samples.* Polymer, **1983**. 24, 1233-1239.

58. Tashiro, K., K. Takano, M. Kobayashi, Y. Chatani, and H. Tadokoro, *Structure and ferroelectric phase transition of vinylidene fluoride-trifluoroethylene copolymers: 2. VDF 55% copolymer.* Polymer, **1984**. 25, 195-208.

59. Murata, Y. and N. Koizumi, *Curie Transition in Copolymers of Vinylidene Fluoride and Tetrafluoroethylene.* Polymer Journal **1985**. 17, 1071-1074.

60. Baltá Calleja, F.J., A.G. Arche, T.A. Ezquerra, C.S. Cruz, F. Batallán, B. Frick, and E.L. Cabarcos, *Structure and properties of ferroelectric copolymers of poly(vinylidene fluoride)*, in *Structure in Polymers with Special Properties*, H.G. Zachmann, Editor. 1993, Springer Berlin Heidelberg. p. 1-48.

61. Hu, Z., M. Tian, B. Nysten, and A.M. Jonas, *Regular arrays of highly ordered ferroelectric polymer nanostructures for non-volatile low-voltage memories.* Nat Mater, **2009**. 8, 62-67.

62. Faria, L.O. and R.L. Moreira, *Infrared spectroscopic investigation of chain conformations and interactions in P(VDF-TrFE)/PMMA blends.* Journal of Polymer Science Part B: Polymer Physics, **2000**. 38, 34-40.

63. Guo, D. and N. Setter, *Impact of Confinement-Induced Cooperative Molecular Orientation Change on the Ferroelectric Size Effect in Ultrathin P(VDF-TrFE) Films.* Macromolecules, **2013**. 46, 1883-1889.

64. Guo, D., I. Stolichnov, and N. Setter, *Thermally induced cooperative molecular reorientation and nanoscale polarization switching behaviors of ultrathin poly(vinylidene fluoride-trifluoroethylene) films.* J Phys Chem B, **2011**. 115, 13455-66.

65. Wu, Y., X. Li, Y. Weng, Z. Hu, and A.M. Jonas, *Orientation of lamellar crystals and its correlation with switching behavior in ferroelectric*

P(VDF-TrFE) ultra-thin films. Polymer, **2014**, http://dx.doi.org/10.1016/j.polymer.2014.01.004.

66. Mao, D., M.A. Quevedo-Lopez, H. Stiegler, B.E. Gnade, and H.N. Alshareef, *Optimization of poly(vinylidene fluoride-trifluoroethylene) films as non-volatile memory for flexible electronics.* Organic Electronics, **2010**. 11, 925-932.

67. Sharma, P., T.J. Reece, S. Ducharme, and A. Gruverman, *High-Resolution Studies of Domain Switching Behavior in Nanostructured Ferroelectric Polymers*. Nano Letters, **2011**. 11, 1970-1975.

68. Tagantsev, A.K., I. Stolichnov, N. Setter, J.S. Cross, and M. Tsukada, *Non-Kolmogorov-Avrami switching kinetics in ferroelectric thin films.* Physical Review B, **2002**. 66, 214109.

69. Takashi, N., A. Ryosuke, T. Yoshiyuki, and F. Takeo, *Intrinsic Switching Characteristics of Ferroelectric Ultrathin Vinylidene Fluoride/Trifluoroethylene Copolymer Films Revealed Using Au Electrode.* Japanese Journal of Applied Physics, **2005**. 44, L1385.

70. Bune, A.V., V.M. Fridkin, S. Ducharme, L.M. Blinov, S.P. Palto, A.V. Sorokin, S.G. Yudin, and A. Zlatkin, *Two-dimensional ferroelectric films.* Nature, **1998**. 391, 874-877.

71. Zhang, Q.M., H. Xu, F. Fang, Z.-Y. Cheng, F. Xia, and H. You, *Critical thickness of crystallization and discontinuous change in ferroelectric behavior with thickness in ferroelectric polymer thin films.* Journal of Applied Physics, **2001**. 89, 2613-2616.

72. Kang, S.J., Y.J. Park, J.Y. Hwang, H.J. Jeong, J.S. Lee, K.J. Kim, H.C. Kim, J. Huh, and C. Park, *Localized Pressure-Induced Ferroelectric Pattern Arrays of Semicrystalline Poly(vinylidene fluoride) by Microimprinting.* Advanced Materials, **2007**. 19, 581-586.

73. Zhang, L., S. Ducharme, and J. Li, *Microimprinting and ferroelectric properties of poly(vinylidene fluoride-trifluoroethylene) copolymer films.* Applied Physics Letters, **2007**. 91, 172906-172906.

74. Hu, Z., G. Baralia, V. Bayot, J.-F. Gohy, and A.M. Jonas, *Nanoscale Control of Polymer Crystallization by Nanoimprint Lithography.* Nano Letters, **2005**. 5, 1738-1743.

75. Hu, Z. and A.M. Jonas, *Control of crystal orientation in soft nanostructures by nanoimprint lithography.* Soft Matter, **2010**. 6, 21-28.

76. Li, X., A.J.J.M. van Breemen, V. Khikhlovskyi, E.C.P. Smits, M. Kemerink, D.J. Broer, and G.H. Gelinck, *Programmable polymer light emitting transistors with ferroelectric polarization-enhanced channel current and light emission.* Organic Electronics, **2012**. 13, 1742-1749.

77. Bae, S.-H., O. Kahya, B.K. Sharma, J. Kwon, H.J. Cho, B. Özyilmaz, and J.-H. Ahn, *Graphene-P(VDF-TrFE) Multilayer Film for Flexible Applications.* ACS Nano, **2013**. 7, 3130-3138.

78. Khan, M.A., U.S. Bhansali, and H.N. Alshareef, *Fabrication and characterization of all-polymer, transparent ferroelectric capacitors on flexible substrates.* Organic Electronics, **2011**. 12, 2225-2229.

79. Mao, D., I. Mejia, H. Stiegler, B.E. Gnade, and M.A. Quevedo-Lopez, *Fatigue characteristics of poly(vinylidene fluoride-trifluoroethylene) copolymer ferroelectric thin film capacitors for flexible electronics memory applications.* Organic Electronics, **2011**. 12, 1298-1303.

80. Müller, K., D. Mandal, K. Henkel, I. Paloumpa, and D. Schmeisser, *Ferroelectric properties of spin-coated ultrathin (down to 10 nm) copolymer films.* Applied Physics Letters, **2008**. 93, 112901-112901.

81. Naber, R.C.G., P.W.M. Blom, A.W. Marsman, and D.M. de Leeuw, *Low voltage switching of a spin cast ferroelectric polymer.* Applied Physics Letters, **2004**. 85, 2032-2034.

82. Ng, T.N., B. Russo, B. Krusor, R. Kist, and A.C. Arias, *Organic inkjet-patterned memory array based on ferroelectric field-effect transistors.* Organic Electronics, **2011**. 12, 2012-2018.

83. Naber, R.C.G., J. Massolt, M. Spijkman, K. Asadi, P.W.M. Blom, and D.M. de Leeuw, *Origin of the drain current bistability in polymer ferroelectric field-effect transistors.* Applied Physics Letters, **2007**. 90, 113509-113509.

84. Kam, B., X. Li, C. Cristoferi, E.C.P. Smits, A. Mityashin, S. Schols, J. Genoe, G. Gelinck, and P. Heremans, *Origin of multiple memory states in organic ferroelectric field-effect transistors.* Applied Physics Letters, **2012**. 101, 033304-033304.

85. Kam, B., *Organic Electronics & Memories*. 2014, IMEC, Belgium.

86. Blom, P.W.M., R.M. Wolf, J.F.M. Cillessen, and M.P.C.M. Krijn, *Ferroelectric Schottky Diode.* Physical Review Letters, **1994**. 73, 2107-2110.

87. Asadi, K., M. Li, N. Stingelin, P.W.M. Blom, and D.M. de Leeuw, *Crossbar memory array of organic bistable rectifying diodes for nonvolatile data storage.* Applied Physics Letters, **2010**. 97, 193308-193308.

88. Kemerink, M., K. Asadi, P.W.M. Blom, and D.M. de Leeuw, *The operational mechanism of ferroelectric-driven organic resistive switches.* Organic Electronics, **2012**. 13, 147-152.

89. Nougaret, L., H.G. Kassa, R. Cai, T. Patois, B. Nysten, A.J.J.M. van Breemen, G.H. Gelinck, D.M. de Leeuw, A. Marrani, Z. Hu, and A.M. Jonas, *Nanoscale Design of Multifunctional Organic Layers for Low-Power High-Density Memory Devices.* ACS Nano, **2014**, DOI: 10.1021/nn406503g.

Chapter 3

Fabrication and Characterization of Imprinted Nanostructures

Fabrication of nano-structures with high precision and cheaper cost is one of the major challenges in the production of high-volume nano-system technologies. In this thesis, we have developed and used a variety of nano-fabrication techniques. Nano-structured ferroelectric polymers, i.e., poly(vinylidene fluoride-ran-trifluoroethylene) P(VDF-TrFE) patterns are fabricated by nano-imprint lithography (NIL) and the structural and ferroelectric properties of the resulting patterns are characterized by different techniques. Since a significant part of the thesis was devoted on producing nano-structured hard molds and developing a versatile ferroelectric characterization technique in our laboratory, one chapter is dedicated to present the details of the technologies used. Thus, it is one of the main parts of the thesis.

In the first part of this chapter, the fabrication by electron beam lithography (EBL) of nano-structured hard molds for the NIL experiments is presented. We have also investigated the potential of block copolymer lithography (BCL) to

fabricate molds of large active area. The second section of this chapter is dedicated to the use of nano-imprint lithography to produce arrays of ferroelectric copolymers. Finally, the various characterization techniques are discussed, with an emphasis on the study of the ferroelectric properties of nano-patterns by piezoresponse force microscopy (PFM).

3.1 Techniques for Fabrication of Nanostructures

Nanoimprint lithography is a standard fabrication technique to produce nanostructures (patterns) on polymer materials. The particular interest of using NIL in this thesis is the potential of this technique to pattern arrays of ferroelectric nanostructures. These nano-patterns are interesting to fabricate devices for memory applications. The NIL process is based on pressing a stamp (nanostructured hard mold) into a heated polymer under pressure. Once the system is cooled and the hard mold is removed, the features of the mold will be transferred to the polymer material. However, nanoimprint lithography is not a self-contained technique. Before doing NIL, imprinting molds with nanometer features have first to be fabricated, which means that other nanofabrication techniques should be introduced. There are various techniques that can be used to fabricate nanostructured molds. The aim of the following section is to introduce the different techniques that are used in this thesis to produce nano-structured imprinting molds. In this context current applications and limitations of each technique compared with other nanofabrication methods are discussed.

3.2 Selection of Mold Fabrication Technologies

The main issues that should be considered to select a fabrication technology for NIL hard molds are the competitiveness and resolution limits of the process. Molds with small feature sizes can be fabricated using a variety of methods like optical lithography, nano-imprint lithography (NIL), electron beam lithography (EBL), or block copolymer lithography (BCL). Among these techniques, EBL and BCL are the ones used widely to produce features of nanometer size (features to a few hundreds of nm). Initially the principles and practical steps of hard mold fabrication by EBL are discussed in detail. Then the option of BCL technology to fabricate imprinting hard molds is discussed.

3.2.1 Electron Beam Lithography (EBL)

Electron Beam Lithography (EBL) has been one of the most developed fabrication techniques to achieve nano- and micro-patterns for over 50 years [1-4]. This technique is often used to fabricate masks for optical lithography or hard molds for nanoimprint lithography. In our case, EBL is used to fabricate imprinting molds of different feature sizes and shapes. Here, the basic principles of EBL are first presented. Then, the actual process parameters of the hard mold fabrication are discussed in detail.

EBL is a “conventional” method which operates based on the principle of “top-down” lithography techniques. The process itself comprises the use of a highly focused electron beam to modify the solubility of a resist material so that patterns are created once the resist is developed in the right solvent. Areas that are either exposed or not depending on the tone of the resist are removed during development step.

As a comparison to the EBL technology lets us highlight optical lithography, a standard method for manufacturing in the microelectronics industry. In the case of photolithography, first, an organic photoresist is spin-coated on the top of a wafer. Then, the resist is exposed through a patterned mask by a high energy short-wavelength light (typically, UV light) [5]. It should be noted that the photo mask needs to be prepared by another lithography technique like EBL. When the exposed photoresist is immersed in solvents that dissolve the exposed (positive photoresist) or unexposed (negative photoresist), the surface of the substrate is accessed. Finally, processes like metal deposition, lift-off and etching of the underlying substrate are done to complete the transfer of the image of the drawing to the wafer. The time and cost required to fabricate the photo mask is a significant drawback of photolithography fabrication techniques. The final resolution and quality of the resulting structure depend on the wavelength of the light source, the type of photoresist used, and the process and technology itself [5].

The working principle of EBL resembles the one of optical lithography except that light is used in the later technique to modify the nature of the resist. The use of electrons to write the patterns increases the resolution limit of EBL. This is one significant advantage of EBL technique over the other methods. In addition, because no mask is needed to project the patterns on the electron-sensitive resist, EBL is also known as a mask-less lithography technique.

The size of the patterns produced by EBL varies from a few nanometers to several micrometers [6-8]. The direct writing technology used by EBL has the advantage of fabricating high resolution patterns of arbitrary shapes. However, this in turn results into one of the main drawbacks of EBL systems, i.e., low throughput. This is because the serial writing of patterns by electrons takes time

to write large and complex structures. Thus, it is an expensive technique for the fabrication of larger surface areas.

The fabrication of nano-features by EBL on hard (like silicon oxide) substrates follows almost the same kind of process as that of optical lithography. Figure 3.1 is a scheme of a complete process for the fabrication of line patterns in a silicon oxide layer. The process typically begins by spin-coating a thin electron sensitive resist layer on a Si-substrate with a layer of thermally grown oxide, whose thickness will define the height of the protrusions of the final mold (Figure 3.1(3)). The pre-defined design on the computer is transferred into the lithography equipment. These designs are then written on the resist material by a focused electron beam (Figure 3.1(4)). The usual resists used in EBL are thin films of polymers dissolved in solvent. When the resist is exposed by an electron beam, the longer polymer chains are broken into fragments of shorter molar mass. Once the exposed resist is immersed in a developer, the degraded components dissolve faster than the unexposed ones. The increase in solubility is due to a difference of chain lengths between the exposed region and the unexposed ones. This ultimately creates a pattern in the resist film. These created contrasts can be used as a mask to transfer the pattern into the substrate (Figure 3.1(4)). After development, a thin layer of metal is often deposited (Figure 3.1(5)) to achieve lift off, in so doing, the remaining resist and metal deposited on unexposed parts are removed.

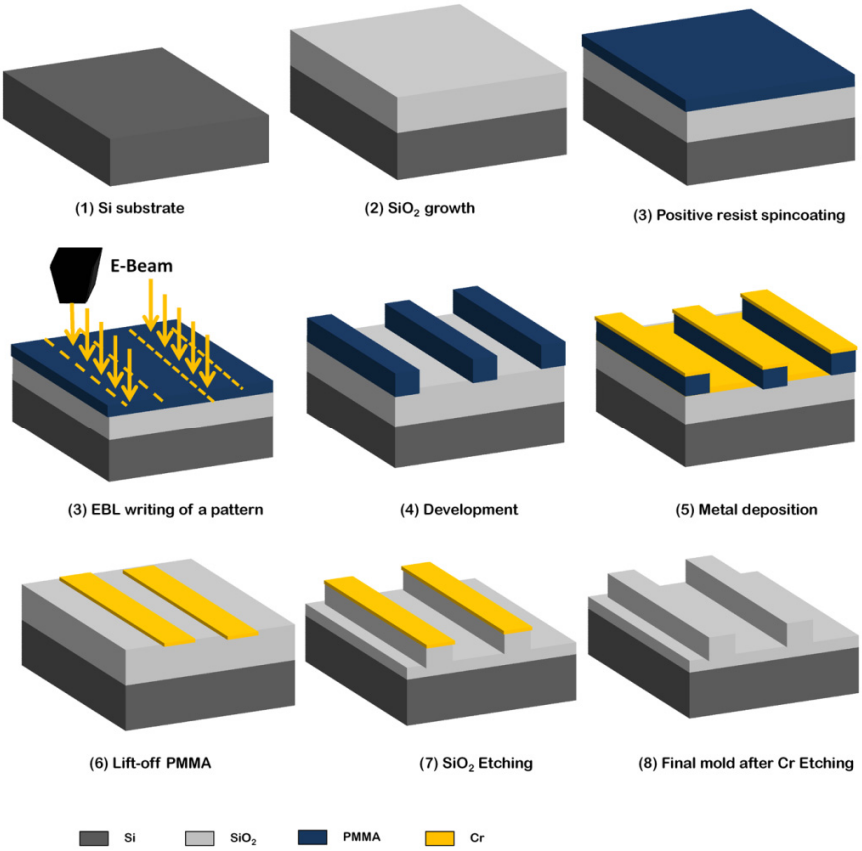

Figure.3.1: Schematic illustration of process flow for the fabrication of hard molds by electron beam lithography (EBL). (1-3) show the sample preparation steps and (4-8) show the fabrication steps from e-beam exposure up to the ultimate pattern transfer to the silicon oxide layer.

As Figure 3.1(7) and (8) shows, reactive ion etching (RIE) and etching the remaining metal completes the fabrication process of hard molds by the EBL process.

It is noteworthy to mention here that the interaction of the electrons with the resist creates complexity. The elastic collisions of the electrons within the resist deflect the electron slightly. This forward scattering broadens the beam. The effect of this broadening is less pronounced if the thickness of the resist is decreased. Especially this effect is noticeable when low energy electrons are used to write patterns. The other serious problem during EBL writing is the recurrence (backscattering) of some electrons into the resist after large angle collisions within the substrate. This second scattering causes a phenomenon called proximity effect which causes pattern distortion and overexposure [3, 4]. The proximity effects can be minimized by using low energy electrons.

In addition, even though an EBL is a favorable technique for the fabrication of patterns with high density, high resolution and high reliability, it is also a complex process with many interacting parameters that can affect the quality of the resulting nanostructures and the robustness of the process [3]. Especially, fabricating nanostructures with high pattern density is very tricky. The most common parameters that need to be controlled to achieve high resolution patterns include the exposure energy, the nature of the resist, the resist thickness, the dose and the development time. If one or more of these parameters are not optimized, the final structure will be very different from the expected result. That is also why mastering the technique is not easy for a beginner even though the principle of EBL appears to be easy and straightforward.

To sum up, electron beam lithography is a versatile and convenient tool to fabricate nanostructured hard molds. Due to these advantages, we used EBL to fabricate hard molds that can be used to perform nanoimprint lithography (NIL). In the next section, the full electron beam lithography procedure carried out in this work is presented in some detail.

3.2.2 Mold Fabrication by Electron Beam Lithography

To fabricate the hard molds by electron beam lithography (EBL), a Philips XL 30S FEG scanning electron microscope (SEM) equipped with an Elphy plus (Raith) pattern generator lithography module is used (Figure 3.2). This EBL system operates at spot 1 and aperture 7 which gives a minimum current at an acceleration voltage of 30 kV. The whole EBL process starts by growing a thin silicon oxide layer by thermal oxidation on a silicon substrate. The thickness of the SiO_2 is controlled on the basis of the depth of the final mold cavities. For example, to fabricate 150 nm deep cavities, the initial thickness of the deposited silicon oxide layer should be at least 150 nm. In this thesis, either a 100 nm or a 150 nm thick SiO_2 are often deposited on the Si substrates. Then, a thin layer of resist is spin-coated on the thermally deposited oxide layer. The standard and widely used resist for e-beam is polymethyl methacrylate (PMMA) which was initially reported by IBM [9].

Figure 3.2: Electron lithography system of Philips XL 30S FEG SEM equipped with a RAITH lithography module.

Controlling the thickness of the PMMA resist (usually a thin layer) is very crucial to optimize the resolution of the resulting patterns. We make use of a 2% PMMA solution of 130 K molar mass, in toluene solvent. PMMA was spin-coated at 2000 rpm onto a cleaned SiO_2 layer and annealed for 1 h at 150^{o}C to give around 90 nm thick films. The next step is to put these samples inside the EBL equipment. Squares of different size are drawn on the computer with the ELPHY software. We experimented two ways of obtaining square patterns on the molds, either by direct exposure of squares (Figure 3.3(a)) or by exposing crossed lines as described in (Figure 3.3(b)).

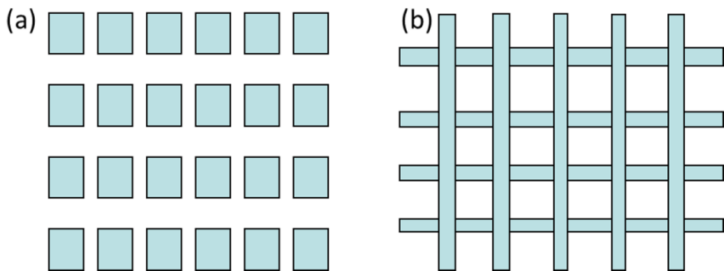

Figure 3.3: Schematic showing the two tested ways of exposing the resist to get square shaped nano-features.

Direct exposure of squares (Figure 2.3(a)) was not found to be successful to produce the intended square cavity hard molds, thus it is not used as a reliable way of fabricating nanostructured molds. One example of a mold fabricated using this route along with some discussion is presented in Appendix, Figure A1 of the thesis. Therefore, we started to work on a second way of exposing the resist, i.e., irradiating an array of intersecting lines which follow the perimeter of squares (Figure 3.3(b)). The rest of discussion and results are based on this second method.

Before inserting the sample in the lithography system, often a scratch is made at one corner of the substrate to be used as a reference to move the stage. This scratch is also used to perform focusing of the beam on the resist. Focusing of the electron beam is a crucial step to achieve small size features and reproducible results. The focusing is done by moving the stage on which the sample is mounted in the *z*-direction, while the astigmatism is corrected by moving the stage laterally (*x, y*). The final stage of the focus correction is burning a contamination dot. A small, circular, and clear contamination dot infers that a good focusing is achieved. Once a good focusing is achieved, the resist is exposed using the already prepared design on the computer. The design should be converted into the appropriate format of the lithography module. Typically, the "Generic Pattern Format "(".gpf") is used for our EBL system.

The resist is irradiated by the beam of electrons at varying doses usually between 150 - 200 μC/cm^2. These operating doses are selected on the basis of the electron beam energy, pattern density and size, and also the resist thickness (Appendix, Figure A2). For example, to make smaller features on the PMMA resist, lower electron doses are used.

After writing the pattern by an electron beam, the resist is typically immersed in a liquid developer to dissolve the fragments. The duration and temperature of development plays a role in deciding the resolution and pattern quality because the produced contrast is a function of the developer solubilizing power. In our experimental setup, when the sample is immersed in the developer, the irradiated parts of the PMMA are washed away by a 1:3 MIBK: IPA developer (MIBK is Methyl Isobutyl Ketone and IPA is Isopropyl Alcohol). The development is performed at a room temperature for 90 seconds in the MIBK: IPA developer followed by 30 seconds of rinsing in IPA.

Figure 3.4 shows some AFM topography images of e-beam exposed patterns with different sizes after development indicating the exposed lines surrounding islands of unexposed PMMA. These images are selected as examples to only show the adaptability of an EBL technique to write intersecting line patterns as small as 40 nm (Figure 3.4(a)) and as large as 200 nm (Figure 3.4(c)).

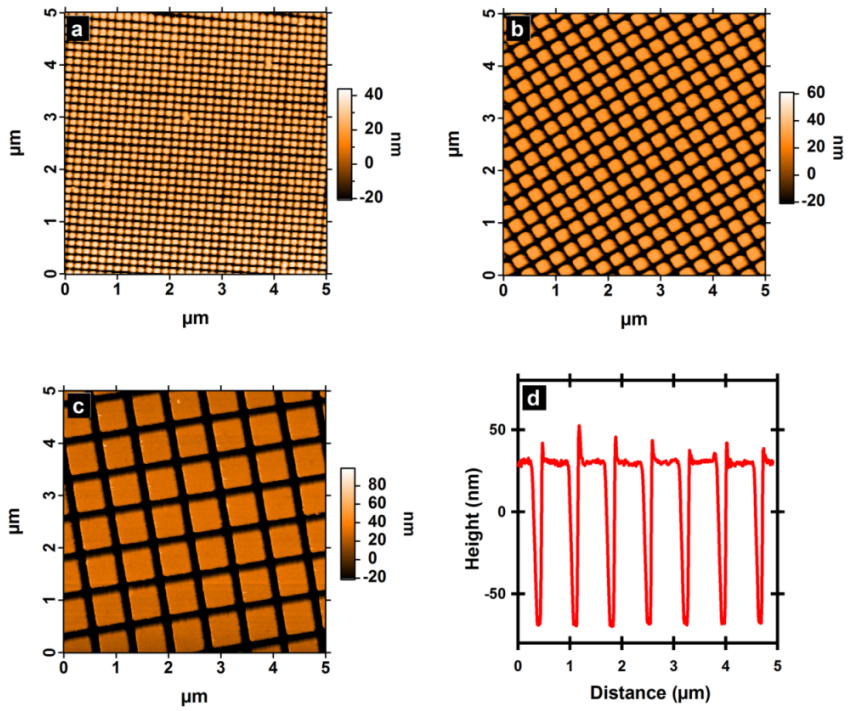

Figure 3.4: Mold fabrication process using PMMA resist by EBL. (a) AFM topography image of exposed resist after development of samples with less than 50 nm exposed lines, (b) 150 nm, and (c) 200 nm. The cross section profile image of (c) is shown in (d). PMMA thickness is 80~100 nm.

(Figure 3.4(b)) displays AFM topography image of developed line patterns of 150 nm in width while (Figure 3.4(d)) is a cross-sectional profile image showing the contrast between the exposed and unexposed areas of the resist. These AFM images confirm that by an electron beam it is indeed possible to create (write) very regular patterns with good precision.

The goal of producing high resolution patterns in the resist is to use the resulting pattern as a mask to fabricate nanostructured SiO_2 hard NIL molds. The most practical method used to transfer these patterns into the hard substrate is by using the lift-off technique [10]. Before undertaking the lift off step, the developed sample is placed inside a metal evaporation chamber where a 10 nm of Cr is deposited perpendicularly to the sample surface, covering the resist and areas in which the resist has been cleared. The thickness of the metal here is selected to be smaller than the standard ratio of 3:1 between the thickness of the resist and that of metal. This ratio is usually reliable for successful lift-off.

After the metallization step, the PMMA is lifted off. During the lift-off, the resist under the film is removed by a solvent, taking the film with it and leaving only the metal which is deposited directly on the substrate. Two types of solvents were tried for the lift-off process. First we immersed the sample in a nitric acid (NHO_3) solution for few minutes followed by dipping in acetic acid solution for a minute. Lift-off is also accomplished by immersing in acetone overnight followed by ultra-sonication for a few minutes. We found that both lift-off solvents give similar results. When the PMMA is lifted off, an array of holes is created in the Cr layer (Figure 3.5). The Cr layer is used as a mask to etch the underneath oxide layer.

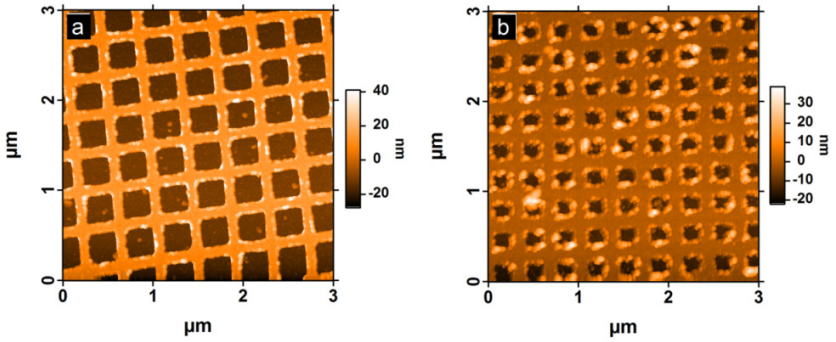

Figure 3.5: AFM image of two samples after metal lift-off in acetone. The imperfection in lift-off is higher in smaller exposed areas (b) than in larger patterns (a)

Etching of the SiO_2 layer is made by thermal reactive ion etching (RIE) for less than 4 minutes in a CHF_3 plasma. Since the etching rate of SiO_2 is around 43 nm/min, about 150 nm deep square holes are obtained (Figure 3.6). It should be mentioned here that, the width of square cavities is the size of the unexposed PMMA islands of Figure 3.4. The remaining Cr outside the nano-structures is washed away by rinsing in a chromium etchant solution. Chromium etchants are typically mixtures of perchloric acid ($HClO_4$), and ceric ammonium nitrate $(NH_4)_2[Ce(NO_3)_6]$.

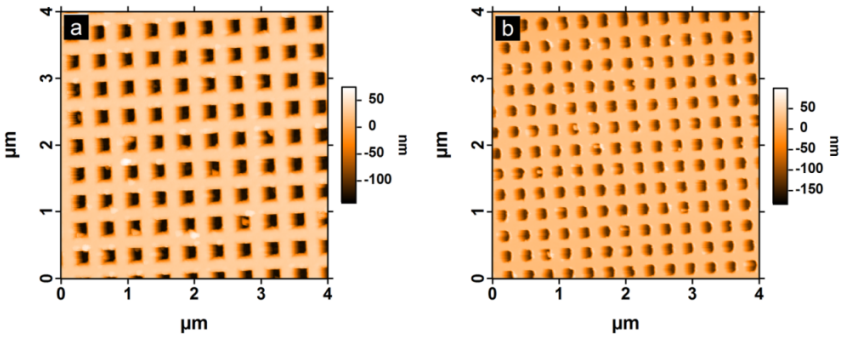

Figure 3.6: AFM topography images of the final square molds fabricated by EBL using a monolayer resist. (a) Cavities of around 250 nm diameter and (b) cavities of less than 200 nm side.

We see some defects at the edge of each nano-cavity in Figure 3.6 because some part of the imperfect metal lift-off. The origin of this defect could be from SiO_2 which was not etched because of the presence of some Cr grains outside the exposed lines. The accumulation of the defects around the square holes is more obvious for samples with higher density of nanostructures like those of smaller square patterns of Figure 3.6(b). The lift-off problem is mainly related to the monolayer electron beam resist (PMMA) used. The main disadvantage of using a monolayer resist is that the metal grains are also deposited on the sidewall of the resist. As a result, some Cr grains stick to and accumulate on the perimeter of the square features even after the resist removal as shown in Figure 3.5. The small metal grains are also visible on the AFM topography images of the final mold (Figure 3.6).

In order to prevent this defect and improve the quality of the lift-off, multiple-layer (usually two layer) resists consisting of a thin imaging layer on top of a thicker under layer can be used to create an undercut profile [10]. Figure 3.7

shows a schematic description of mono-layer and double-layer resist developed samples before and after the metal deposition steps.

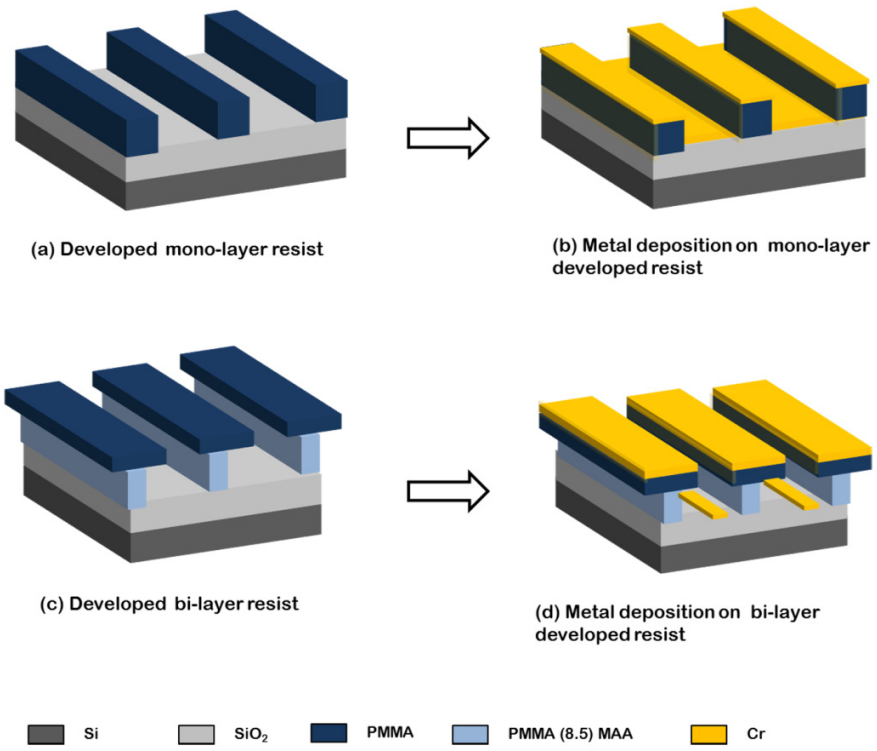

Figure 3.7: Schematic illustration of EBL process using different layers of resist. (a) Developed mono-layer resist, (b) deposition of metal on the monolayer resist, (c) developed resist using double-layer, and (d) metallization process for a double-layer resist. The presence of the underlying copolymer creates higher undercut so that the evaporated metal does not reach the bottom layer.

The adhesion of Cr metal on the sides of the top developed layer is illustrated in Figure 3.7(c); however, the evaporated metal grains cannot reach the bottom layer of the double-layer resist (Figure 3.7(d)). Thus, the presence of improved

undercut of the double-layer patterns helps to ensure a clean lift-off and a well-defined metal pattern.

In this thesis work we have also used a double-layer resist to enhance the undercut for metal lift-off. PMMA and its copolymer poly(methylmethacrylate-co-methylacrylic acid) PMMA(8.5)MAA 3% in ethyl lactate (EL) solvent are used to achieve this enhanced undercut. The improved undercut profile is caused by the higher electron sensitivity of PMMA(8.5)MAA layer, thus resulting in a higher dissolution rate in a developer than the top PMMA layer. Initially, about 70 nm of copolymer is spin-coated on a silicon oxide layer. Then the sample is baked in an oven at 140^{o}C for 30 min. Finally a thin layer of PMMA (~50 nm) is spinned over the already deposited layer and is baked all together at 150^{o}C for 30 min.

This double-layer resist is used to make an e-beam exposure with an identical condition as the previously discussed EBL process where a monolayer resist was used. The sample is also developed with MIBK: IPA solvent. As stated earlier the exposed copolymer layer dissolves faster than the top PMMA layer, creating wider openings on the bottom layer than on the top.

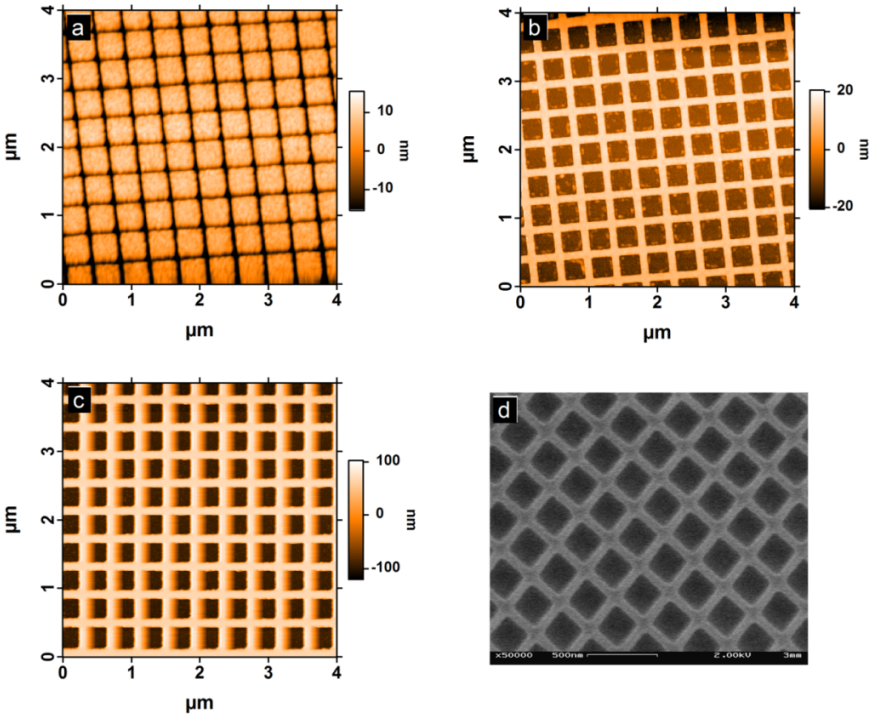

Figure 3.8: Mold fabrication process using a bilayer resist by EBL. (a) AFM topography image of developed bilayer resist, (b) lifting-off a Cr layer, (c) the final square mold obtained by EBL, (d) SEM image of the final mold.

Some results of an EBL process using the double-layer resist are shown in Figure 3.8. The AFM topography images of the developed resist (Figure 3.8(a)) do not show the underlying layer; hence it looks exactly the same as the topography images of the developed resist using the mono-layer shown earlier. A successful lift-off of the Cr metal is achieved by using the double-layer resists (Figure 3.8(b)). An AFM topography image of the final SiO_2 hard mold after thermal reactive ion etching (RIE) and etching the remnant Cr is presented in

(Figure 3.8(c)). SEM image of the final hard mold is also shown in Figure 3.8(d) to complement the AFM images. These results demonstrates that even if the AFM topography images of double-layer patterns look identical to the patterns obtained via the mono-layer, there are no more defects on the edge of the nano-cavities after the lift-off process (Figure 3.8(b)) and the in final molds as well (Figure 3.8(c & d)).

We have also used the bilayer resist process to fabricate molds having line patterns (Figure 3.9(a)). The whole fabrication process is exactly the same as the one discussed for those of the square shaped molds. The only difference is that we have designed and exposed lines instead of an array of intersecting lines which follow the perimeter of squares.

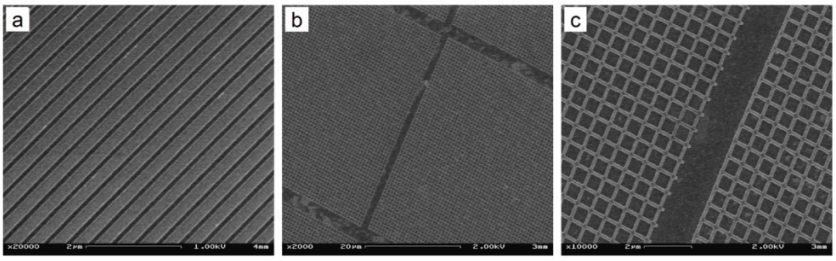

Figure 3.9: SEM image of final hard molds made by EBL. (a) Line patterns, (b) the zoom- out view of big size square molds, and (c) is the zoom in SEM image of (b).

In addition, the EBL technique was used to create nano-structured NIL molds over a much larger surface area (Figure 3.9(b & c)). The SEM image of Figure 3.9(c) shows the zoom out view of the regularly patterned square shaped nano-cavities while Figure 2.3(d) shows the zoom-in view of two neighboring writing

fields. Since EBL exposes patterns serially, it takes a long time to expose patterns of few millimeter scales. For example, it takes ~87 hours to expose a 2.5 mm^2 surface areas.

The only challenge of using the bilayer resists is the formation of shortcuts at the bottom layer when the size of the exposed feature gets smaller and closer to each other. This shortcut appears during the development stage. When the features are closer, the undercut we wanted to achieve became so large that a shortcut was formed and the top layer was displaced. Figure 3.10(a) shows an AFM image of a mold with non-regular (displaced) cavities fabricated using the double-layer resist. In order to prevent this shortcoming, exposing the patterns at a lower dose of electrons was experimented. Nevertheless, this did not prevent the formation of shortcuts. Finally, the time of development in MIBK: IPA solvent was reduced to 60 seconds instead of 90 seconds. The short development time prevented the displacement of patterns. An AFM images showing the effect of development time is presented at Appendix, Figure A3.

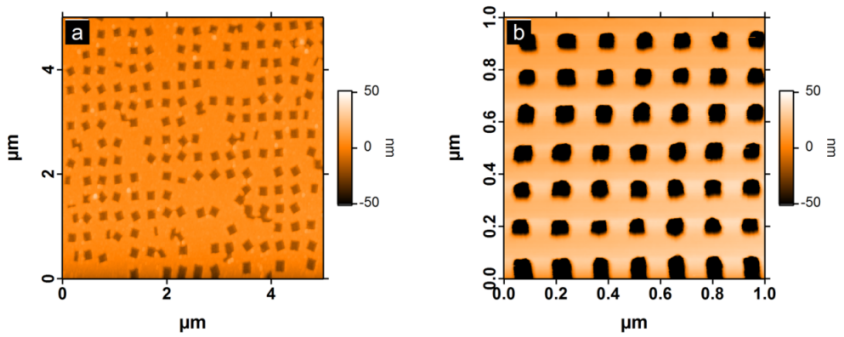

Figure 3.10: AFM topography images of mold made by EBL. (a) Using double-layer resist and (b) small feature size NIL mold fabricated using a mono-layer EBL resist. It should be noted that the scale of (b) is 1 µm x 1 µm.

Even with the shorter development time, the double-layer resists EBL process cannot be used as a reliable method to fabricate hard molds with feature sizes below 100 nm as the problem of shortcut is more significant. Thus, the mono-layer resist of PMMA is used to fabricate molds of feature sizes as small as 75 nm as shown in Figure 3.10(b). Fabrication of the square cavities of lateral size of 75 nm is achieved by particularly controlling many of the parameters that affect the EBL process like those mentioned at the beginning of this section.

To summarize this section, we have fabricated the hard molds required to make nanoimprint lithography (NIL) by electron beam lithography (EBL), metal-lift off and reactive ion etching (RIE). By means of the described processes, hard molds containing nano-features of different lateral sizes and shapes are fabricated reproducibly by optimizing the EBL process parameters. Moreover, a reliable lift-off is performed via the double-layer resist process. The AFM and SEM images confirm the fabrication of regularly patterned molds with nano-cavities.

As mentioned earlier, however, one of the drawbacks of EBL is the limited area over which the samples can be irradiated. To avoid this limitation, another lithography technique was investigated, that is known as block copolymer lithography (BCL). The possible advantage of BCL is to transfer the nanostructures created by the copolymers into a mold over much larger areas, which is difficult otherwise to achieve by EBL. The large surface area can be useful for ferroelectric characterization of the nanostructures and also to integrate these nanostructures into devices.

In the next section the fabrication of nanostructures based on the self-assembly of block copolymers and the suitability of BCL for NIL hard mold fabrication is

presented. In the first part, basic principles of block copolymers lithography process are discussed. Then, the specific experimental setups and some typical results are presented.

3.2.2 Block copolymer Lithography (BCL)

Block copolymer (BCP) based nanofabrication is an emerging approach for the fabrication of nanostructured features because of the ability of copolymers to self-assemble into morphologies having domains tens of nanometers in size [11-16]. Block copolymers are produced by covalent bond connection of two or more chemically different polymer chains [17]. Unlike most pairs of polymers, the two constituents of diblock copolymers are unable to phase separate at the macroscopic level [13]. Diblock copolymers spontaneously self-assemble into nanometer-sized domains that exhibit spontaneously ordered morphologies at equilibrium [12]. The actual size and shape of the domains in the diblock copolymers are dependent on the relative chain lengths and composition of the blocks and usually adopt various nanoscopic structures like spheres, cylinders, or lamellae [12].

Block copolymer lithography (BCL) is one of the "bottom-up" approaches that use domain structures of copolymer thin films as lithography masks to transfer a periodic array of patterns into substrates. It has been reported that by removing the minor component of microdomains a nanoporous template can be produced, however, the exact mechanism of nanopore creation is not very clear. These porous structures are further used as a mask to etch the underlying substrates. Dense arrays of nanostructures with a density of ~10^{11} holes/cm^2 [12] and also later patterned media with a density of 1 Terabit/$inch^2$ and beyond have been reported by BCL [18]. Large area high density sub-20 nm SiO_2 hard molds for

nanoimprint lithography are also produced by BCL [15]. These reported nanostructures are either difficult or expensive to fabricate using conventional lithographic techniques like photolithography or electron beam lithography.

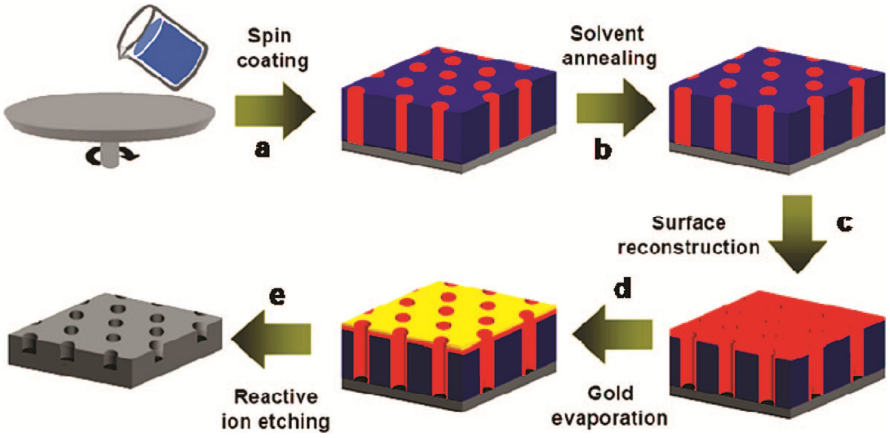

Figure 3.11: Schematic to create nanoporous structures using block copolymer lithography: (a) spin-coating of block copolymer on a SiO_2 substrate; (b) preparation of highly long-range ordered films via solvent annealing; (c) surface reconstruction of ordered films; (d) metal evaporation on the reconstructed films; and finally (e) transfer of nanoporous patterns by the use of reactive ion etching of the substrate [14]

A schematic representation of the block copolymer lithography is presented in Figure 3.11. It shows the whole fabrication process starting from the deposition of the copolymer solution by spin-coating to the ultimate transfer of nanopatterns to the substrates by reactive ion etching (RIE) process [14]. Among the different thin film morphologies of copolymers, cylindrical domains with their domains oriented perpendicular to the substrate are of interest for our project. Therefore, all the explanations and discussions hereafter are made for

cylindrical morphologies only. One of the main benefits of using cylindrical morphologies to fabricate molds for NIL is because of their high aspect ratio and vertical orientation which can be turned to some extent by solvent annealing [19-21] or by the application of an external field [11, 17, 22, 23]. In addition, by selecting the right materials and the right experimental setup the desired microdomains (cylindrical) can also be obtained by just spin-coating thin films of copolymers [14]. It is also highly desirable that the process selected be independent on the underlying substrate; otherwise, additional steps need to be done to ensure the vertical orientation of domains.

3.2.2.1 Experimental Setup and Materials Used

Recently, it has been reported that highly oriented cylindrical microdomains with a long-range lateral ordering can be achieved by simply spin-coating a poly(styrene-b-4-vinylpyridine) (PS-b-P4VP) diblock copolymer solution [14, 20, 21]. In this thesis PS-b-P4VP copolymers were used as well. The selection of these copolymers is logical to achieve cylindrical microdomains that are oriented normal to the surface because they are attractive for NIL template applications. The other major advantage of using these copolymers is that these cylindrical orientations are obtained after spin-coating regardless of the underlying substrate. This is quite interesting for lithography applications since the ultimate goal of using these copolymers is to transfer the pattern templates to the substrates.

PS-b-P4VP copolymer solutions were prepared from a mixed solvent of toluene and tetrahydrofuran (THF). The ratio of toluene/THF was 75/25; V/V. PS-b-P4VP thin films were fabricated by spin-coating at different spinning speeds on a silicon dioxide substrate. In order to get a higher degree of lateral order, the as

spin-coated thin films were annealed in a solvent vapor [20]. Solvent annealing involves the use of a good solvent vapor or of mixtures of solvent vapors to treat spin-coated films in the gas phase. One of the reasons for an improved ordering of the microdomains by solvent annealing is attributed to the substantially increased mobility of the plasticized BCP during the annealing process [11, 20]. The solvent vapor exposure time can be varied from a few hours to several tens of hours, depending on the final ordering sought. The experimental setup for solvent annealing was quite classical. A mixture of 2.5 ml of THF and 7.5 ml of toluene in a 50 ml beaker was used as a solvent. The spin-coated sample and the solvent were kept under a half-cut 2 liter beaker for 6 hours.

By dipping these ordered films into a preferential solvent for P4VP, which is ethanol in this work, a nanoporous film can be produced by swelling only the P4VP block as demonstrated in [14, 20, 21], though as stated earlier the details are not very clear. These created pores are then used to etch the underlying substrate. Using the aforementioned experimental setups and conditions, we carried out the lithography processes presented below.

3.2.2.2 Results and Discussion

Initially a low molar mass PS-b-P4VP was used, with number average molar masses of PS and P4VP blocks of 51 and 18 kDa Kg/mol, respectively, and a total polydispersity of 1.15. PS-b-P4VP thin films were prepared by spin coating typically at 2000 rpm and 60 s from a 0.5 wt % toluene/THF solution on the silicon oxide substrate.

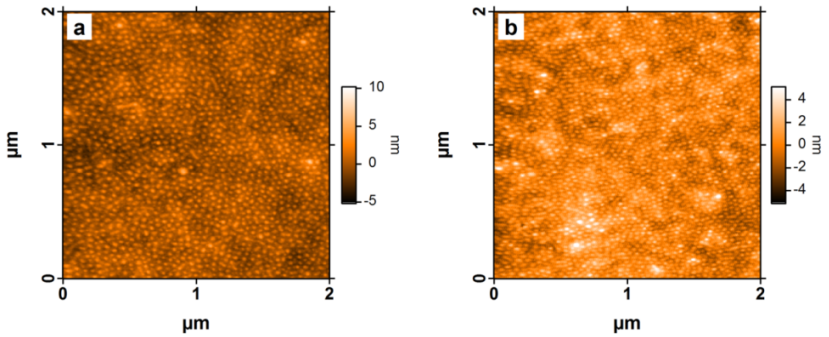

Figure 3.12: AFM height images of highly ordered PS-b-P4VP films on silicon oxide substrates: (a) topography image of spin-coated copolymer thin film, and (b) structure after solvent annealing.

The atomic force microscopy (AFM) topography image of Figure 3.12 (a) shows as spin-coated PS-b-P4VP thin film whereas the topography image of the solvent-annealed thin film on a native silicon oxide substrate is shown in Figure 3.12 (b). In fact, the two images look similar in that both images display circular domains over their surface. As it can be seen from both images, all the circles are not uniform in size and are not regular in arrangement as well. From SEM images (shown in Appendix, Figure A4), the diameter of one random circle is ~18 nm and the separation distance between two circles is ~39 nm. However, the existence of circular domains testifies that the cylindrical microdomains of the P4VP are oriented normal to the surface.

When, the spin-coated films were subsequently exposed to a toluene/THF mixtures at room temperature for 6 h, the lateral ordering of the circular holes looks slightly enhanced (Figure 3.12(b)), though this is not that much obvious. Still the ordering obtained here is not as good as what has been reported in the literature [14, 20, 21].

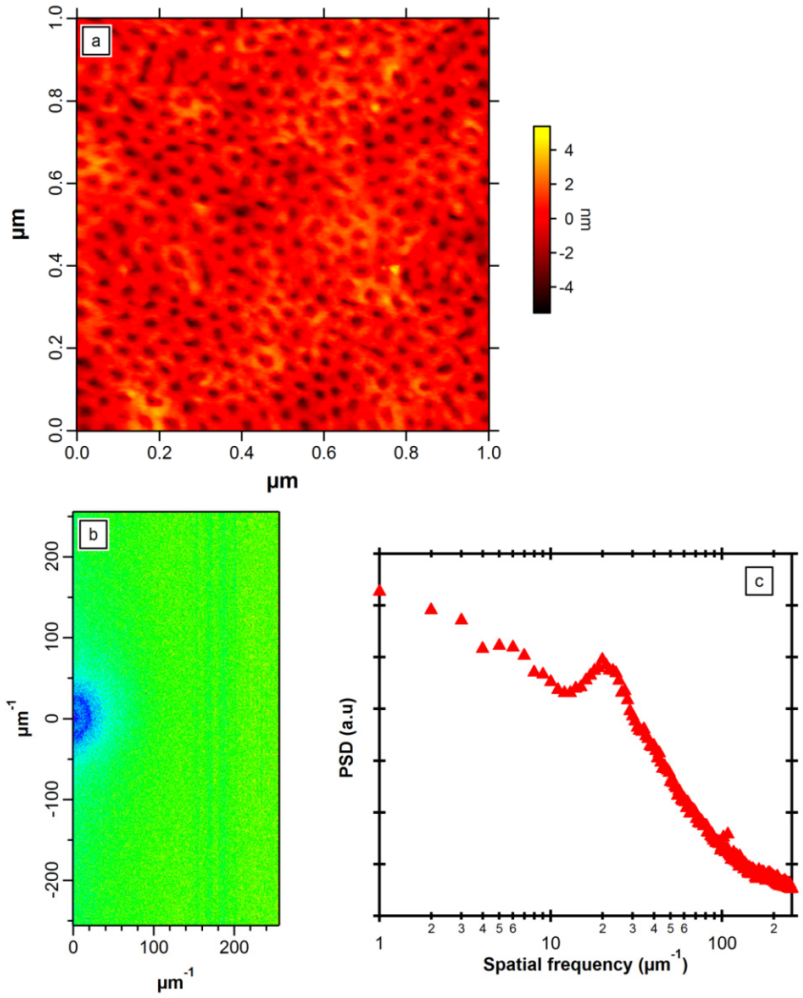

Figure 3.13: (a) AFM topography images of ordered PS-b-P4VP films after surface reconstruction by ethanol on silicon oxide substrate. (b) Two-dimensional PSD computed from the AFM topography image of (a), and (c) circular average of (b).

To be more quantitative about the distribution of holes and the average distance between the holes the power spectral density (PSD) of an AFM topography image of PS-b-P4VP films after surface reconstruction is presented in Figure 3.13 (a and b). The PSD is obtained from the squared norm of the Fourier transform of two-dimensional brightness function that defines the image, and it is often used for pattern recognition [24]. The two-dimensional PSD of the reconstructed sample (Figure 3.13 (b)) shows that the distribution of the nanopores is isotropic, whereas from the radial average of Figure 3.13 (b) the average distance between the holes is found to be ca. 50 nm.

Finally, the solvent annealed films were dipped in ethanol for 30 min. Since ethanol is a selective solvent for P4VP and a non-solvent for PS, a reconstruction of the film is observed with the formation of an ordered array of nanoscopic pores (Figure 3.13). In other words, when the P4VP block is solubilized by ethanol and subsequently dried, the P4VP rests on top of the PS matrix, leaving pores at the positions of the cylindrical P4VP microdomains. The surface-reconstructed film retained the ordered microdomain structure of solvent-annealed films (Figure 3.12(b)) without changing the domain size and diameter.

In order to check if the holes go down to the bottom, a thin layer of chromium (15 nm) was evaporated onto the surface of the reconstructed film by orienting the film surface perpendicular to the path of the chromium atoms from the target in the evaporator. The thickness of the metal was set in order to fill one fourth of the pores depth. However, lifting off the film after the Cr deposition proved to be very difficult, probably due to the relatively small pore size and larger Cr grain sizes.

To fabricate nanoporous templates of larger pore sizes, larger molar masses of PS-b-P4VP copolymers were used. This is because the resulting pore size of the templates can be simply tuned by varying the molar mass of the block copolymers [11]. Thus, the same set of experiments were performed with PS-b-P4VP BCPs having a molar masses of the PS and P4VP blocks 93 and 35 Kg/mol, respectively, with Mw/Mn =1.15 (purchased from Polymer Source). Since the molar masses are larger, larger diameter sizes are expected. Figure 3.14(a) shows an AFM image of the PS-b-P4VP template after spin-coating and solvent annealing with a toluene/THF mixture, followed by swelling with alcohol and drying.

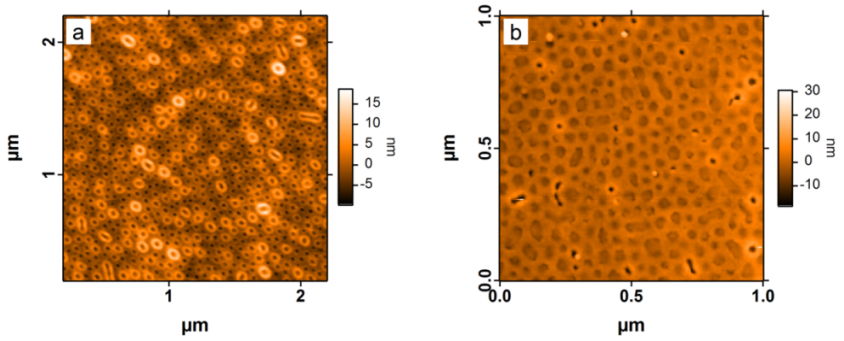

Figure 3.14: AFM topography image of surface reconstructed film of PS-b-P4VP film with a BCP of larger molar mass. (a) Pore opening by dipping for 30 min in ethanol; and (b) the same molar mass after 1 hour immersion in ethanol.

The PS-b-P4VP copolymer film with the larger molar mass was also dipped in ethanol for a longer time (1 hour), and the topography image of this sample is shown in Figure 3.14(b). We can see that the pore size of this sample is wider even if the ordering is less than the previous one. The cross section of a single hole from Figure 3.14(a) is shown in Figure 3.15. The diameter of the hole is

found to be approximately 47 nm which is indeed larger than the previous set of samples.

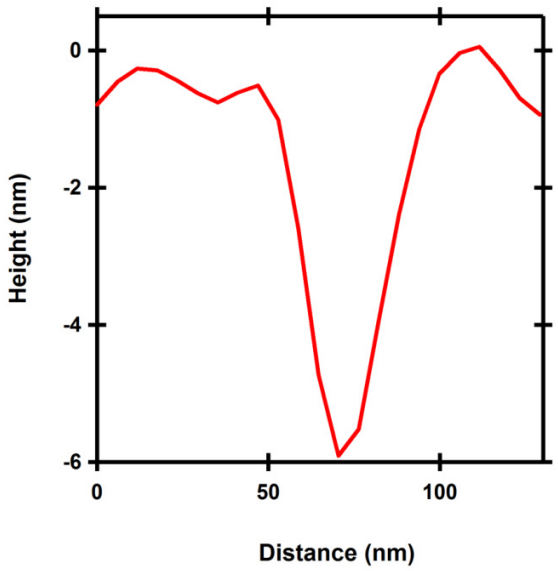

Figure 3.15: Profile image of a single hole of nanoporous template made from the PS-b-P4VP copolymers shown in Figure 2.14.

It should be noted that the value of height from Figure 3.15 does not give the exact depth of the pores since the AFM tip does not reach the bottom of these small pores. 5 nm of Cr was then evaporated on the surface of the film to use the Cr as a mask to etch the silicon oxide. However, a neat lift-off was still difficult to achieve. Thus, we were not able to produce hard molds from PS-b-P4VP copolymers.

A series of experiments were carried out involving variation of molar mass, thickness, annealing time, concentration of PS-b-P4VP, and ratio of

toluene/THF. The obtained results were different from what has been reported in the literature [11-15, 18, 23]. This could be because block copolymer lithography is a very sensitive experiment where a slight change in any of the above parameters could change the final result significantly. The resulting microstructures were invariably of lower quality than expected; therefore, we stopped working on BCL to focus on the EBL technique.

3.3 Nanoimprint Lithography (NIL)

Nanoimprint lithography, sometimes described as “hot embossing”, is a parallel method to transfer topographic patterns from a rigid mold into a heated thermoplastic or thermosetting polymer film under pressure [25]. Nanoimprint lithography has gained a significant attention recently as a simple and cost-effective technique to replicate patterns of a hard mold with high precision. The advantages of NIL over the conventional “top-down” lithography techniques like photolithography and electron beam lithography include low-cost fabrication, high resolution, and high throughput production of nanostructures [25-31]. In addition, conventional lithography techniques expose substrates to corrosive etchants and high-energy radiations during the transfer of patterns from the resist to the substrate. This can be considered as a drawback for some specific applications like when using sensitive organic materials, which is specially the case for ferroelectric polymers.

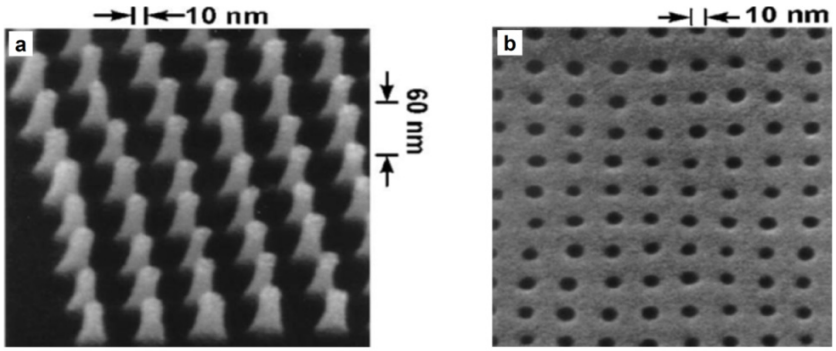

Figure 3.16: (a) Scanning electron microscopy (SEM) image of a fabricated pillar mold of 10 nm diameter and (b) SEM image of 10 nm wide imprinted arrays of holes in PMMA resist using the mold shown in (a) [32].

Nanoimprint lithography creates a pattern by physical deformation of the resist with embossing, unlike optical lithography and EBL where the chemical structure of the resist is modified with radiation [33]. This striking difference in the operating principle leads to one of the great advantages of NIL, i.e., its ultrahigh resolution. Features as small as ~ 10-nm over a large surface area reported on poly(methyl methacrylate) (PMMA) by the NIL technologies as shown in Figure 3.16 [32].

The advantages of NIL are not limited to the production of patterns in a polymer resist, NIL can also shape and improve the functional properties of polymer materials while imprinting. Thus, NIL can be used to create functional polymer devices directly. Here, it should be emphasized that the mechanical confinement of polymers by NIL is more desired than the simple shape patterning that can be achieved by other lithography techniques such as EBL. For example, our group and others have reported on the use of nanoimprint lithography to control the

crystal orientation in soft nanostructures, so that highly ordered ferroelectric polymer arrays were achieved that can be used for non-volatile low-voltage memories [34-36]. NIL was also used to fabricate nanowire-based devices consisting of liquid crystalline light-emitting polymers and of liquid crystalline semiconducting polymers, proving the versatility and wide applicability of the method [37, 38].

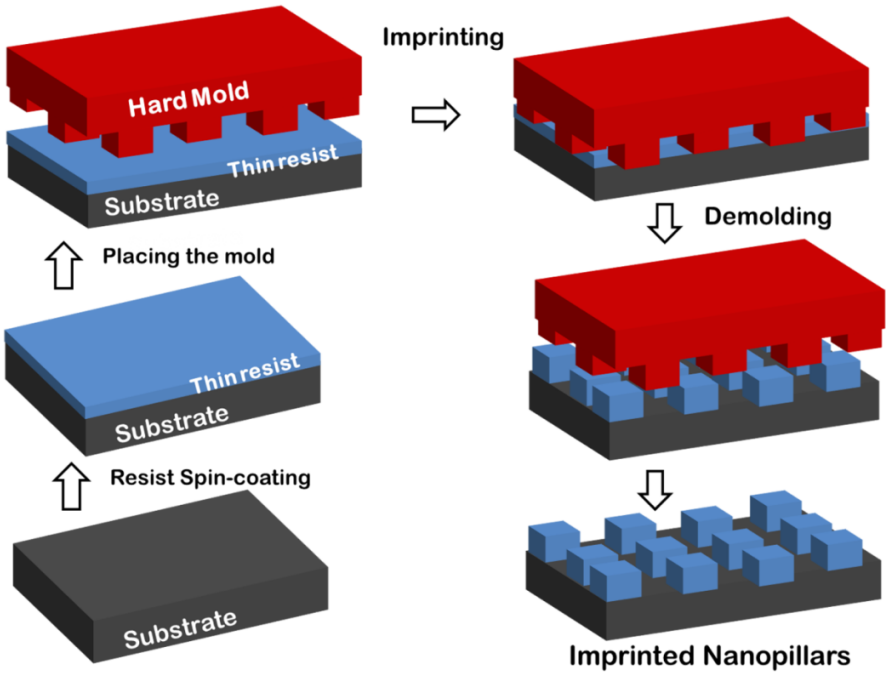

Figure 3.17: Schematic description of imprinting and pattern transfer using a hard mold to create nano-pillars into a polymer resist by nanoimprint lithography. It shows the whole NIL process starting from uniform thin film on a bare silicon substrate to the final imprinted patterns.

The general working principle of NIL is shown in Figure 3.17. First, a thin resist is spin-coated on a substrate. When the heated resist is pressed by a mold with nanoscale protrusion features on its surface, the resist material underneath the protrusions is displaced and transported to the nearby trenches or cavities [39]. Once the resist is solidified by cooling at a lower temperature, the hard mold is removed. At the end of the process, the features of protruding mold have been transferred to the soft polymer resist.

The NIL molds should be compatible with the fabrication process and are commonly made of solid materials like silicon, silicon dioxide or silicon nitride, with a high strength and durability. The hard mold used in NIL can be prepared by other lithography techniques. The common fabrication techniques of NIL molds include optical lithography for microscale features, EBL for very small features, or NIL itself as discussed earlier. To preserve the structural integrity during the removal of the mold, the mold itself needs to be coated with a self-assembled anti-adhesion layer to prevent sticking of the mold and the resist.

To replicate the features of the hard mold nanoimprint lithography requires the use of easily deformable polymers under an applied pressure. As an example, thermoplastic amorphous polymers like PMMA and polystyrene (PS) or some other functional organic polymers can be used as imprinting resists. For thermoplastic polymers, imprinting must be done at a temperature above the glass transition temperature (T_g) so as to lower the viscosity of the polymer, allowing easy flow of mass to the nearby cavities.

Like other lithography techniques, nanoimprint lithography is not immune from drawbacks. One of the main limitations is the lifetime of the mold because after some number of imprints the hard mold may require replacement. The other

challenge facing NIL is the thermal cycling of the system. Since NIL is a process in which the resist should be heated to a certain temperature for embossing and cooled afterwards to detach the mold, the imprinting throughput is limited by this cycling process [5, 26, 31].

3.3.1 Fabrication of arrays of P(VDF-TrFE) by NIL

As explained in the introduction section, NIL is a fast and low-cost lithographic technique which allows us to replicate not only nanopatterns but also to fully control the crystal orientation of polymers. In this section, an in-depth description of the fabrication steps of these ferroelectric arrays of nanostructures in our laboratory is presented.

Here, an Obducat Nanoimprinter is used to fabricate high-density arrays of ferroelectric polymer cells (Figure 3.18). The ferroelectric material that we want to pattern here is the semicrystalline poly(vinylidene fluoride-ran-trifluoroethylene) P(VDF-TrFE) copolymer.

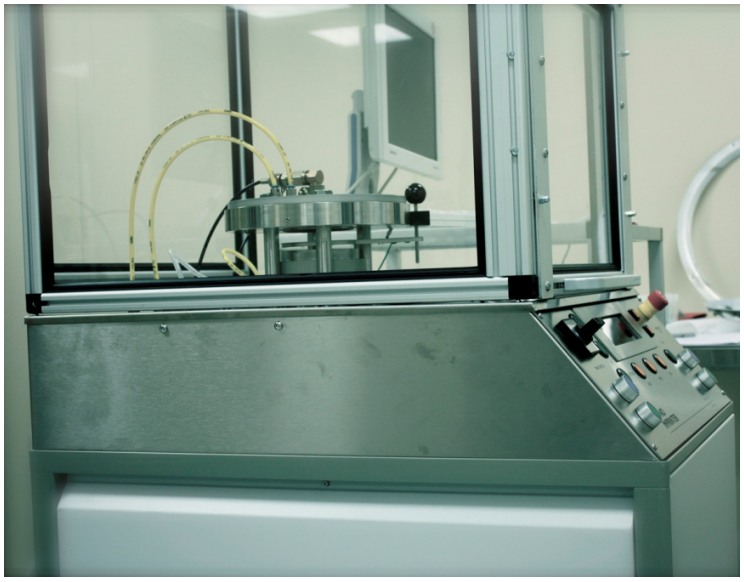

Figure 3.18: Image of the Obducat Nanoimprinter machine.

To create a clear picture of the nanostructure fabrication process, the experimental processes of one typical NIL is detailed below. The process is supported by some schematics and pictures when necessary. The first step of a NIL experiment is using a commercially available n-doped (P-doped) silicon wafer of thickness around 380 µm. The doped silicon substrate which is polished on one side is chosen because of its conductivity for future ferroelectric characterization of imprinted structures. The full Si wafer is diced into small pieces of 1.5 cm x 1.5 cm. The silicon substrates are cleaned by treatment in a piranha solution which is a mixture of H_2O_2 and H_2SO_4 (1:1 v/v) for about 30 min and then thoroughly washed with pure Milli-Q water.

P(VDFE-TrFE) powders produced by Solvay Solexis, France are used as received. The P(VDF-TrFE) powder is dissolved in cyclohexanone to prepare a solution of defined concentration. A continuous thin film of P(VDF-TrFE) is

prepared by spin-coating on the silicon substrate. By pouring and spinning a small amount of polymer on the substrate at a given rotational speed and time, a uniform continuous thin film can be achieved. The film thickness is varied by changing the spinning speed. The thicknesses are measured by ellipsometry and profilometry.

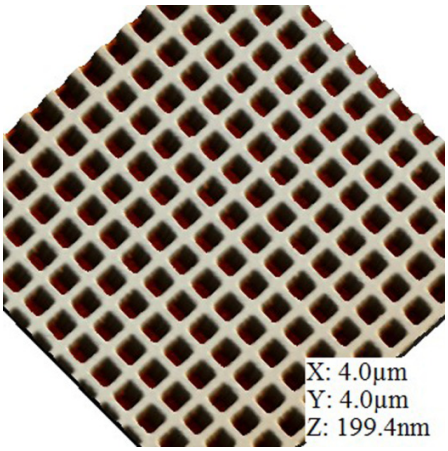

Figure 3.19: Three dimensional AFM image of a typical hard mold with square cavities used to create pillar nanopatterns onto organic resists by NIL.

Silicon oxide molds with arrays of cavities of different size and shape made by EBL and etching are used to carry out NIL. Figure 3.19 shows an atomic force microscopy (AFM) image of a typical imprinting mold used in this thesis. The details of the mold fabrication technique were presented in the preceding section. To decrease the sticking of the mold with the P(VDF-TrFE) copolymer, the hard mold itself needs to be coated with some non-adhesive layer. Here, a monolayer of perfluorodecylchlorodimethylsilane was deposited by mixing a few drop of the silane in a toluene solution (around 0.1 % in volume). The salinization is performed in a glove box with low H_2O content (less than 0.1

ppm). To clean the mold after a couple of NIL experiments, it was rinsed first in acetone and then in cyclohexanone solution to remove P(VDF-TrFE) polymer remaining in the cavities of the mold. In addition, oxygen plasma was used subsequently to make sure that impurities and contaminants on the hard mold are removed. Finally, prior to the salinization step the hard molds were further cleaned by treatment in a piranha solution which is a mixture of H_2O_2 and H_2SO_4 (1:1 v/v) for about 1 hour and then thoroughly washed with pure Milli-Q water. The hard molds have to be silanized repeatedly after a few NIL experiments to achieve good quality of imprinted patterns. The sticking problem is more frequent in our experiments because the molds have a high density of nanoscale protrusion features on their surface leading to strong adhesion between the mold and the copolymer.

Once the continuous thin film of P(VDF-TrFE) is prepared, the silanized hard mold is placed on top of the polymer film. Figure 3.20 shows the schematics of a time diagram of the temperature and pressure during the nanoimprinting process. Before applying pressure, the thin film is heated to 125°C. Then, the printing mold is pressed against the film under pressure of 60 bar at a temperature of 125°C and held for 10 min to make sure that the nano-cavities in the printing mold are completely filled (Figure 3.20). Finally, the system is cooled to 60°C, the pressure is reduced to zero, and then the mold is removed.

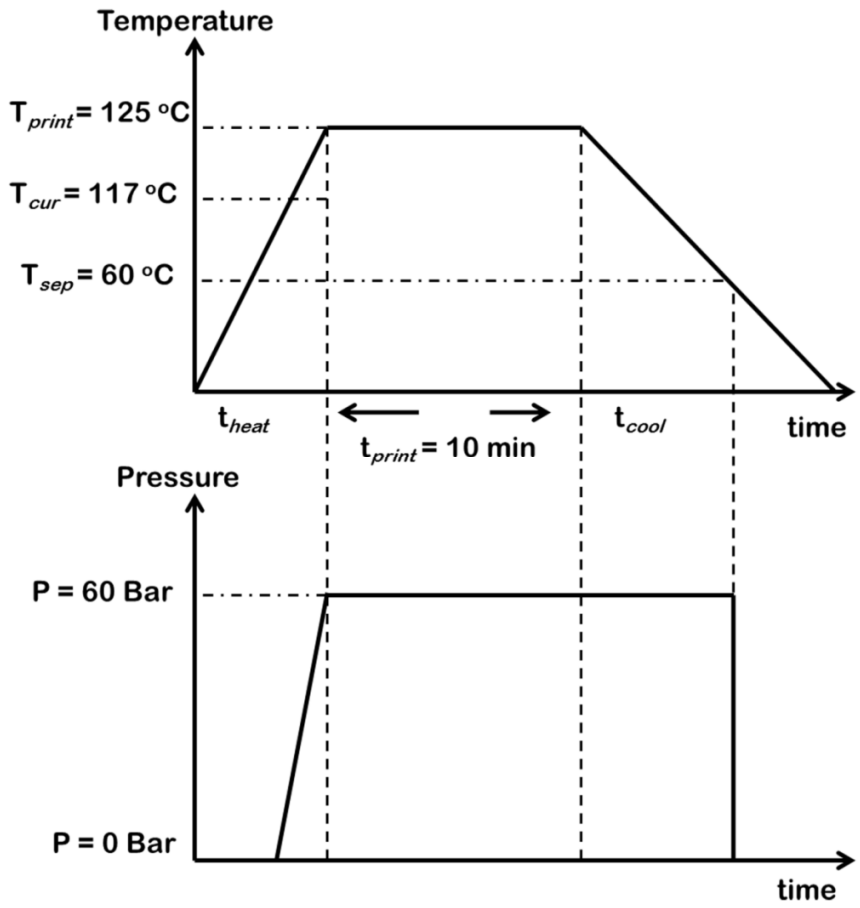

Figure 3.20: Schematics of the whole imprinting process sequence displaying the applied pressure and temperature versus time.

The imprinting temperature is chosen in such a way that it is positioned between the Curie and the melting temperature. In this specific process, 125°C is selected for a P(VDF-TrFE) copolymer 70% in VDF, which has a Curie temperature of 117°C and a melting temperature of 143°C. Heating the polymer above the

Curie temperature enables the polymer chains to flow and fill the mold cavities during imprinting. The values of imprinting temperature were obtained from DSC experiments, and are presented in the second chapter of this thesis.

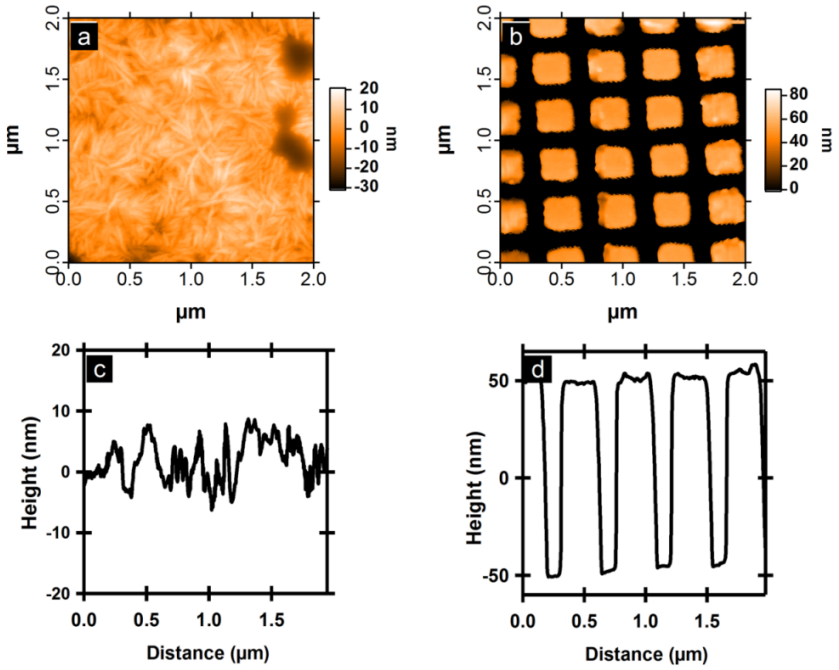

Figure 3.21: (a) AFM topography image of continuous P(VDF-TrFE) thin film, (b) AFM image of nano-imprinted P(VDF-TrFE) structures, (c) cross sectional profile image of (a), and (d) cross sectional profile image of (b).

As an example, we present AFM topography images of a continuous thin film of P(VDF-TrFE) (Figure 3.21(a)) and of a subsequently imprinted arrays of pillars (Figure 3.21(b)) using hard molds of square nanofeatures like the one shown in Figure 3.19. The profile images are also presented in Figure 3.21(c & d) respectively showing the thickness contrast before and after the embossing

process. The almost flat continuous thin film of Figure 3.21(c) with less than 10 nm peak to peak roughness is transformed into an ordered array of pillars of 100 nm height.

The size of the pillars in Figure 3.21 is 250 nm x 250 nm; however, bigger square pillars with lateral size of 500 nm x 500 nm and smaller pillars of lateral size 75 nm x 75 nm were also fabricated using this technique. Imprinted patterns of different sizes are presented and discussed in the subsequent chapters. Nevertheless, using NIL, not only the lateral size of the patterns, but also the shape of the imprinted patterns can vary as well depending on the shape of the cavities of the hard mold. Figure 3.22 is another example of imprinted P(VDF-TrFE) line patterns embossed using the same conditions as those of the pillar patterns of Figure 3.21. Figure 3.22(a) is an AFM image of the line mold while the imprinted line patterns are shown in Figure 3.21(b).

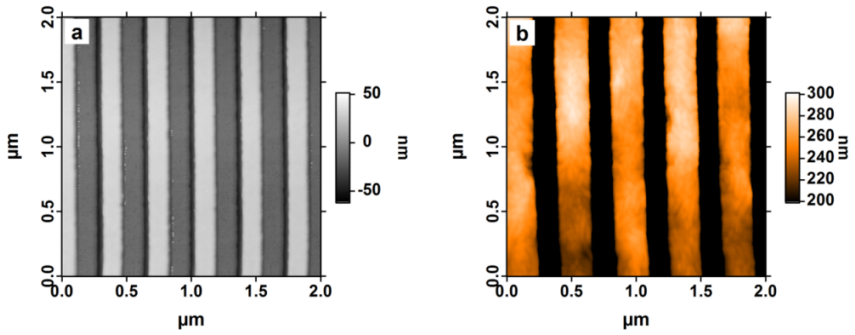

Figure 3.22: (a) AFM height image of hard mold bearing line nano-features and (b) is an AFM topography image of the replicated pattern (lines) by the hard mold of (a).

The other important outcome of NIL is the amount of excess polymer left between the protrusions of the mold and the substrate (referred to as residual layer hereafter). The presence or not of the residual layer can be intentional or not. For example, in order to prevent the damage of surface-relief features of the hard mold, a thin film of residual layer can be left intentionally [26]. Then, to uncover the surface of the underlying substrate an anisotropic O_2 plasma etching is often used [28].

For some applications, however, the presence of a thin residual layer may not be needed. The chain orientation, subsequently, the electrical properties of semicrystalline polymers can be influenced by the presence of a residual layer [34, 37]. The thickness of the residual layer depends on the master mold characteristics, the initial thickness of the resist, or the embossing parameters. Here, we present how the thickness of the residual film thickness can be precisely controlled by deriving a simple formula for square cavities of a mold with lateral sizes s_1, s_2 and depth h, when the mold is pressed to its maximal penetration depth in the film (filled cavities) (Figure 3.23). Let us call the initial thickness of the spin-coated film t_o, and t the residual film thickness after the embossing.

From the law of conservation of mass, after embossing the mass of the polymer film should be the same as the initial total mass before embossing. This means that the initial mass should be equivalent to the sum of the mass in the cavities of the mold plus the mass of the recess between the substrate and the protrusions of the mold.

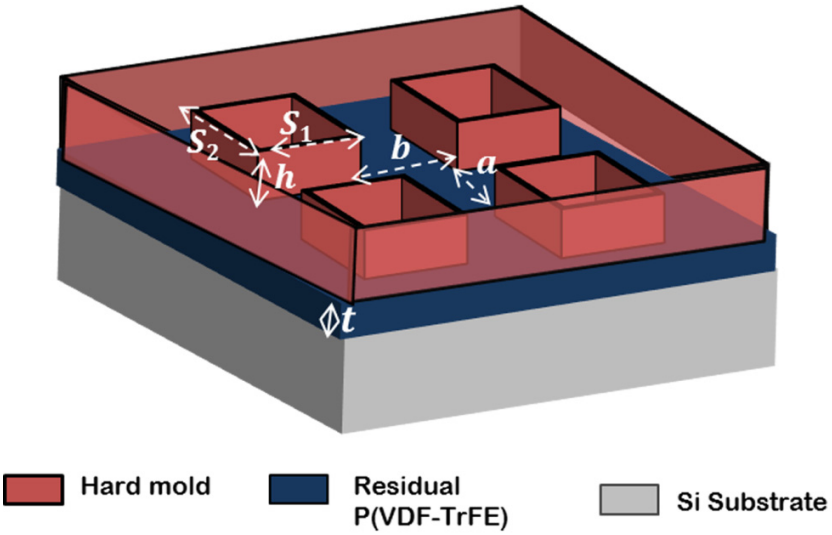

Figure 3.23: Schematic description of the embossing process. The top (light blue color) is the hard mold with dimensions indicated; the red layer is the remaining polymer film after the NIL process, whereas the grey layer is representing the silicon substrate.

Using the parameters depicted in Figure 3.23 we can write mathematically,

$$(s_1 + b).(s_2 + a).t_0 = (s_1.s_2.h) + [(s_1 + b).(s_2 + a).t\,] \ldots\ldots\ldots \quad (3.1)$$

if the initial thickness t_o is large enough to have a non-zero thickness t for the residual layer.

From equation (2.1), the value of the final residual film can be expressed as

$$t = \left(t_0 - \frac{(s_1 . s_2)}{(s_1 + b).(s_2 + a)} . h \right) \ldots\ldots\ldots\ldots . (3.2)$$

The abbreviations of the parameters are as follow:

t = the residual film thickness
t_0 = the initial thickness of the spincoated film
h = the depth of the square cavities of the mold
s_1 = the length of one side of the square cavity of the mold
s_2 = the length of the other side of the square caities of the mold
a = the spacing between the adjacent square cavities
b = the spacing between the adjacent square cavities on the other side

Since the dimensions of the imprinting mold are fixed, and the initial film thickness of the P(VDF-TrFE) can be calibrated, it is possible to select a specific value for the final residual thickness. To control the thickness of the initial continuous thin film in this thesis the solution concentration and spinning speed were adjusted depending on either a partial or full confinement regime was sought. The full confinement regime corresponds to a zero residual film thickness, for which we need as starting t_o :

$$t_0 \leq \left(\frac{(s_1 \,.\, s_2)}{(s_1 + b).(s_2 + a)} . h \right) \ldots\ldots\ldots\ldots\ldots\ldots (3.3)$$

In this regime, the absence of residual layer film connecting the pillars left after imprinting ensures that each pattern evolves independently on its neighbours, with the polymer being effectively confined three-dimensionally. The AFM images of the pillar and line patterns shown in Figures 3.21 and 3.22 are examples of imprinted samples with almost no polymer left after the embossing process.

3.4 Structural Characterization Techniques

The microstructure and topography view of nanoimprinted regular arrays, continuous thin films of P(VDF-TrFE) copolymers, and nanostructured imprinting molds can be inspected by a range of characterization techniques. In this section a brief overview of the main structural characterization techniques are presented.

3.4.1 Atomic Force Microscopy (AFM)

Since its first introduction by Binning and Quate, atomic force microscopy (AFM) has revolutionized the way researchers probe nanostructured surfaces [40]. AFM makes it possible to observe, manipulate and explore surface at the molecular level. In addition to topographic images, AFM enables a nanoscale understanding of how systems work, thus, leading to new discoveries in many fields.

The AFM system unlike the traditional microscopies does not rely on far field electromagnetic radiation to create an image. AFM senses small forces that act on the surface of a sample by sharp tips (here, it uses the near field electromagnetic fields) [40]. To generate a topography image, the tip is attached to the free end of a cantilever that bends under force while the tip is moved in three dimensions using a piezoelectric scanner (Figure 3.24). During the sample surface scanning, the cantilever bending is detected by means of a laser beam focused on the backside of the cantilever, which is ultimately reflected onto a photodiode. In this way three dimensional images are obtained at high resolution.

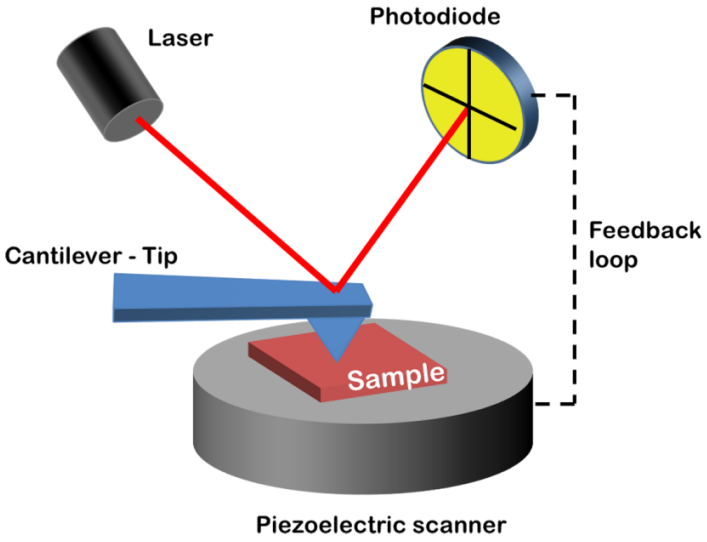

Figure 3.24: Schematic description of the working principle of an AFM. In the AFM system, a sharp probe scans across a surface. By monitoring the motion of the probe, a three dimensional image of a surface is reconstructed.

AFM has two modes of operation that are commonly used to acquire images, known as contact and tapping mode. In the contact mode, the tip makes physical contact with the sample and the resulting image is a topographical map of the surface of the sample. The force acting on the tip is proportional to the deflection of the cantilever. Thus, by keeping this force constant (fixed cantilever deflection) the motion of the scanner in the z-direction can be recorded. Nevertheless, this mode can cause damage to both sample and probe (create artifacts).

Another well-known imaging mode of AFM is tapping mode. In this mode the cantilever oscillates close to its resonance frequency. While scanning, the force

between the sample and tip, hence, the resonance frequency and phase of the cantilever, are altered. By using an electronic feedback loop this amplitude variation is recorded as a height image. In addition, the phase shift can be used to reconstruct a phase image. In our work, the tapping mode is implemented to characterize microstructure and topography images of different samples.

3.4.2 Scanning Electron Microscopy (SEM)

A scanning electron microscope is a scientific instrument that enables the observation of samples down to a few tens of nanometers [41]. The working principle of SEM is like a laser scanning optical microscope. However, SEM uses a finely focused electron beam instead of light to image the sample. The structure of the instrument is shown in Figure 3.25. It consists of an electron source, scan coils and condenser lens that deflect and focus the beam. The focused beam is used to scan the surface of the sample [42]. Finely focused electron beams result in higher resolution.

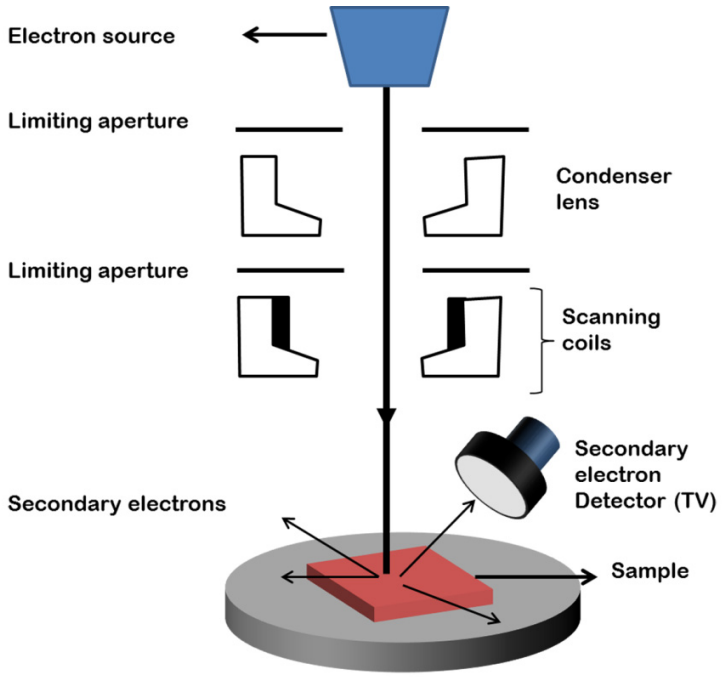

Figure 3.25: Schematic diagram of a scanning electron microscope (SEM).

When the electron beam irradiates the sample surface, electrons are emitted from the surface. By collecting these electrons through detectors, an image is produced on the cathode ray tube (screen). For imaging a relatively low (1 to 2 kV) voltage is sufficient. Note that the voltage used for EBL is 30 kV. In this thesis, the SEM technique is used to image the patterns of imprinting molds.

3.4.3 Fourier Transform Infrared Microscopy (FTIR)

A widely used technique to determine molecular orientation is Fourier transform infrared microscopy (FTIR). Infrared spectroscopy is a technique based on the vibrations of the atoms of a molecule [43]. When an incident infrared passes

through the sample some fraction of the incident radiation is absorbed at a particular energy. The absorption peaks form what is commonly referred as infrared spectrum. This infrared spectrum can be considered as a molecular fingerprint of the sample because the absorption peaks correspond to the frequency of vibration between the bonds of a molecule. Thus, the knowledge of molecular vibrations of molecules is crucial to interpret their respective infrared spectrum. Figure 3.26 shows a diagram of an optical device used to perform FTIR based on a Michelson interferometer.

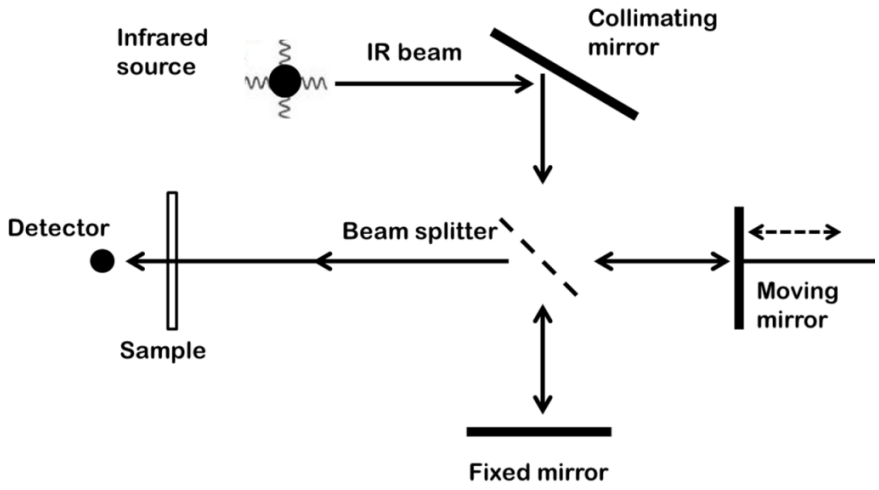

Figure 3.26: Optical diagram of a typical FTIR [44]. It consists of an infrared source, fixed and moving mirrors, beamsplitter and detector.

Using the interferometer, IR radiation is split into two beams; one of the beams travels a different optical distance so that interference fringes are created at the beamsplitter. The combined beams leave the interferometer to interact with the sample and strike the detector. In our case, the spectrometer is mounted on an

infrared microscope, providing the possibility to focus the beam onto a 100 µm x 100 µm surface area.

The absorbance peak (A) depends strongly on the angle (θ) between the transition dipole moment vector $(\bar{\boldsymbol{M}})$ and the electric field vector $(\bar{\boldsymbol{E}})$ component of the incident electromagnetic radiation (IR) [45]. Mathematically,

$$A \cong [\,|\bar{\boldsymbol{E}}| \cdot |\bar{\boldsymbol{M}}| \cdot \cos\theta]^2 \ldots\ldots\ldots\ldots\ldots\ldots (3.4)$$

Thus, for a molecule to show an infrared absorption peak it must possess a specific feature, i.e., the transition electric dipole moment of the molecule must vibrate in the same direction (parallel) with the electric field component of the incident electromagnetic wave (IR) as shown in Figure 3.27 [43-45]. On the other hand, if the electric field vector and the transition dipole moment vector are perpendicular ($\theta = 90^o$), no IR absorption is observed (Figure 3.27).

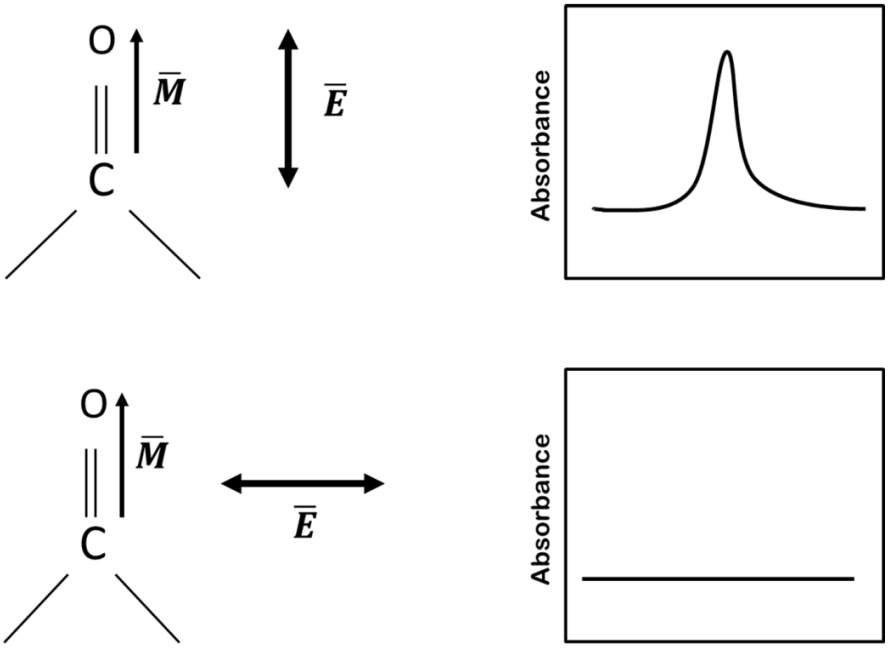

Figure 3.27: Schematic description of an infrared absorption curves as a result of a difference in the electric field polarization ($\bar{E}$) direction with respect to the transition moment vector ($\bar{M}$) [45]. The origin of absorption peak in this particular example is the presence of electronegativity difference between the carbon and oxygen atoms in the carbonyl group (C=O stretching vibration). The transition moment vector is then oriented in the direction of the net change of the dipole moment.

As already noted, for a vibration to give rise to the absorption of infrared radiation, it must cause a change in the transition dipole moment of the molecule. Vibrations in a given molecule can involve either a change in bond length (stretching) or bond angle (bending). In addition, some bonds can stretch in-phase (symmetrical stretching) or out-of-phase (asymmetric stretching) [43].

Due to the symmetry reasons, a given molecule can have only a limited number of vibration modes. As a result, the corresponding IR absorption peaks are limited in number to the possible vibrational modes of the sample. Thus, understanding of the molecular symmetry of the sample is also very important to assign infrared bands.

3.5 Characterization of Ferroelectric Polymers

In this section, the characterization technique that is used to measure the local ferroelectric properties of continuous thin films and imprinted nanostructures is presented. Investigation of the ferroelectric properties of materials necessitates a complete understanding of polarization reversal and domain structure on the nanometer scale. Recently, scanning probe microscopy (SPM) techniques have been used to study ferroelectric materials [46]. SPMs are used to create contrast due to the difference in the piezoelectric, dielectric, and structural properties of ferroelectric domains. Among the various SPM characterization techniques, the most widely used method for the nanoscale study of ferroelectric materials is piezoresponse force microscopy (PFM) [47-51]. The advantages of the PFM technique include imaging domain structures, poling of specified regions, and local hysteresis measurements. In addition, the ease of implementation on commercial AFMs and high resolution are some of the reasons for the rapidly increasing use of PFM.

Here, the PFM technique is also used to study the ferroelectric properties of nano-imprinted patterns and of continuous ultrathin films. The PFM setup was not initially existent in our laboratory. The development of this technique was therefore an important part of this thesis; this is even more so that PFM on

polymers is not frequently performed in the literature. Nevertheless, there are a few research studies on nanoscale polarization manipulation and imaging of ferroelectric copolymer films using PFM [51-55]. In this section, the basic principles of PFM are first presented. The following section describes the actual experimental requirements and settings to use the atomic force microscopy (AFM) as a PFM technique. Our experimental setup of PFM is based on the commercially available AFM technique in contact mode. Then, using the developed setup, the application of PFM for probing the local switching behavior (hysteresis loops), and the imaging modes in PFM are discussed.

3.5.1 Principles of Piezoresponse Force Microscopy

The working principle of PFM is based on the strong coupling between the polarization and the electromechanical behavior of ferroelectric and piezoelectric materials at the nanoscale [47, 49, 51]. Piezoelectricity is defined as a phenomenon where the application of pressure or stress leads to the buildup of electric surface charges or polarization. The inverse of this phenomenon is called the converse piezoelectric effect, i.e., the application of an electric field results in a deformation of the material. Piezoresponse force microscopy uses the principle of this converse piezoelectric effect. In other words, PFM measures the mechanical response of ferroelectric (piezoelectric) materials when a periodic electrical voltage is applied on the sample. Figure 3.28 shows a simplified schematic of a PFM experimental setup where ac and dc voltages are applied between the tip and the bottom electrode.

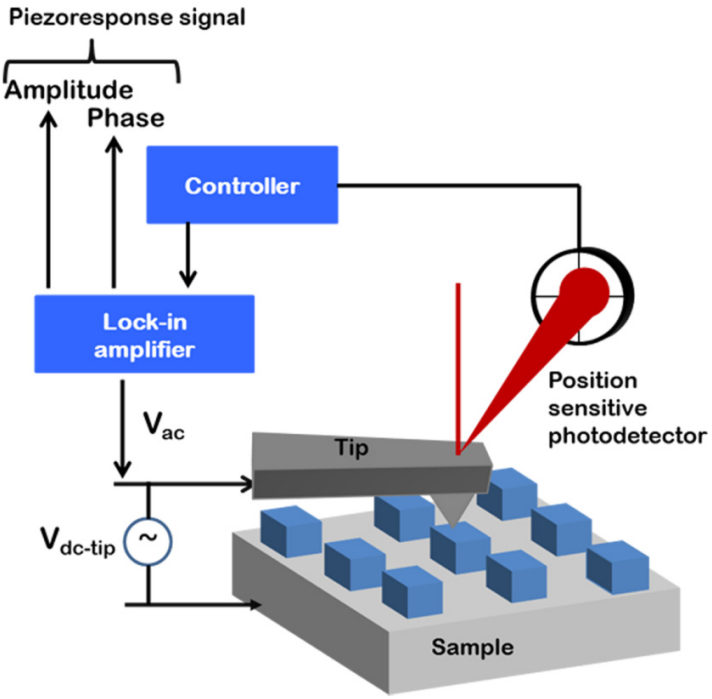

Figure 3.28: A typical piezoresponse force microscopy setup where both ac and dc voltages are applied to the AFM tip. The voltage-induced cantilever oscillation is detected by a photodetector.

A periodic bias (V_{tip}) is applied to a metal coated tip/cantilever which is in contact with the sample.

$$V_{tip} = V_{dc} + V_{ac}\cos(\omega t) \qquad (3.5)$$

Here V_{dc} is the dc bias (switching bias), V_{ac} is the ac bias (probing bias) and ω is the angular frequency of ac bias (driving frequency). When the sample expands or contracts due to the converse piezoelectric effect, the AFM tip, which is in contact with the sample, deflects simultaneously (Figure 3.28). The deflection is

monitored by means of a beam deflection laser/photodiode setup, with the first harmonic of the deflection signal detected by a lock-in amplifier (Figure 3.28). The displacement (A) is given as

$$A = A_0 + A_{1w}\, cos(\omega t + \varphi) \qquad (3.6)$$

Here A_{1w} is the sample deformation at the driving frequency of the ac voltage whereas A_0 is the static surface displacement and φ is the phase shift between the driving voltage (V_{ac}) and the voltage induced deformation, A_{1w}. It should be noted that the PFM images are recorded simultaneously with topography images.

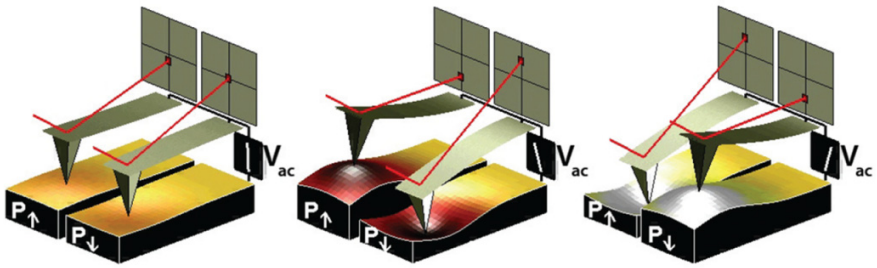

Figure 3.29: Schematics of PFM operation. (Left) when no voltage is applied, (middle and right) when voltage is applied. The sample deformation is detected by the tip deflection. The expansion or contraction of the materials is related to the local ferroelectric properties. Image courtesy S. Jesse, ORNL [56].

For example, if the initial polarization is oriented in the same direction as the applied electric field, the region beneath the tip expands due to the force made by the electric field on the surface charges (Figure 3.29). As a result the AFM tip in contact with the sample surface bends the cantilever upwards, and hence, an

increased deflection ensues (Figure 3.29). However, if the initial direction of the polarization is anti-parallel to the applied electric field, the underneath region contracts and in turn the cantilever deflection decreases. To elaborate the PFM working principle further, a simplified description of a ferroelectric sample contraction and expansion phenomenon is given in Figure 3.30.

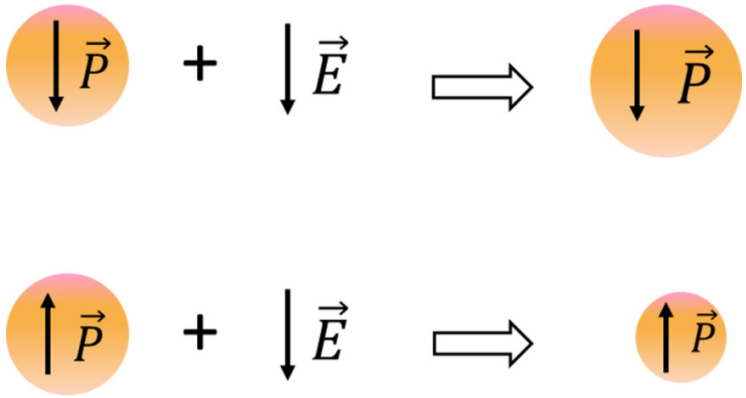

Figure 3.30: Schematic representation of a ferroelectric response underneath a polarized PFM tip. Provided that the initial polarization of the sample is downward, the sample expands when the applied electric field is in the same direction (top). On the other hand the sample contracts in the case of anti-parallel electric field application (bottom).

The PFM amplitude response of the deflection signal provides information about the local electromechanical coupling (converse piezoelectric coefficient). On the other hand, the phase φ, of the electromechanical response of the surface yields information about the polarization direction (orientation) below the tip (Figure 3.29). Domains of upward or downward-pointing polarization will have a

polarization of 0 or 180^{o}, respectively (if the voltage is applied to the tip). However, other factors can complicate this simple picture, resulting in PFM phases being neither 0 nor 180^{o}. This results from any other source of electromechanical and capacitive coupling in the tip/sample/electrode system. Besides the vertical deflections, lateral (shear) deformations of the sample resulting from any in-plane component of polarization can also be recorded to produce lateral PFM (LPFM) images [47, 49].

In addition to the simple imaging, the PFM spectroscopy technique can be used to generate local electromechanical hysteresis loops. The PFM hysteresis loops (PHLs) yield information about the local ferroelectric properties like coercive electric field and local work of switching [49]. This information is of direct interest for the realization and optimization of ferroelectric based applications such as non-volatile random-access memory (FeRAMs). To get PHLs, a small dc field is applied between the AFM tip and bottom electrode which induces local polarization orientation. A positive or negative cyclic dc bias application can orient the polarization direction upward or downward. The strength of electromechanical coupling is then measured for this dc field by recording the vibration resulting from a small superimposing field. Loops are drawn by plotting the amplitude and phase of the vibration as a function of the applied dc field. One limitation of the PHLs technique is that the PFM signals are affected by the static electrostatic contribution. To minimize this problem, techniques are reported where the PFM response is measured after the dc bias is turned off [56]. The other general challenge related with PFM is that the electric field generated by the SPM tip is highly inhomogeneous, which makes quantitative analysis of the field- induced signal extremely difficult [47].

3.5.2 PFM Experimental Setup

Our PFM system consists of an Agilent 5500 AFM (Agilent technologies) system which is adapted to perform PFM measurements. A MAC III Controller is used as both function generator for ac modulation bias and lock-in amplifier for PFM signal analysis. The lock-in amplifier of the controller converts the ac inputs to amplitude and phase.

A conducting boron-doped and amorphous diamond-coated Si cantilever (from Nanosensors) with a force constant of 0.02-0.77 N/m is used as a top electrode. To conduct PFM measurements, the n-doped silicon substrate under the polymer film is used as a bottom electrode. During PFM measurements the dc bias and the ac modulation bias can be applied to either the bottom electrode or the conductive tip. To apply higher than 10 V dc bias, an external amplifier is used. For our experimental setup, the amplified dc (> 10 V) bias is always applied on the sample (bottom electrode). The choice to apply bias either on the tip or sample is easily done by selecting the appropriate setting on the PFM control software.

3.5.3 PFM Hysteresis Loops (PHLs)

As stated above, PFM can be used in a spectroscopy mode when the measurements are done on a fixed tip position while the dc voltage is swept in a cyclic manner. The dependence of the local piezoelectric vibration on applied bias is the reason for the formation of piezoelectric hysteresis loops [48]. Measurements of local hysteresis loops are of great importance in particular for semicrystalline ferroelectrics thin films (like PVDF-TrFE) because they are able

to quantify polarization switching on a selected area of a few tens of nanometers only.

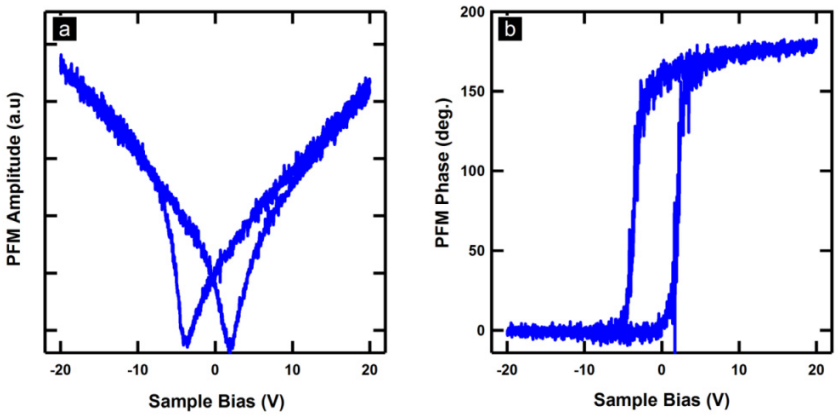

Figure 3.31: PHL amplitude (a) and phase (b) as a function of symmetric bias voltage of an annealed continuous P(VDF-TrFE) thin film.

Figure 3.31(a) shows a typical PFM "butterfly shape" amplitude and PFM phase hysteresis loop (Figure 3.31(b)) obtained using our PFM setup. These clear switching hysteresis loops indicate that the sample is ferroelectric (existence of a well-defined permanent polarization); hence, they can be used to study the polarization switching of our P(VDF-TrFE) copolymers. These hysteresis loops are recorded by applying a symmetric sweeping dc voltage from -20 V to +20 V.

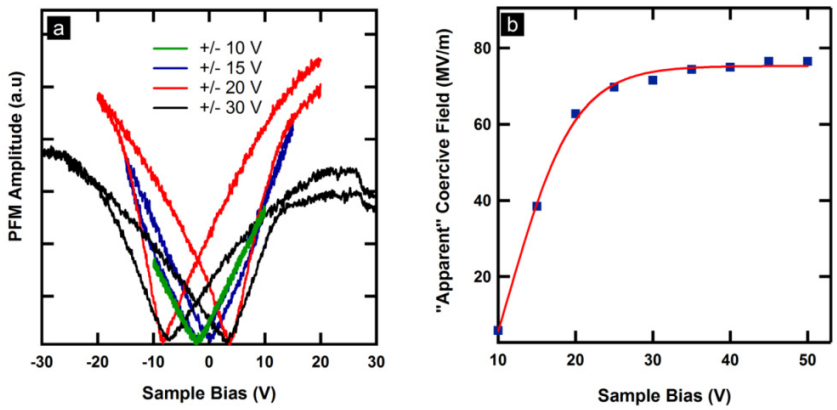

Figure 3.32: (a) PHL amplitude as a function of symmetric bias voltage of 80 nm thick continuous thin film and (b) is a plot of "apparent" coercive field as a function of applied sample bias of the same sample.

Figure 3.32(a) shows that when the limiting values of the sweeped sample bias increase progressively from +/- 10 V to +/- 30 V, the PFM amplitude signals open up (create hysteresis). For example when the applied dc bias is +/- 10 V there is hardly any opening. On the other hand, once the limiting value of dc bias is +/- 20 V or above the PFM amplitude curves do not vary anymore. This corresponds to an increase in the amount of switched dipole moments and finally reaching saturation. From the saturated phase PHLs the coercive field values can be obtained easily. The coercive field is the threshold field required to change the direction of polarization. The term "apparent" coercive field for the *y*-axis on Figure 3.32(b) is used since the real coercive field could only be obtained when the applied field is high enough to cause full saturation of polarization. The real coercive field corresponds to the plateau of the "apparent" coercive field of Figure 3.32 (b). For example, the coercive field from the PHL graph (Figure 3.32(a)) obtained by applying +/- 30 V symmetric dc bias is around 5.275 V / 80

nm = 70.2 MV/ m, since the coercive voltage is 5.275 V for a nearly 80 nm thick P(VDF-TrFE) continuous thin film. Note that, even if the coercive field is much lower than the applied poling voltage, implying that polarization switching starts at a much lower bias, we need to apply higher poling voltage (+/- 20 V) to fully switch the dipole moments of our P(VDF-TrFE) sample.

Actually, the switching voltage depends on the time of application of the field, and is related to the dynamics of the flipping of the polarization. Hence, the voltages required to switch fully the polarization are invariably larger than the "coercive voltage"; nevertheless, lower "coercive voltage" will also generally result in lower switching voltages. A quantitative analysis of PHL amplitude results is usually difficult. This is because the electric field generated by the AFM tip on the surface of ferroelectric samples is not homogeneous through the whole film thickness [47]. In other words, it means that the electromechanical coupling obtained underneath the polarized PFM tips is greatly localized. That is why the scale on the *y*-axis of Figures 3.31(a) and 3.32(a) is set as arbitrary unit (a.u).

It is interesting to note from Figure 3.31(a) and Figure 3.32(a) that the PHL amplitude does not saturate when the bias voltage increase above ~7V, because a linear electrostatic (capacitor) contribution adds up to the PFM amplitude [47, 49, 51]. We have tried to subtract this linear electrostatic contribution but it is found out to be tricky to do so, and this was then not performed in our thesis. An overall shift of the hysteresis loops toward the negative bias side (Figure 3.31 and 3.32(a)) and the positive bias side (Figure 3.33a) is observed. This effect is also reported in other ferroelectric materials and the reason was attributed to the polarization pinning due to either mechanical stress or charge trapping [57]. It

may also result from built-in voltages due to differences in work-functions of the bottom and top electrodes, and also to trapped charges in the structures.

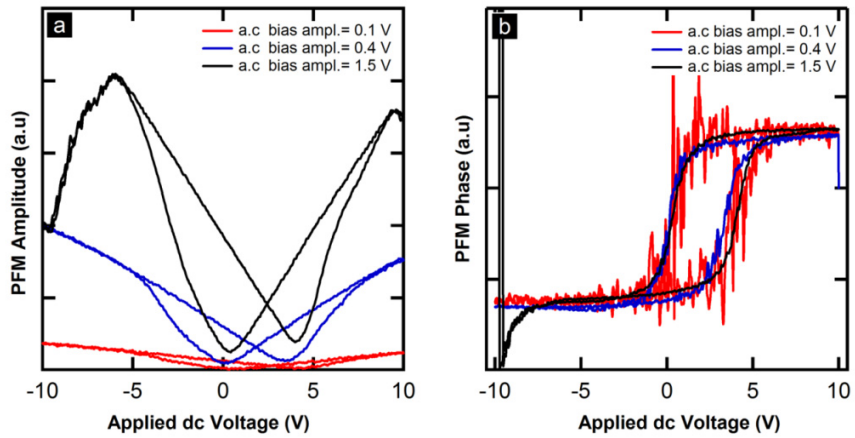

Figure 3.33: Dependence of PFM hysteresis effects on the amplitude of the ac drive.

It is also noteworthy to mention here that PHLs like the ones shown in Figure 3.31 are obtained only when some critical sweeping parameters (conditions) are optimized. One of the key issues is the peak-to-peak amplitude of the ac bias, sometimes referred to as the drive amplitude. To find reasonable values we have measured PHLs with drive amplitudes from 0.1 V to 1.5 V by 0.1 V increments, applied to a film of 80 nm thickness. Figure 3.33 shows the dependence of the measured PHLs amplitude and phase on the amplitude of applied ac bias. For clarity, only three selected PHLs with varying drive amplitudes are plotted in Figure 3.33.

Sweeping at 0.1 V ac drive amplitude causes a lot of noise as shown in Figure 3.33(b) and weak PFM response as well (Figure 3.33(a)). On the other hand,

when the amplitude of the ac bias is 1.5 V, the PFM amplitude decreased unexpectedly for dc voltages larger than ~5 V in absolute value (Figure 3.33(a)). The origin of this effect is not known; therefore, we did not perform PFM on such conditions. The switching loop measurement at the intermediate ac drive amplitude (0.4 V) gives a good PFM curve, with little noise and a behavior compatible with the expectations. Hence, 0.4 V drive amplitude was used for all PFM measurements presented in this thesis for film thicknesses around ± 100 nm. Nevertheless, these measurements show how the PHLs are strongly affected by the amplitude of drive bias in PFM experiments.

We have also found out that a series of hysteresis loops (at least 5) need to be performed at the same location before the final PHLs are recorded. The PHL amplitude and phase images underlining the importance of several sweeping at one location are presented in the Appendix, Figure A5. This effect might be related to the need to evacuate trapped charges. Other adjustable parameters in the PFM setup include: the "Gain" to scale up the input signal if the piezoelectric effect is weak and the "Bandwidth" to reduce the signal noise by applying a band-pass filter. In all of our PFM measurements the gain was adjusted to be x8, whereas the bandwidth was turned on only during hysteresis loop measurements and tuning (frequency sweep).

The other PFM parameter that we checked is the drive frequency of the ac bias. Conducting PFM amplitude and phase measurements at the resonance frequency of the cantilever leads to an enhanced electromechanical response, thus, enhanced signal-to-noise ratio (SNR) of PFM signals [48, 58, 59]. This effect can be used for both PHLs acquisition and PFM imaging mode, which is presented in the following section.

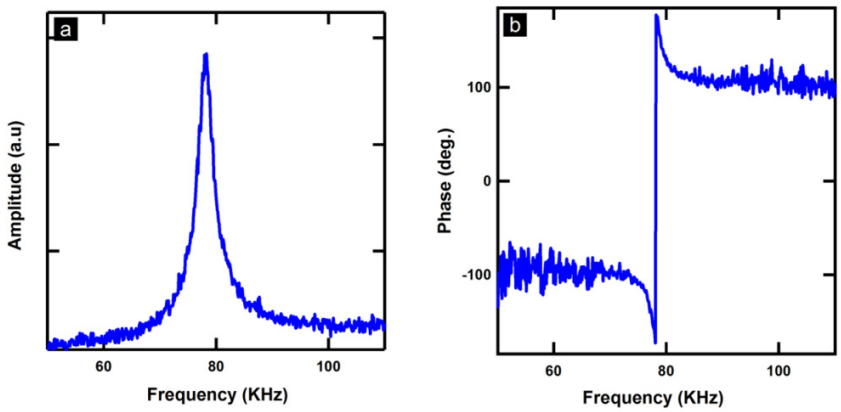

Figure 3.34: (a) amplitude and (b) phase of the cantilever response during a frequency sweeping of the ac bias on the sample (in this case, a 4 V dc voltage on the tip to increase the signal intensity.

The resonant frequency of the cantilever is obtained by performing a frequency sweep (tuning) for the ac voltage applied on the tip and which is in contact with the sample. From this sweeping measurement the amplitude/phase versus frequency curve can be recorded (Figure 3.34). The resonant peak shown in Figure 3.34(a) is defined by the mechanical properties of the cantilever and the stiffness of the tip-sample contact. In order to increase the signal amplitude, the sweeping measurements were done by applying a small dc bias (usually ~ 4V) either on the tip or the bottom electrode. The higher amplitude enables us to select the appropriate drive frequency close to the resonance frequency. The selection of the drive frequency is crucial in determining the direction of the polarization. For example, if the drive frequency is set exactly at the resonance frequency, the value of the drive frequency can be lower or higher than the resonance frequency during the PFM measurements. The unstable cantilever

contact resonance frequency can originate from a difference in tip-sample contact stiffness on different surface areas. Nevertheless, this makes the analysis of the PFM results more difficult. To avoid this complexity, in this thesis the drive frequency was always set at a value a little bit below the resonance peak. Using the harmonic oscillator model the amplitude and phase frequency response of the cantilever [60] is quantified as :

$$A(\omega) = \frac{A_{max}{\omega_0}^2/Q}{\sqrt{({\omega^2}_0 - \omega^2) + (\frac{\omega_0\omega}{Q})^2}} \qquad (3.7)$$

$$\tan\varphi(\omega) = \frac{\omega_0\omega}{Q({\omega^2}_0 - \omega^2)} \qquad (3.8)$$

where A_{max} is the amplitude at the resonance angular frequency ω_o, and Q is a quality factor that describes the energy loss in the system. Equation 3.7 shows mathematically how the PFM amplitude can be enhanced when ac drive frequency ω is close to the resonant frequency of the cantilever ω_o.

3.5.4 PFM Imaging

The other application of PFM is what is known as the PFM imaging mode. In these experiments the topography, PFM amplitude, and phase images are obtained simultaneously. The experimental setup for PFM imaging is similar to the one used for the PFM spectroscopy. However, here PFM images are usually

recorded once the poling (dc) bias is removed; poling is first performed onto specific regions, then mapping is performed with only the ac field. Hence, there is no contribution from the electrostatic (capacitor) component on the final PFM amplitude and phase images. This is one of the advantages of using this technique over the hysteresis loop measurements. However, polarization switching was inspected in PFM imaging mode by applying an oscillating voltage (amplitude 0.4 V) and a dc bias simultaneously. All PFM measurements are done by applying the ac driving bias on the cantilever while applying the dc bias voltage on the sample substrate.

In our thesis, PFM contrast images are obtained by poling the ferroelectric samples with dc voltages of opposite polarity. Figure 3.35 displays one example of PFM amplitude and phase images, obtained as follows. The sample is first scanned without bias over a scale of 10 μm x 10 μm. The resonance frequency of the cantilever is attained by putting the AFM tip on top of a single P(VDF-TrFE) pillar and subsequent tuning. Then, a positive voltage (20 V) is applied to the central square area of 6 μm x 6 μm. Again on a smaller square of 3 μm x 3 μm, a negative voltage (20 V) is applied. Eventually the dc bias is turned off and a scan is made over the initial scan area. The differences in color over the poled regions of the PFM phase image (Figure 3.35(b)) imply the switching of polarization when the polarity of the applied voltage is reversed. This is again characteristic to ferroelectric materials akin P(VDF-TrFE) copolymers. The PFM contrasts of Figure 3.35 were imaged again after 16 hours and they were identical (not shown in this thesis).

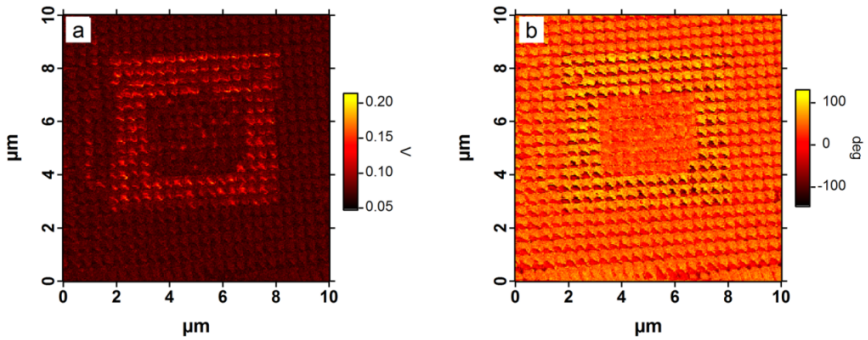

Figure 3.35: (a) Piezoresponse amplitude and (b) Piezoresponse phase images of the poled nanostructures of P(VDF-TrFE) surface.

To compare PFM images of Figure 3.35 the PFM amplitude and phase image of the structures before applying bias is shown in Figure 3.36. These figures do not reveal any special features (contrast). This confirms further that we indeed switched the direction of polarization, emphasizing the significance of PFM as a ferroelectric characterization technique.

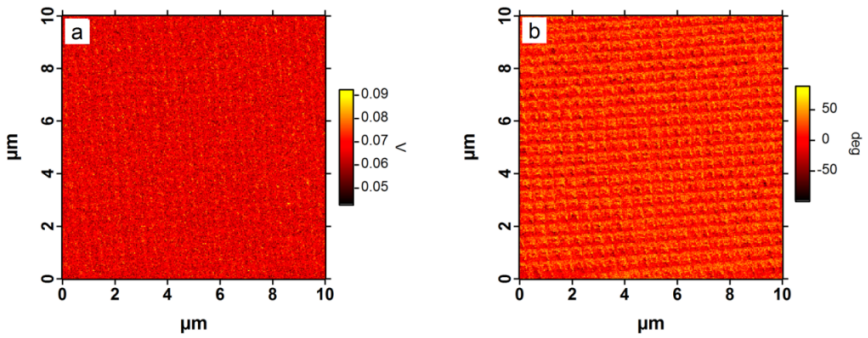

Figure 3.36: (a) Piezoresponse amplitude and (b) Piezoresponse phase images of arrays of nano-imprinted pillars before poling.

It should be mentioned that the lateral PFM amplitude and phase images which are recorded at the same time with vertical PFM images are not shown here. In our experimental setup the electric field is applied vertically; hence, there can only be weak lateral electromechanical coupling between the polarized tip and the underneath ferroelectric polymer. Consequently no or very little contrast is observed on the lateral PFM amplitude and phase images (not shown in this thesis).

Like PFM hysteresis loop measurements some PFM imaging parameters require optimization. In addition to poling at ac drive frequency close to the resonance frequency, the scanning rate or the time taken at one point should be high enough to cause polarization flipping. This is critical because the tip moves from one point to the next in a step motion. The scanned points then constitute a line. Because 256 points make one line, knowing the scanning rate, the time during which the tip stays at a single point can be calculated.

Figure 3.37 shows a plot of PFM contrast as a function of scanning speed (a) and the time spent at a single point (b). The PFM contrast is an arbitrary value defined by subtracting data acquired on areas poled upwards from those acquired on areas poled downwards. It is a measure of the electromechanical strength of ferroelectric materials. A more detailed explanation about PFM contrast acquisition is presented in the following chapter. We can see that to polarize the local area the pulse should be on for a few milliseconds (Figure 3.37(b)). The longer time spent on a single local point results in an improved PFM contrast (the plateau in Figure 3.37(b)). Conversely, a slow scanning speed results in higher PFM contrast. Thus, all our PFM poling (writing) and imaging (reading) experiments were performed at a scanning speed of 0.8 lines/s or around 5 milliseconds at one point. Obviously, scanning speeds slower than 0.8

lines/s at a point would have been preferable to get better PFM images but the total scanning time will increase enormously. For example, it takes around 45 minutes to complete one PFM image at a speed of 0.2 lines/s. So it is all about a compromise between a good PFM image and a reasonable scanning speed.

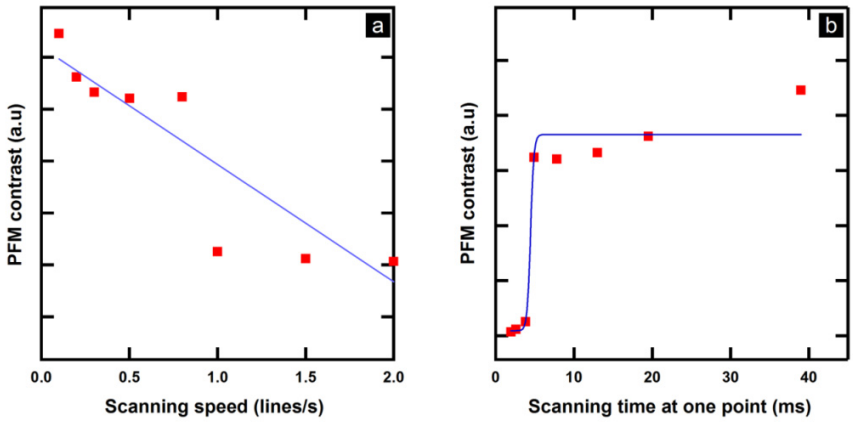

Figure 3.37: The dependence of PFM contrast on (a) the scanning speed both during poling and imaging and (b) on the time the PFM tip stays at a single point for 90 nm thick continuous film of P(VDF-TrFE) sample.

The other challenge of getting a good quality PFM image is the surface roughness of the ferroelectric samples. This is because the cantilever resonance frequency, which determines the quality of PFM images, is dependent on the tip-sample contact stiffness (roughness) [56]. For example, when the tip is in contact with a concave area of sample surface, the tip-sample contact stiffness is higher compared with the case when the tip is in contact with a smooth surface area. As a result, the contact resonant frequency gets higher. If the cantilever is being driven at a fixed resonant frequency measured while the tip is in contact

with the smooth area, a large drop in the PFM amplitude would occur. This is because the new contact resonance at the concave area is no longer the same at the specified frequency (smooth area). Hence, the PFM images are not the same over a larger surface area. The interpretation of the resulting PFM images is then much more difficult. If the effect of this resonance frequency variation is significant, the intended PFM contrast can even be masked.

This effect can be noticed in Figure 3.35 where darker and brighter contrasts are seen next to each other on a single imprinted nano-pillar, due to abrupt variations of topography at the edge of the pillars.

To summarize, in this section the working principles and the experimental settings of PFM used in this thesis were presented. Piezoresponse force microscopy (PFM) was then shown to be a powerful technique to characterize ferroelectric thin films and nano-imprinted patterns. In the following chapters PFM imaging and spectroscopy will be used as a main ferroelectric characterization technique.

Chapter 3

Bibliography

1. Hahmann, P. and O. Fortagne, *50 years of electron beam lithography: Contributions from Jena (Germany).* Microelectronic Engineering, **2009**. 86, 438-441.

2. Altissimo, M., *E-beam lithography for micro-nanofabrication.* Biomicrofluidics, **2010**. 4, 026503.

3. Mohammad, M., M. Muhammad, S. Dew, and M. Stepanova, *Fundamentals of Electron Beam Exposure and Development*, in *Nanofabrication*, M. Stepanova and S. Dew, Editors. 2012, Springer, Vienna. p. 11-41.

4. Groves, T.R., D. Pickard, B. Rafferty, N. Crosland, D. Adam, and G. Schubert, *Maskless electron beam lithography: prospects, progress, and challenges.* Microelectronic Engineering, **2002**. 61–62, 285-293.

5. Gates, B.D., Q. Xu, M. Stewart, D. Ryan, C.G. Willson, and G.M. Whitesides, *New approaches to nanofabrication: molding, printing, and other techniques.* Chemical Reviews, **2005**. 105, 1171-1196.

6. Manfrinato, V.R., L. Zhang, D. Su, H. Duan, R.G. Hobbs, E.A. Stach, and K.K. Berggren, *Resolution limits of electron-beam lithography toward the atomic scale.* Nano Letters, **2013**. 13, 1555-8.

7. Vieu, C., F. Carcenac, A. Pépin, Y. Chen, M. Mejias, A. Lebib, L. Manin-Ferlazzo, L. Couraud, and H. Launois, *Electron beam*

lithography: resolution limits and applications. Applied Surface Science, **2000**. 164, 111-117.

8. Broers, A.N., A.C.F. Hoole, and J.M. Ryan, *Electron beam lithography—Resolution limits.* Microelectronic Engineering, **1996**. 32, 131-142.

9. Hatzakis, M., *Electron Resists for Microcircuit and Mask Production.* Journal of the Electrochemical Society, **1969**. 116, 1033-1037.

10. Chen, Y., *A lift-off process for high resolution patterns using PMMA/LOR resist stack.* Microelectronic Engineering, **2004**. 73-74, 278-281.

11. Bang, J., U. Jeong, Y. Ryu du, T.P. Russell, and C.J. Hawker, *Block copolymer nanolithography: translation of molecular level control to nanoscale patterns.* Advanced Materials, **2009**. 21, 4769-92.

12. Park, M., *Block Copolymer Lithography: Periodic Arrays of 10^{11} Holes in 1 Square Centimeter.* Science, **1997**. 276, 1401-1404.

13. Stoykovich, M.P. and P.F. Nealey, *Block copolymers and conventional lithography.* Materials Today, **2006**. 9, 20-29.

14. Park, S., J.-Y. Wang, B. Kim, J. Xu, and T.P. Russell, *A Simple Route to Highly Oriented and Ordered Nanoporous Block Copolymer Templates.* ACS Nano, **2008**. 2, 766-772.

15. Park, H.J., M.-G. Kang, and L.J. Guo, *Large Area High Density Sub-20 nm SiO2 Nanostructures Fabricated by Block Copolymer Template for Nanoimprint Lithography.* ACS Nano, **2009**. 3, 2601-2608.

16. Fustin, C.A., B.G.G. Lohmeijer, A.S. Duwez, A.M. Jonas, U.S. Schubert, and J.F. Gohy, *Nanoporous Thin Films from Self-Assembled Metallo- Supramolecular Block Copolymers.* Advanced Materials, **2005**. 17, 1162-1165.

17. Gowd, E.B., M. Rama, and M. Stamm, *Nanostructures Based on Self-Assembly of Block Copolymers*, in *Nanofabrication*, M. Stepanova and S. Dew, Editors. 2012, Springer, Vienna. p. 191-216.

18. Yang, X., L. Wan, S. Xiao, Y. Xu, and D.K. Weller, *Directed Block Copolymer Assembly versus Electron Beam Lithography for Bit-Patterned Media with Areal Density of 1 Terabit/inch2 and Beyond.* ACS Nano, **2009**. 3, 1844-1858.

19. Cavicchi, K., K. Berthiaume, and T. Russell, *Solvent Annealing Thin Films of Poly(isoprene-b-lactide).* Polymer, **2005**. 46, 11635-11639.

20. Park, S., J.-Y. Wang, B. Kim, W. Chen, and T.P. Russell, *Solvent-Induced Transition from Micelles in Solution to Cylindrical Microdomains in Diblock Copolymer Thin Films.* Macromolecules, **2007**. 40, 9059-9063.

21. Park, S., B. Kim, J. Xu, T. Hofmann, B.M. Ocko, and T.P. Russell, *Lateral Ordering of Cylindrical Microdomains Under Solvent Vapor.* Macromolecules, **2009**. 42, 1278-1284.

22. Tang, C., E.M. Lennon, G.H. Fredrickson, E.J. Kramer, and C.J. Hawker, *Evolution of Block Copolymer Lithography to Highly Ordered Square Arrays.* Science, **2008**. 322, 429-432.

23. Hamley, I.W., *Ordering in thin films of block copolymers: Fundamentals to potential applications.* Progress in Polymer Science, **2009**. 34, 1161-1210.

24. Haubruge, H.G., X.A. Gallez, B. Nysten, and A.M. Jonas, *Image analysis of transmission electron micrographs of semicrystalline polymers: a comparison with X-ray scattering results.* Journal of Applied Crystallography, **2003**. 36, 1019-1025.

25. Chou, S.Y., P.R. Krauss, and P.J. Renstrom, *Imprint Lithography with 25-Nanometer Resolution.* Science, **1996**. 272, 85-87.

26. Guo, L.J., *Nanoimprint Lithography: Methods and Material Requirements.* Advanced Materials, **2007**. 19, 495-513.

27. Becker, H. and U. Heim, *Hot embossing as a method for the fabrication of polymer high aspect ratio structures.* Sensors and Actuators A: Physical, **2000**. 83, 130-135.

28. Jaszewski, R.W., H. Schift, J. Gobrecht, and P. Smith, *Hot embossing in polymers as a direct way to pattern resist.* Microelectronic Engineering, **1998**. 41–42, 575-578.

29. Schift, H., R.W. Jaszewski, C. David, and J. Gobrecht, *Nanostructuring of polymers and fabrication of interdigitated electrodes by hot embossing lithography.* Microelectronic Engineering, **1999**. 46, 121-124.

30. Guo, L.J., *Recent progress in nanoimprint technology and its applications.* Journal of Physics D: Applied Physics, **2004**. 37, R123.

31. Peroz, C., V. Reboud, and C.S. Torres, *Nanoimprint Technologies*, in *Nanofabrication*, M. Stepanova and S. Dew, Editors. 2012, Springer, Vienna. p. 117-140.

32. Chou, S.Y., P.R. Krauss, W. Zhang, L. Guo, and L. Zhuang, *Sub-10 nm imprint lithography and applications.* Journal of Vacuum Science & Technology B: Microelectronics and Nanometer Structures, **1997**. 15, 2897-2904.

33. Maximov, I., E.-L. Sarwe, M. Beck, K. Deppert, M. Graczyk, M. Magnusson, and L. Montelius, *Fabrication of Si-based nanoimprint stamps with sub-20 nm features.* Microelectronic engineering, **2002**. 61, 449-454.

34. Hu, Z. and A.M. Jonas, *Control of crystal orientation in soft nanostructures by nanoimprint lithography.* Soft Matter, **2010**. 6, 21.

35. Hu, Z., M. Tian, B. Nysten, and A.M. Jonas, *Regular arrays of highly ordered ferroelectric polymer nanostructures for non-volatile low-voltage memories.* Nature Materials, **2009**. 8, 62-7.

36. Zhang, L., S. Ducharme, and J. Li, *Microimprinting and ferroelectric properties of poly(vinylidene fluoride-trifluoroethylene) copolymer films.* Applied Physics Letters, **2007**. 91, 172906.

37. Hu, Z., G. Baralia, V. Bayot, J.-F. Gohy, and A.M. Jonas, *Nanoscale Control of Polymer Crystallization by Nanoimprint Lithography*. Nano Letters, **2005**. 5, 1738-1743.

38. Hu, Z., B. Muls, L. Gence, D.A. Serban, J. Hofkens, S. Melinte, B. Nysten, S. Demoustier-Champagne, and A.M. Jonas, *High-Throughput Fabrication of Organic Nanowire Devices with Preferential Internal Alignment and Improved Performance.* Nano Letters, **2007**. 7, 3639-3644.

39. Scheer, H.C. and H. Schulz, *A contribution to the flow behaviour of thin polymer films during hot embossing lithography*. Microelectronic Engineering, **2001**. 56, 311-332.

40. Binnig, G., C.F. Quate, and C. Gerber, *Atomic Force Microscope.* Physical Review Letters, **1986**. 56, 930-933.

41. Goldstein, J., D.E. Newbury, D.C. Joy, C.E. Lyman, P. Echlin, E. Lifshin, L. Sawyer, and J.R. Michael, *Scanning electron microscopy and X-ray microanalysis*. 2003: Springer, New York.

42. Kalantar-Zadeh, K. and B.N. Fry, *Nanotechnology-enabled sensors*. 2008: Springer, New York.

43. Stuart, B.H., *Infrared spectroscopy: fundamentals and applications*. 2004: Wiley, West Sussex.

44. Smith, B.C., *Fundamentals of Fourier transform infrared spectroscopy*. 2011: CRC Press, Boca Raton.

45. Gedde, U.W., *Polymer physics*. 1995: Springer, London.

46. Eng, L.M., M.B.C. Loppacher, M.G.R. Bennewitz, R. Lüthi, E.M.T. Huser, H. Heinzelmann, and H.J. Güntherodt, *Ferroelectric domain characterisation and manipulation : A challenge for scanning probe microscopy.* Ferroelectrics, **1999**. 222, 153-162.

47. Kholkin, A., S. Kalinin, A. Roelofs, and A. Gruverman, *Review of Ferroelectric Domain Imaging by Piezoresponse Force Microscopy*, in *Scanning Probe Microscopy*, S. Kalinin and A. Gruverman, Editors. 2007, Springer, New York. p. 173-214.

48. Vasudevan, R., S. Jesse, Y. Kim, A. Kumar, and S. Kalinin, *Spectroscopic imaging in piezoresponse force microscopy: New opportunities for studying polarization dynamics in ferroelectrics and multiferroics.* MRS Communications, **2012**. 2, 61-73.

49. Kalinin, S.V., A.N. Morozovska, L.Q. Chen, and B.J. Rodriguez, *Local polarization dynamics in ferroelectric materials.* Reports on Progress in Physics, **2010**. 73, 056502.

50. Kalinin, S.V. and D.A. Bonnell, *Imaging mechanism of piezoresponse force microscopy of ferroelectric surfaces.* Physical Review B, **2002**. 65, 125408.

51. Soergel, E., *Piezoresponse force microscopy (PFM).* Journal of Physics D: Applied Physics, **2011**. 44, 464003.

52. Gaynutdinov, R.V., O.A. Lysova, A.L. Tolstikhina, S.G. Yudin, V.M. Fridkin, and S. Ducharme, *Polarization switching kinetics at the*

nanoscale in ferroelectric copolymer Langmuir–Blodgett films. Applied Physics Letters, **2008**. 92, 172902.

53. Rodriguez, B.J., S. Jesse, J. Kim, S. Ducharme, and S.V. Kalinin, *Local probing of relaxation time distributions in ferroelectric polymer nanomesas: Time-resolved piezoresponse force spectroscopy and spectroscopic imaging.* Applied Physics Letters, **2008**. 92, 232903.

54. Rodriguez, B.J., S. Jesse, S.V. Kalinin, J. Kim, S. Ducharme, and V.M. Fridkin, *Nanoscale polarization manipulation and imaging of ferroelectric Langmuir-Blodgett polymer films.* Applied Physics Letters, **2007**. 90, 122904.

55. Sharma, P., T. Reece, D. Wu, V.M. Fridkin, S. Ducharme, and A. Gruverman, *Nanoscale domain patterns in ultrathin polymer ferroelectric films.* Journal of Physics: Condensed Matter, **2009**. 21, 485902.

56. Proksch, R. and S. Kalinin, *Piezoresponse Force Microscopy with Asylum Research AFMs* PFM App Note, **2008**.

57. Wang, Z., A.P. Suryavanshi, and M.-F. Yu, *Ferroelectric and piezoelectric behaviors of individual single crystalline BaTiO[sub 3] nanowire under direct axial electric biasing.* Applied Physics Letters, **2006**. 89, 082903.

58. Rodriguez, B.J., C. Callahan, S.V. Kalinin, and R. Proksch, *Dual-frequency resonance-tracking atomic force microscopy.* Nanotechnology, **2007**. 18, 475504.

59. Gruverman, A., B.J. Rodriguez, R.J. Nemanich, and A.I. Kingon, *Nanoscale observation of photoinduced domain pinning and investigation of imprint behavior in ferroelectric thin films.* Journal of Applied Physics, **2002**. 92, 2734.

60. Sader, J.E., *Frequency response of cantilever beams immersed in viscous fluids with applications to the atomic force microscope.* Journal of Applied Physics, **1998**. 84, 64-76.

Chapter 4

Structure and Ferroelectric Properties of Nanoimprinted Poly(Vinylidene Fluoride-*ran*-Trifluoroethylene)

Hailu G. Kassa,[1] Ronggang Cai,[1] Alessio Marrani,[2] Bernard Nysten,[1] Zhijun Hu,[3] and Alain M. Jonas[1] (Macromolecules **2013**, 46, 8569-8579)

(1) Université catholique de Louvain, Croix du Sud 1/L7.04.02, B1348
Louvain-la-Neuve, Belgium
(2) Solvay Specialty Polymers Italy S.P.A.,
Viale Lombardia, n° 20, Bollate (MI), 20021 (Italy)
(3) Soochow University, Suzhou 215006 (China)

This chapter shows how it is possible to control the microstructure and local ferroelectric behavior of P(VDF-TrFE) by confining the polymer in the cavities of nanoimprinting molds. Specifically, we report in detail how the geometric constraints of the mold and the nanoimprinting process parameters result in a preferential crystal orientation or not of P(VDF-TrFE) semicrystalline copolymer, and how the local ferroelectric properties of the resulting nanostructures are correlated to the microstructural changes.

Chapter 4

4.1 Abstract

Nanoimprint lithography (NIL) was used to shape thin films of a ferroelectric copolymer of vinylidene fluoride and trifluoroethylene (PVDF-TRFE), using a variety of molding shapes and imprinting conditions. The morphology of the layers was characterized by atomic force microscopy (AFM), and preferential orientation of the crystallographic axes was monitored by infrared micro-spectroscopy; in addition, the local ferroelectric properties were obtained by piezoresponse force microscopy (PFM). When the sample is imprinted in its paraelectric phase in conditions leading to complete confinement, in cavities of size lower than the natural lamellar length observed in a continuous thin film, the crystallographic *a* axis aligns preferentially parallel to the substrate, and the crystalline lamellae are of significantly reduced length. These characteristics translate in a strongly decreased coercive field and accelerated ferroelectric switching, which is in part ascribed to the improved coupling between the electric field and the properly-oriented dipole moments. When decreasing the confinement either by leaving a residual film connecting the nanopillars, or by increasing the lateral size of the nanopillars above the natural lamellar length, or by using line molds where confinement only exists in one direction, or by using continuous films, the preferential orientation becomes less visible and the lamellar length increases, resulting in increased coercive and switching fields. Interestingly, the average length of the crystalline lamellae tends to correlate with the value of the coercive field. Finally, if the sample is imprinted in the melt, a flat-on setting of the crystalline lamellae ensues, with a vertical chain axis which is unfavorable for ferroelectric properties probed with a vertical electric field.

4.2 Introduction

Easy switching of polarization states of ferroelectric materials by an external electric field opens up the possibility to electrically control their properties and provides a physical basis for the fabrication of electronic devices like non-volatile ferroelectric random access memories (FeRAM) [1-5]. Due to their high flexibility, low cost and easy solution processability, organic ferroelectric polymers are getting considerable interest over inorganic ferroelectric materials [6]. Poly(vinylidene fluoride) (PVDF) and its copolymers with trifluoroethylene (TrFE) are widely-investigated ferroelectric polymers because of their large polarization and excellent switching characteristics making them particularly attractive for non-volatile memory applications [7-12]. In order to integrate P(VDF-TrFE) in an all-organic low power electronic device, it is desirable to decrease its switching voltage while preserving data retention. Since the switching voltage is related to the 'coercive voltage' defined as the product of the coercive field by the film thickness, the coercive field being defined as the electric field required to zero the spontaneous polarization, lower switching voltages can be attained by decreasing the film thickness. This was however reported to lead to deteriorated ferroelectric properties [13]; recent reports indicate this to be related to preferential crystal orientation, a factor which can be controlled by proper processing [14-17].

Confining ferroelectric polymers into nanocavities was also reported to control crystal orientation, leading to improvements of the ferroelectric properties. Confinement of P(VDF-TrFE) can be achieved within the grooves of self-assembled organosilicate (OS) lamellar structures [18], by wetting nanoporous alumina templates to produce nanorods [19, 20], or by using nanoimprint

lithography (NIL) [21-28]. In these studies, the molecular orientation of P(VDF-TrFE) was affected by the confinement, resulting in modified ferroelectric properties. Among the aforementioned confinement techniques, nanoimprint lithography is especially promising because the fabricated regular nano-patterns can be used in applications like those of dense mass storage media [28]. Nanoimprint lithography or nano-embossing is a low cost and rapid technique which creates nanofeatures by mechanically deforming a molten amorphous polymer film when pressed against a hard mold [27].

Recently, our group reported on the use of nanoimprint lithography technique to produce high-density regular arrays of P(VDF-TrFE) nanostructures where the orientation of the *c* (chain) and *a* axes was aligned in plane to the substrate [28]. The improved crystal orientation led to a significant decrease in the operational voltage by up to a factor of five. Nevertheless, the detailed understanding of the influence of nanoimprint lithography on the crystallization process and the ferroelectric properties was not yet studied. Furthermore, no attempt was performed to tune the structure of the nanoimprinted P(VDF-TrFE) by playing with processing parameters or chain structure, although it is known that such parameters are critical on the crystal orientation and ferroelectric properties of (PVDF-TrFE) [4, 29]. Possible parameters to control are the composition of the PVDF copolymer and different external variables like temperature and pressure during imprint. Another important parameter is the residual film thickness, i.e., the thickness of the film that remains between the surface of the substrate and the protrusions of the mold, when the mold is fully pressed in the film. It was reported that this residual thickness has a critical role to play when crystallizing polymers in nanoconfinement [25]. Most importantly, the exact reasons for the dramatic improvement of the ferroelectric performances of P(VDF-TrFE) after nanoimprinting are not yet known. This knowledge will not only be of direct

interest for plastic memory applications, but will also provide basic information on the way the structure of semicrystalline polymers can be controlled by nanoconfinement under pressure, and on the way nanoconfinement affects ferroelectricity.

In this chapter, we report on the effect of confinement and processing parameters during nanoimprinting on morphology and crystal orientation as well as on the resulting ferroelectric properties of P(VDF-TrFE) nanostructures. As processing parameters, we essentially played with the initial film thickness and imprinting temperature. The geometrical constraints like size and shape (square or line) of the cavities of the hard mold used for the nanoimprinting process are also explored. The morphology and crystal orientation of continuous and nanostructured P(VDF-TrFE) are characterized by atomic force microscopy (AFM) and Fourier transform infrared spectroscopy (FTIR), respectively. The nanoscale ferroelectric properties are investigated by piezoresponse force microscopy (PFM). PFM hysteresis loops are used to get information about the coercive field while the PFM imaging mode is used to study more globally the switching of local polarization. Our results show the importance of the residual film thickness and lateral cavity size on the improvement of ferroelectric properties, and illustrate the different crystal settings that result from using different imprinting conditions or molds.

4.3 Experimental Section

4.3.1 Sample preparation and methods

The poly(vinylidene fluoride-co-trifluoroethylene) copolymer (PVDF-TrFE) with 70/30 weight % of TrFE and M_w = 230 kg/mol was from Solvay Specialty Polymers (Italy) and used as-received. The melting temperature of this polymer was 143°C, and its Curie transition temperature was 117°C, as determined by differential scanning calorimetry at 10°C/min. The P(VDF-TrFE) powder was dissolved in cyclohexanone (25 g/L). Thin films were prepared by spin-coating on a highly *n*-doped silicon substrate (resistivity 0.3-0.5 Ω.cm). The film thickness was varied by changing the spin speed. The resulting thin film thickness was measured by profilometry and ellipsometry using 1.4 as the index of refraction. The SiO_2 hard molds were home-made by electron beam lithography (EBL). EBL is a standard lithography technique where a designed pattern is transferred from an electron-sensitive resist (PMMA) to the silicon substrate by lift-off and reactive ion etching procedures. Hard molds of different size and shape were prepared, with an effective patterned area of ca. $(100\ \mu m)^2$. The limited patterned surface is the result of the slowness of EBL, preventing us to realize molds of larger patterning size. The height of the protrusions (i.e., the depth of the cavities) was controlled during the etching process. In order to separate the mold easily after imprinting, it was coated with a monolayer of perfluorodecyldimethylchlorosilane deposited from the liquid phase. The molds were silanized repeatedly after a few NIL experiments.

The nanostructures were fabricated by nanoimprint lithography using an Obducat 3-inch imprinter in a class 1,000 clean room environment. Initially, a

continuous thin film of P(VDF-TrFE) was prepared by spin coating on the *n*-doped silicon substrate. Before applying pressure to imprint, the thin film was heated at T_{print} (usually, 125°C). The print mold was pressed against the film under a pressure of 60 bar at T_{print} for 10 min to make sure that the nano-cavities in the printing mold were completely filled. After the system was cooled to 60°C, the pressure was reduced to zero and the mold was finally removed from the samples for characterization.

4.3.2 Characterization of the morphology and structure

The morphology of the continuous thin films and nanostructures was inspected using either a Multimode AFM (Nanoscope IV, Bruker) or an Agilent 5500 AFM (Agilent Technologies) in tapping mode using silicon cantilevers from Nanosensors (with a force constant of ~ 40 N/m and an apex radius of curvature < 7 nm). The molecular orientation of P(VDF-TrFE) samples was investigated by Fourier-transform infrared microscopy (continuμm microscope from Thermo Scientific) in transmission mode thanks to the transparency of silicon in the useful range of the IR spectrum. To ensure a high signal-to-noise ratio, all spectra were averages of 128 scans with a resolution of 8 cm^{-1}. For line array samples, a polarizer was placed in the outgoing beam, with the polarization direction either parallel or perpendicular to the lines.

Quantitative analysis of the infrared spectra. The infrared absorption spectra A were fit between 1030 and 1512 cm^{-1} by a model comprising a polynomial baseline (of order 3), the scaled signal of the bare silicon wafer, the scaled signal of amorphous P(VDF-TrFE) taken here as identical to the signal of molten PVDF reported in Figure 9 of Kobayashi et al. [30], and the sum of 7 crystalline peaks represented by Voigt functions of adjustable location, shape, width and

amplitude. The locations of the peaks were constrained to be within +/- 2 cm^{-1} from the values reported by Prabu et al [31] for the crystalline peaks of P(VDF-TrFE) in this region (1430, 1404, 1342, 1292, 1184, 1127, and 1080 cm^{-1}). In order to decrease the number of fittable parameters, the width and shape of the weaker peaks at 1430, 1342, 1127 and 1080 cm^{-1} were held fixed to the average value found for the stronger peaks. The scale factors of the amorphous and silicon signals were two supplementary fittable parameters. However, the scaling factor of the Si signal was constrained to lie between 0.95 and 1.05, corresponding to the nominal variation of thickness of the Si wafers used in this study. A similar procedure was followed to fit the infrared signal between 650 and 1030 cm^{-1}; in this case, however, only two crystalline peaks were used at 884 and 848.5 cm^{-1}, with the second peak having its width and shape held at the value of the stronger one; in addition, the baseline was a polynomial of order 5.

At the end of the fitting procedure, the scaled Si signal and the polynomial baseline were subtracted from the experimental signal, and the so-obtained absorption spectrum was normalized by division by the thickness of the P(VDF-TrFE) film expressed in nanometers. For imprinted samples, the thickness was taken as the one before imprinting, a valid approximation because the absorbance of the film is very small. The scaled spectrum of the fitted amorphous component was normalized similarly. The normalized spectrum of the crystalline component was obtained by subtracting the normalized amorphous component from the normalized baseline-corrected infrared spectrum.

The crystallinity was evaluated by taking the ratio of the areas of the normalized crystalline and global spectra between 1000 and 1500 cm^{-1}. The crystalline component was then divided by the crystallinity to obtain the pure crystalline

spectrum; this spectrum, free of effects due to crystallinity, was used to evaluate the preferential orientation of the crystals.

4.3.3 Characterization of ferroelectric properties

An Agilent 5500 AFM (Agilent technologies) system equipped with a Mac III Controller lock-in amplifier was adapted to the requirements of the piezoresponse force microscopy (PFM) technique. PFM was used to study the local polarization switching and local ferroelectric properties of continuous thin films and imprinted nanostructures. In order to make PFM measurements, the *n*-doped silicon substrate under the polymer film was used as a bottom electrode. A conducting boron-doped-diamond-coated Si cantilever (from Nanosensors) with a force constant of 0.02-0.77 N/m was used as a top electrode.

The PFM setup allows us to record local piezoresponse hysteresis loops (PHL's) of nano-cells and continuous thin films, from which information about the coercive field is retrieved easily. The PHL's were obtained with the cantilever voltage modulated at the cantilever resonance frequency in order to enhance the signal-to-noise ratio (SNR) of the PFM amplitude and phase measurements. The polarization switching was inspected in PFM image mode using an oscillating voltage (amplitude 0.5 V) and DC bias simultaneously. All PFM measurements were done by applying an AC driving bias on the cantilever while applying the DC bias voltage on the sample substrate.

4.4 Results and Discussion

4.4.1 The effect of nano-processing parameters

The effect of residual layer on the crystallization of nanoimprinted P(VDF-TrFE) nanostructures. Continuous P(VDF-TrFE) ultrathin films were spin-coated on a highly doped Si substrate. They were then annealed for 10 minutes at 125°C, a temperature above the Curie point (T_c) but below the melting point (T_m). Figure 4.1 shows AFM height and phase images of a 95 nm thick P(VDF-TrFE) continuous thin film consisting of randomly oriented lamellae.

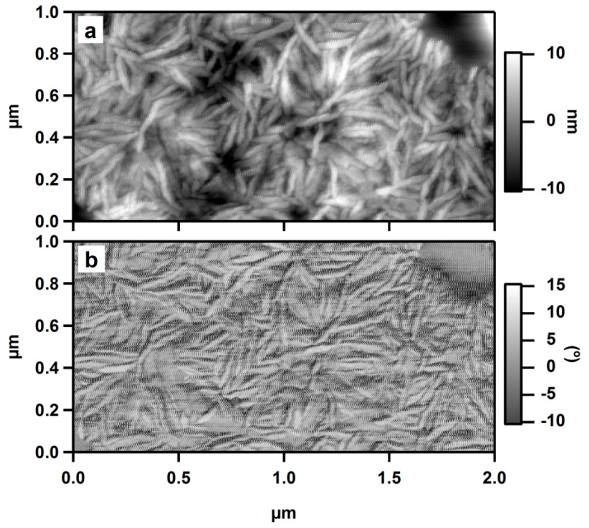

Figure 4.1: AFM morphology of a continuous ultrathin film. **(a)** Height and **(b)** phase images of 95 nm thick annealed continuous P(VDF-TrFE) thin film showing randomly oriented crystal lamellae.

In order to study the effect of the residual layer on the crystallization and its subsequent ferroelectric property, the ratio of the initial film thickness d to the cavity depth h of the mold should be known. For molds consisting of a square array of square cavities of period p and lateral cavity size l, the surface fraction of cavities is l^2/p^2 (ca. 0.5 in the present case). Then, a residual layer exists after imprinting if $d.p^2/l^2 \geq h$. In other words, when the film thickness d is much larger than the cavity depth h, there will be a residual layer between the nanopillars after embossing, a situation we call partial confinement. In the present work, imprinting with an initial film thickness (d) of 74 nm and 95 nm along with a hard mold of geometrical parameters p=350 nm and l=250 nm, resulted in 22 nm and 43 nm thick residual films respectively. Imprinting was made at 125°C for 10 minutes in the paraelectric phase of P(VDF-TrFE) copolymers. Of note, the imprinting temperature is the same as the annealing temperature of the continuous thin films.

Figure 4.2a-c shows typical AFM images of an imprinted sample with a 43 nm thick residual film. The full scale AFM height image (Figure 4.2a) shows only the topmost part of the regularly patterned nanosquares, which does not provide a clear view of the bottom residual layer between the nanosquares. To get a better view of the small crystalline lamellae over the whole scanned surface, we have combined together two separate images as shown in Figure 4.2b. This is achieved by having a height image that shows explicitly the topmost part of the nanosquares combined with another image that shows clearly the residual layer, each of the two images having its own color scale of identical range but different offset. Such composite topography images provide information that correlates very well with phase images (Figure 4.2c).

Imprinted samples under partial confinement with 43 nm thick residual layer display randomly oriented lamellae as shown in Figures 4.2b and c, both on the

top of the nanoimprinted pillars and on the residual layer between them. The crystalline lamellae of partially confined nanostructures are structurally similar to those of continuous ultrathin films (Figures 4.1a and b). This is because the presence of a thin residual film led to a fast crystal growth below the protrusions of the mold, from which crystallization propagates into the square grooves of the mold. Thus, the final morphology is not solely controlled by the hard mold, but mainly by the residual film during the imprinting process [25]. It should be mentioned that the AFM topography image of nanoimprinted structures in the partial confinement regime with 22 nm residual layer thickness is presented only in Appendix, Figure B1, which is in fact more or less similar to the one with 43 nm residual layer thickness (Figure 4.2(a-c)).

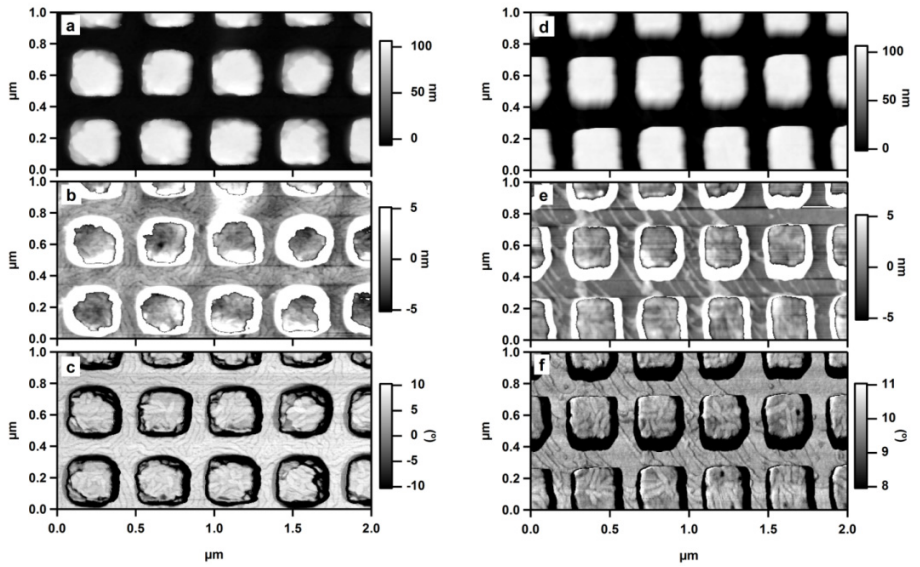

Figure 4.2: AFM morphology of an array of $(250\ nm)^2$ imprinted P(VDF-TrFE) nanopillars. **(a-c)** AFM images of nanoimprinted structures in the partial confinement regime with 43 nm residual layer thickness : Height image **(a)**, a combined height image of the topmost and bottom part of the nanoimprinted structures in the partial confinement regime showing the presence of crystal lamellae on the residual layer **(b)** and phase image **(c)**. **(d-f)** AFM images of nanoimprinted patterns in full confinement regime: Height image **(d)**, a combined height image of the topmost and bottom part of the array with almost no polymer left between the nanopillars **(e)** and phase image **(f)**.

On the other hand, if the topmost part of the hard mold is in contact with the Si substrate, there will not be any remaining polymer between the imprinted features. This leads to imprinting in conditions of complete confinement, where each nanopillar is totally isolated from the others with little or no underlying

residual film. Full confinement is achieved when $d.p^2/l^2 \leq h$. Using the same square mold used in the partial confinement experiments and a 50 nm initial film thickness of P(VDF-TrFE), 100 nm high nanopillars are obtained. Here, the 50 nm initial film thickness compared with the higher depth of the nanocavities (100 nm) ensures a direct contact between the hard mold and the substrate during imprinting. Figure 4.2d-f shows typical AFM images of fully confined arrays of nanopillars. The combined AFM height (Figure 4.2e) and phase images (Figure 4.2f) show the presence of only a few and discontinuous polymer filaments connecting individual pillars. Hence, the three dimensional full confinement and an almost complete isolation of the nanosquares prevent the crystal growth propagating across the nanostructures. Nevertheless, the nanopillars remain polycrystalline.

To be precise on our morphology analysis, the length and distribution of 50 individual crystalline lamellae on each of the AFM images of Figure 4.1and 2 have been measured manually. The distribution of the lamellae length of these samples is plotted in Figure 4.3. The annealed continuous ultrathin film sample has a wider distribution of lamellae length, and the average length of its lamellae is 207 nm by number and 217 nm by surface. In contrast, nanopillars of 250 nm lateral side imprinted in conditions of full confinement have a narrower distribution of lamellar length with an average of 75 nm by number (82 nm by surface), well below the side length of the confining cavities.

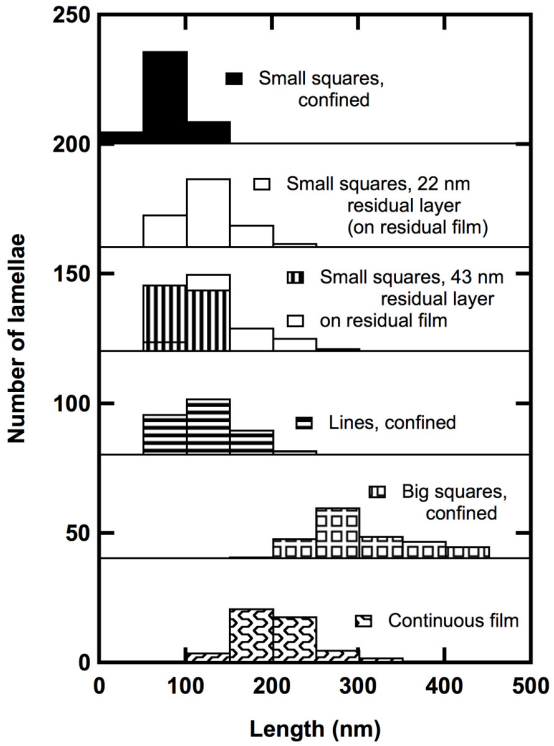

Figure 4.3: Length distributions of 50 individual lamellae taken from fully confined pillars of 250 nm lateral side (solid), imprinted pillars of 250 nm lateral side with 22 nm thick residual layer (white, on the residual film between them), imprinted pillars of 250 nm lateral side with 43 nm thick residual layer (vertical lines: on the nanopillars only; white: on the residual film between them), fully confined imprinted lines (horizontal lines), fully confined pillars of 500 nm lateral side (open squares) and continuous ultrathin films (folded patterns).

Partially confined nanopillars with 43 nm residual thickness have a slightly larger average lamellar length by number of 96 nm (101 nm by surface), when measured over the nanopillars, whereas the average length on the residual film

between the nanopillars is 145 nm by number (159 nm by surface). When the residual layer thickness decreases to 22 nm, the average lengths on the residual film drop to 123 and 131 nm for the number and surface averages, respectively (the average lengths could not be determined on the pillars). As a result, the average lamellar length falls in-between the one of the continuous thin film and of the fully confined nanopillars. These observations already indicate a perturbation of the crystallization process by the (partial) confinement. The smaller lamellar length obtained when confining the crystallization process indicates a higher nucleation density compared to the continuous thin film. Similarly to other systems [25, 27, 32-36], this is most probably due to the division of the melt into many small cavities, which results in the exclusion and thus reduction of heterogeneous nucleation sites from many cavities and therefore a trend towards homogeneous nucleation occurring at lower temperatures. However, it should be mentioned that the surface of the silicon substrate can serve as a nucleation site; as a result the crystallization process cannot be solely homogeneous.

Information on crystal orientation was investigated by Fourier-transform infrared spectro-microscopy (FTIR) in transmission. Grazing-Angle X-ray Scattering was not used because of the limited patterned area (ca. $(100\ \mu m)^2$), whereas electron diffraction was not selected owing to the difficulty to obtain quantitative information due to the extreme sensitivity of P(VDF-TrFE) crystals to electron radiation. Each sample provides its own characteristic FTIR spectrum resulting from the interaction of the incident electric field with the molecular vibration of the samples. In our experimental setup the electric field component of the IR beam is aligned parallel to the substrate within a finite opening angle due to the use of a Cassegrain condenser. Therefore, the absorption peaks correspond to vibrations having their transition dipole moments lying in this

angular range, on average parallel to the substrate. The detailed molecular vibrations of the three crystal forms of PVDF and their absorption band assignments can be found elsewhere [30, 31]. For the β phase, the strong absorption peak at 1400 cm^{-1} corresponds to the wagging vibration of CH_2 groups, which has a transition dipole moment μ_c parallel to the chain *c* axis, while the peak at 1180 cm^{-1} is attributed to an anti-symmetric stretching and rocking vibration of CF_2 (μ_a parallel to the *a* axis). In addition, the absorption peak at 1288 cm^{-1} is assigned to the symmetric stretching vibration of CF_2 parallel to the polar *b* axis [28].

Figure 4.4a shows the thickness-normalized infrared spectra of a series of continuous films processed in different ways, together with the computed spectrum of their amorphous component (dashed line). From this decomposition (fully explained in the Experimental Section), the crystallinity of the samples could be obtained; it is also indicated in the Figure. Because the amplitude of the crystalline absorption bands of the samples is affected by both crystallinity and orientation, we have computed the spectra of the pure crystalline component, free from crystallinity-related effects, by computing the difference between the total and amorphous spectra, divided by crystallinity (Figure 4.4b). These pure crystalline spectra correspond to 100% crystallinity, and are thus only sensitive to orientation effects. One should be aware that, because Si has a relatively strong band at 1107 cm^{-1}, the P(VDF-TrFE) spectra cannot be reliably obtained between 1070 and 1140 cm^{-1}; however, this is a region where only small absorption bands are found for P(VDF-TrFE). In addition, the signal of the bare Si wafer is also quite rich and complex below 1000 cm^{-1}; therefore, the two P(VDF-TrFE) bands found in this region will not be discussed in the sequel, as they are likely to be much less accurate.

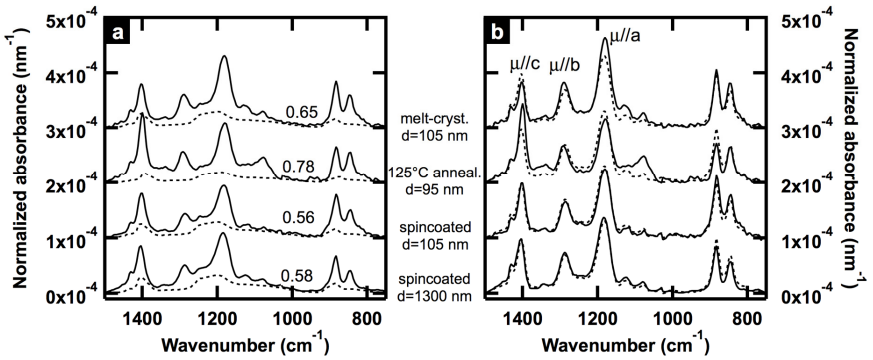

Figure 4.4: (a) Thickness-normalized infrared transmission spectra, corrected for baseline and Si absorption, of P(VDF-TrFE) continuous thin films. The dashed line is the amorphous component; the numbers are the crystallinity. **(b)** Corresponding thickness-normalized infrared spectra of the crystalline component, scaled to unit crystallinity. The dashed line is the spectrum of the reference spin-coated sample. From bottom to top : spin-coated film of 1300 nm thickness; spin-coated film of 105 nm thickness; film of 94 nm thickness, annealed at 125°C; film of 105 nm thickness, crystallized from the melt. The curves are shifted vertically by integral multiples of 0.0001 nm^{-1} for clarity.

The two films measured after spin-coating (lower traces in Figure 4.4) exhibit a close crystallinity of about 57%, despite having rather different thicknesses (1300 and 105 nm, respectively). In addition, the spectra of their pure crystalline components almost superimpose (Figure 4.4b). Therefore, it is reasonable to assume that these films have relatively isotropic distributions of crystal orientation, in agreement with previous studies [37]; a reference crystalline spectrum was thus computed by averaging these two spectra. It appears as the dashed line in Figure 4b, and will serve as reference for discussing relative

orientations in the sequel. The film annealed in the paraelectric state at 125°C (third trace from bottom in Figure 4.4) has a significantly higher crystallinity, close to 80%. In addition, the pure spectrum of its crystalline component indicates that the chain *c*-axis tends to align better in the plane of the substrate. In contrast, when crystallized from the melt, the *a*-axis tends to lie in-plane, whereas the *c*-axis slightly tilts towards the normal. This corresponds to a more flat-on orientation of the lamellae and is unfavorable for easy dipole rotation in the presence of a vertical electric field. These observations fully confirm previous reports on the effect of annealing temperature on crystal setting [14, 15, 29, 31, 37], and therefore validate our methodology. However, it should be realized that the changes observed remain weak, which is due to the distribution of the orientation of the IR electric field resulting from the use of a Cassegrain condenser.

The infrared data for imprinted nanopillars of 250 nm lateral size, with various thickness of the residual layer, is displayed in Figure 4.5. Whereas the continuous thin film (lower trace in Figure 4.5) was characterized by a stronger absorption peak at ~1400 cm^{-1} (μ_c // *c*) compared to the reference isotropic sample, the imprinted film with no residual layer (upper trace in Figure 4.5) displays a strongly increased absorption peak at ~1180 cm^{-1} (μ_a // *a*), indicating a more in-plane (parallel to the substrate) orientation of the crystallographic *a* axis. This observation is consistent with our previous electron diffraction work [28], which showed that samples imprinted in full confinement essentially displayed the (200) and (400) reflections, together with a weaker (001) reflection. Hence, it is likely that the imprinted sample corresponds to increased edge-on orientations of the lamellae (*a* and *c* in plane) compared to the reference spin-coated sample. In addition, the crystallinity of the fully imprinted sample is increased by about 10% compared to the continuous film annealed at 125°C.

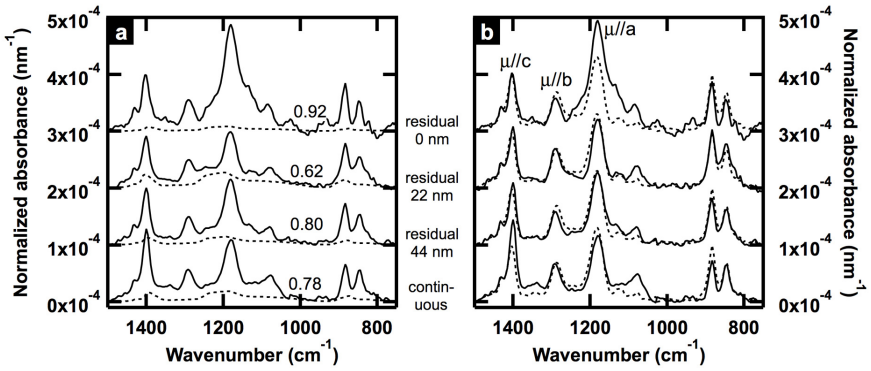

Figure 4.5: (a) Thickness-normalized infrared transmission spectra, corrected for baseline and Si absorption, of P(VDF-TrFE) thin films, imprinted with a mold of square cavities of 250 nm side and varying residual thickness as indicated. The dashed line is the amorphous component; the numbers are the crystallinity. **(b)** Corresponding thickness-normalized infrared spectra of the crystalline component, scaled to unit crystallinity. The dashed line is the spectrum of the reference spin-coated sample. The curves are shifted vertically by integral multiples of 0.0001 nm^{-1} for clarity.

In contrast, imprinted nanopillars with residual layers do not reveal any specific increase of peak intensity compared to the isotropic film, and their crystallinity is similar or even lower to the one of the continuous film. This underlines the determinant role of full confinement in controlling crystal orientation and crystallinity during imprinting, and supports further our findings that showed the importance of nanoimprinting in controlling the local crystallization of polymers [25, 28]. One should however be aware that samples crystallized in conditions of partial confinement exhibit two very different regions, pillars and inter-pillar film, whose morphology was shown to be different by AFM; the infrared

spectrum being the average of these two types of regions, caution should be exercised when discussing them.

The effect of size and shape on crystallization of nanoimprinted P(VDF-TrFE) nanostructures. Once explored the influence of residual layer of imprinted nanostructures on the crystal quality and orientation, we turned our attention to systems which are fully confined in two dimensions (lines), and to imprinted pillars twice larger in lateral size (500 nm side). These samples will be compared with continuous thin films and fully confined pillars of 250 nm side. Hereafter, the 500x500 nm^2 imprinted square structures are referred to as "big pillars" to differentiate them from the previously discussed 250x250 nm^2 pillars which will be referred to as "small pillars". The geometric parameters of the big square mold are the following : p=630 nm, l=500 nm and h=140 nm. With an initial film thickness of 95 nm, full confinement is thus achieved for big pillars.

Figures 4.6a-c shows typical AFM images of imprinted big pillars. It is evident in both height and phase images of Figures 4.6a-c that there is no residual layer between the big pillars after embossing. This is a direct confirmation of a fully confined system. However, on the topmost part of the pillars, randomly oriented and longer crystalline lamellae are observed in Figures 4.6b and c.

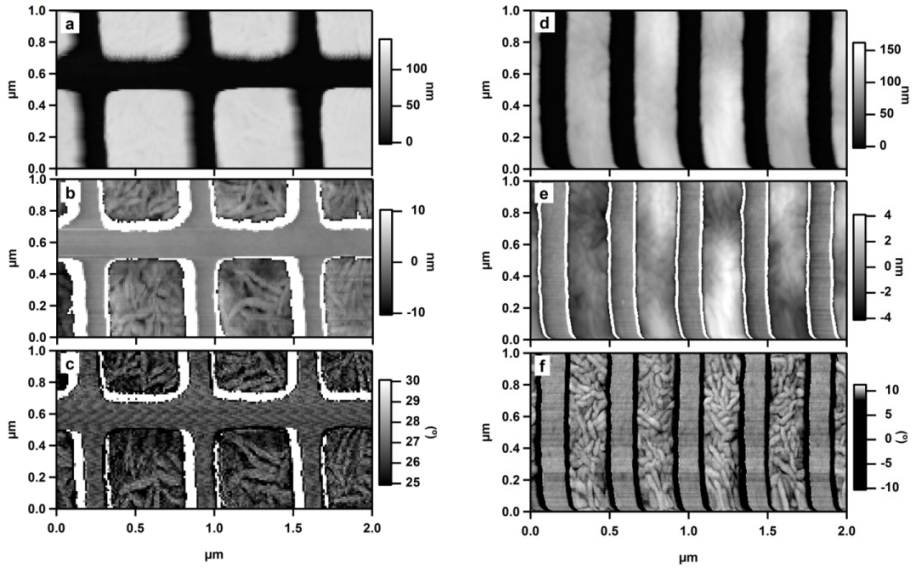

Figure 4.6: AFM morphology of imprinted P(VDF-TrFE) nanostructures of larger size. **(a-c)** AFM images of an array of fully confined nanoimprinted pillars of 500 nm side. **(a)** Height, **(b)** a combined height image of the topmost and bottom part of the nanoimprinted structures revealing long crystal lamellae on the topmost part and **(c)** phase image. **(d-f)** AFM images of nanoimprinted lines in full confinement regime. **(d)** Height, **(e)** a combined height image of the topmost and the bottom part of nanopatterns containing shorter and wider lamellae on the topmost part and **(f)** phase image, showing the lamellae more clearly.

The length distribution of the 50 crystalline lamellae is plotted in Figure 4.3. For imprinted big pillars the average length of the lamellae (298 nm by number; 312 nm by surface) is close to the one of the continuous thin film, and the length of the crystal lamellae is widely distributed from 180 nm to 400 nm. This is in

contrast to imprinted small pillars for which the average length of the crystal lamellae (75 nm) was not only shorter than for bigger squares but showed also less variation of length. Obviously, here crystal nucleation is not severely affected by the splitting of the melt, which is logical since the lateral size of the cavities is well above the average lamellar length obtained in continuous films. Hence, regarding nucleation, the very notion of confinement appears to be relative to the natural, unperturbed size of the crystalline lamellae.

Line molds of period 400 nm and line width 200 nm were also fabricated to make fully confined imprinted lines. Like the square cavities when the initial film thickness *d* is much smaller than the protrusion height *h*, fully confined line patterns could be transferred from the mold. AFM Figure 4.6d-f shows that almost no polymer is left in the regions between the protrusions of the print mold and the substrate, because the initial 95 nm film thickness was much smaller than the 200 nm height of the trenches. AFM height and phase images of Figure 4.6e and f show crystalline lamellae that grow mostly edge-on at the top of the line patterns. The average length of the lamellae of these samples is 127 nm by number (139 nm by surface) and the lengths are less distributed than for continuous thin films. Here, it is important to note that the average size of the lamellae of the line patterns falls between the one of fully confined small squares and the one of fully confined big squares or continuous thin films.

The crystallographic orientation of imprinted big pillars and lines was also studied by FTIR and compared with imprinted small pillars and annealed continuous thin films (Figure 4.7). Neither imprinted lines nor big pillars show any significant difference in the intensities of the absorption peaks, compared to the reference spin-coated film; in addition, their crystallinity of ~80% is comparable to the one of the annealed continuous thin film. This implies that imprinting using big square cavities ($(500\ nm)^2$) and lines (2D confinement)

does not result in increased preferential orientation of specific crystallographic axes with respect to the substrate. Actually, imprinting with large cavities can be essentially considered as shaping the film with little beneficial effect on orientation or nucleation. This underlines the vital role of lateral size and shape of the cavities on controlling the crystal orientation of the P(VDF-TrFE) during embossing process.

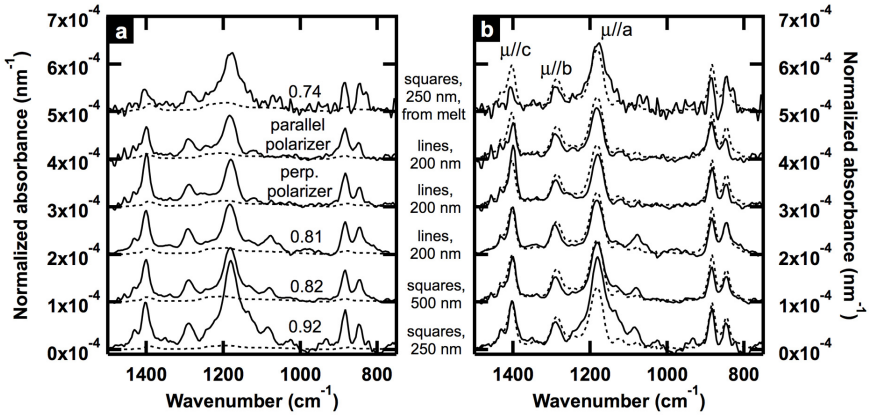

Figure 4.7: (a) Thickness-normalized infrared transmission spectra, corrected for baseline and Si absorption, of P(VDF-TrFE) thin films, with molds of cavities of varying size and shape, as indicated. All samples were imprinted in the paraelectric phase at 125°C, except the topmost sample which was imprinted in the melt at 160°C. The dashed line is the amorphous component; the numbers are the crystallinity. Two spectra of the line-imprinted samples were obtained with a polarizer placed in the beam, either parallel or perpendicular to the direction of the imprinted lines. **(b)** Corresponding thickness-normalized infrared spectra of the crystalline component, scaled to unit crystallinity. The dashed line is the spectrum of the reference spin-coated sample. The curves are shifted vertically by integral multiples of 0.0001 nm^{-1} for clarity.

FTIR was used to investigate further whether the crystals show or not any preferential orientation in the direction of the imprinted lines as the AFM images (Figures 4.6e and f) seemed to suggest. For this, we have used polarized IR to fix the polarization direction of the electric field. The external polarizer was aligned either parallel or perpendicular to the long axis of the lines. The three upper traces in Figure 4.7 shows FTIR absorption peaks of imprinted lines with the IR beam polarized parallel to the direction of the line, perpendicular to the lines, and without polarizer. It is obvious that the FTIR absorption peak at ~1400cm^{-1} (μ_c // *c*) is stronger when the polarizer is perpendicular to the lines, which means that the *c* (chain) axis tends to be perpendicular to the lines. As expected, the IR absorption peaks of imprinted lines without polarizer have intensities between those polarized in the two directions. Since the *c* axis is perpendicular to the basal faces of the crystal, the lamellae should thus on average be more oriented in the direction of the lines. This preferential orientation is due to the influence of topographically-patterned amorphous surfaces guiding the crystal growth in a specific direction, a phenomenon called graphoepitaxy [38]. In our specific case, the presence of rough silicon line grooves helped to guide the crystalline lamellae in the direction of the grooves. However, this effect is far from being perfect, as can easily be realized from the AFM pictures of Figure 4.6, which is not surprising considering the relatively short length of the lamellae compared to the width of the grooves. Accordingly, the dichroic ratio measured from the IR data, $(A_1\text{-}A_2)/(A_1\text{-}A_2)$ where A_1 and A_2 are the peak absorbances at ~1400 cm^{-1} in the presence of the perpendicular and parallel polarizer, respectively, is only ca. 0.25, while it should be 0 and 1 for perfectly random and perfectly oriented samples, respectively.

The effect of imprinting temperature. Thermal annealing of P(VDF-TrFE) films is essential to control the molecular structure as well as the chain

orientation [37], as was shown above. Hence, the imprinting temperature should be crucial as well in determining the final microstructure and electrical performance of the nanostructures. We thus performed FTIR in transmission mode on samples that were imprinted in full confinement either above the melting temperature, or in the paraelectric phase. Fully confined nanopillars of 250 nm lateral dimension imprinted at 125 and 160°C for 10 min are compared in Figure 4.7. Interestingly, the nanoimprinting process exacerbates the trends seen on the continuous thin films. The film imprinted from the melt has a very low absorption peak at 1400 cm^{-1} (μ_c // *c*), indicating that the chain axis is now almost fully perpendicular to the substrate; hence, the trend seen on the continuous films is amplified upon imprinting, leading to a much better alignment of the crystallographic *c* axis corresponding to flat-on crystals (a setting unfavorable for most applications). In addition, the slightly higher intensity at 1180 cm^{-1} (μ_a // *a*) compared to the reference spin-coated film annealed at 125°C implies that the crystallographic *a* axis also tends to orient itself parallel to the substrate. As for the sample imprinted at 125°C, we already noted the preferential orientation of the *a* axis parallel to the substrate, whereas the *c* axis absorption remains strong, which corresponds to an edge-on setting of the crystalline lamellae. These FTIR studies thus underline the importance of controlling the thermal treatment during nanoimprint lithography as it results in entirely different crystalline orientations and therefore, as will be shown shortly, ferroelectric properties.

4.4.2 Nanoscale ferroelectric properties

Piezoresponse force microscopy (PFM) was then used to investigate the impact of the nanoprocessing parameters on the ferroelectric properties of the samples. The coercive field (E_c) of the nanostructured P(VDF-TrFE) can easily be

accessed from PFM phase piezoresponse hysteresis loops (PHLs) [39, 40]. Figures 4.8a-d shows PFM-phase PHLs of imprinted nanopillars and continuous thin films as a function of applied electric field.

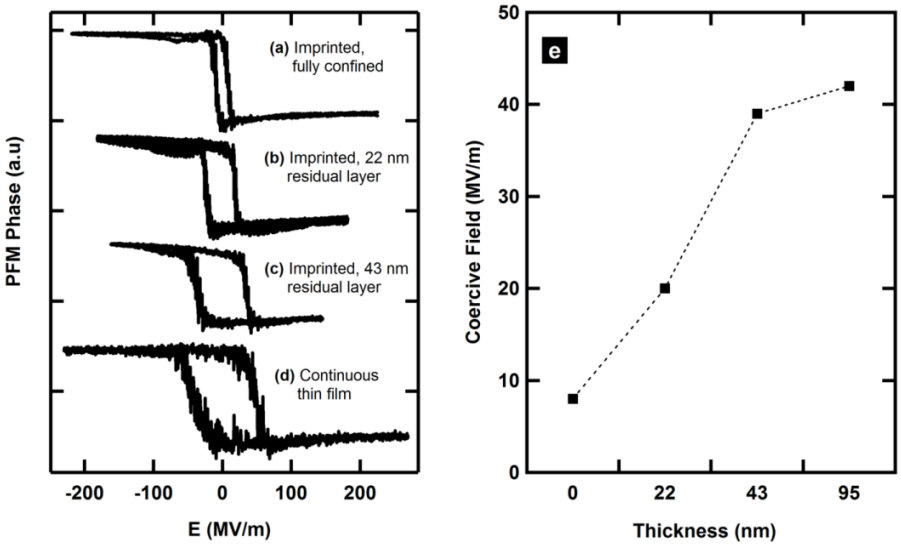

Figure 4.8: PFM-phase piezoresponse hysteresis loops (PHLs) of **(a)** an array of fully confined nanopillars of 250 nm side, **(b)** of a similarly imprinted array but with a 22 nm thick residual layer, **(c)** idem but with 43 nm thick residual layer, **(d)** of a continuous ultrathin film and **(e)** the coercive field of the aforementioned samples as a function of the thickness of the residual layer or the thickness of the continuous thin film (95 nm). The loops were shifted laterally to center them on zero, due to slight experimental shifts resulting from built-in voltage or charging effects.

For imprinted samples, we made sure that the conductive AFM tip was centered on top of the pillars. It should be noted that a series of PHLs were first taken

while sweeping the voltage to increasing values; it was found that maximal voltages of ± 20 V were high enough to switch all the dipole moments of all the samples during a sweep (saturation). Interestingly, the coercive field of imprinted pillars of 250 nm side with 43 nm thick residual layer (~39 $MV.m^{-1}$) is almost the same as the one of the annealed 95 nm thick continuous thin films (~42 $MV.m^{-1}$). However, 100 nm thick fully confined pillars of 250 nm side have the lowest coercive field (~8 $MV.m^{-1}$) of all the samples, which is smaller than the E_c of continuous thin films by up to a factor of five. The E_c of an imprinted sample with 22 nm thick residual layer is between the imprinted sample with 43 nm thick residual layer and the one of fully confined nanopillars. The E_c of all the different samples as a function of the thickness of the residual layer or sample thickness (for the continuous thin film) is plotted in Figure 4.8e. It is obvious from Figure 4.8e that the value of the coercive field increases when the thickness of the residual film increases, demonstrating clearly the importance of full confinement to make the switching of the dipole moments easier.

The ferroelectric properties of imprinted arrays of pillars with different lateral sizes and shape (lines) were also inspected by PFM phase PHLs (Figure 4.9). The coercive field of 130 nm thick imprinted pillars of 500 nm lateral side is ~39 $MV.m^{-1}$, a value close to the E_c of continuous thin films (~42 $MV.m^{-1}$). Interestingly, the ~ 20 $MV.m^{-1}$ coercive field of 200 nm thick confined line patterns is much lower than the one of a continuous thin film but still higher than three-dimensionally confined $(250\ nm)^2$ pillars (Figure 4.9).

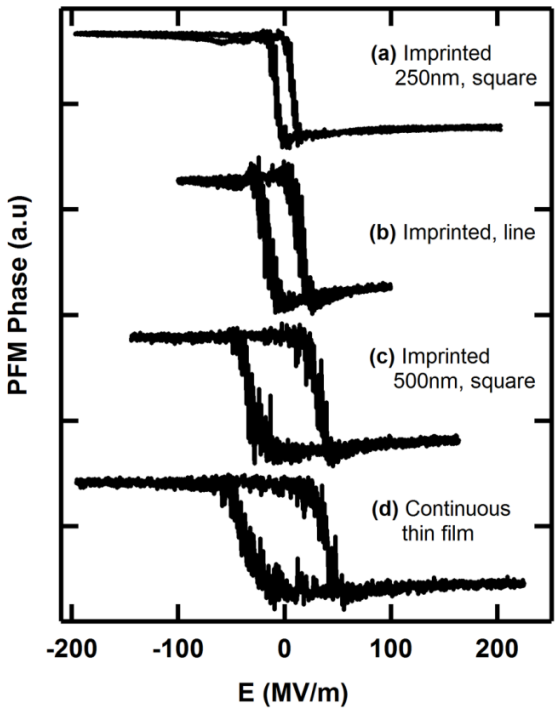

Figure 4.9: PFM-phase PHLs of **(a)** an array of fully confined nanopillars of 250 nm lateral side, **(b)** of an array of fully comfined imprinted lines, **(c)** an array of fully confined nanopillars of 500 nm lateral side and **(d)** of a 95 nm thick continuous thin film.

To complement the PHL results, the polarization switching behavior of the different samples was also studied by PFM imaging. In this mode, one measures the mechanical vibration of a conducting AFM tip in contact with the sample. An alternating electric potential of small amplitude is applied between the tip and bottom electrode, resulting in a periodic sample deformation due to the converse piezoelectric effect. The amplitude and phase of the mechanical

vibration are recorded by monitoring the motion of the tip, providing images which give information about the magnitude of the local polarization and its direction, respectively [39]. In order to observe the switching by PFM imaging, a 20 x 20 μm^2 square area was initially poled by applying a -30 V DC bias to the bottom electrode resulting in a downward pointing dipole moment. Then, small squares of 4 x 4 μm^2 were poled by applying sequentially to the bottom electrode positive DC voltages from +5 V to +30 V with an increment of 5 V. This resulted in partial upward flipping of the dipole moment. Finally, PFM images were recorded again on the 20 x 20 μm^2 square area at 0 V DC, revealing places where the dipole moment was flipped upwards. Typical PFM amplitude and phase shift images of P(VDF-TrFE) imprinted nanostructures poled using the above conditions are shown in Figure 4.10. The clear color contrast between the negatively-poled white background (polarization down) and the small dark squares poled by positive voltage (polarization up) is evident in the PFM phase image (Figure 4.10b) when the positive voltage is large enough. Qualitatively, when the reverse bias is +5 V and +10 V, the color contrast is very weak, indicating that the dipole moments are not fully switched (Figure 4.10b). However, when a positive reverse bias $\geq$15 V is applied, all the small squares are fully dark because all the dipoles are completely switched (180° rotation of the polar CF_2 unit).

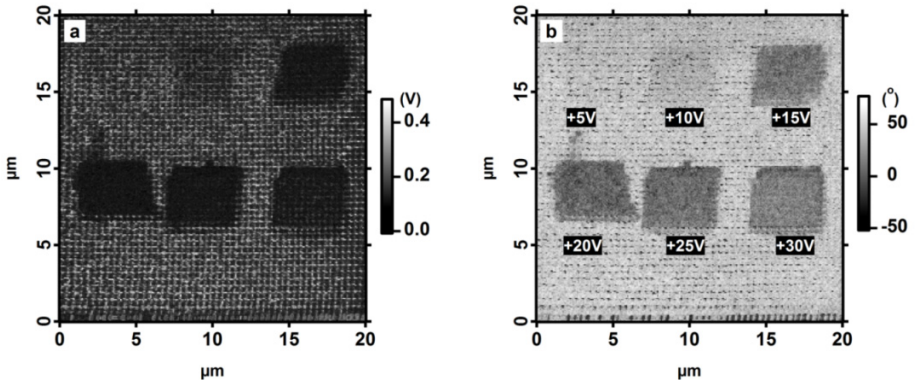

Figure 4.10: (a) PFM piezoresponse amplitude and **(b)** piezoresponse phase images of an array of nanopillars of 250 nm side, with 22 nm thick residual layers. In both images the background was polarized initially with a negative DC voltage of -30 V, and the smaller dark square areas were polarized with increasing positive DC voltages from +5 V to +30 V as shown in **(b)**. Both PFM images are recorded with a 0 V DC voltage.

To quantitatively compare our different samples, we define the "phase-contrast" $C = (A^{+}\cos\phi^{+} - A^{-}\cos\phi^{-})$, with A the PFM amplitude and ϕ its phase, and where the superscripts + and - indicate that the values refer to an average performed over regions poled positively or negatively, respectively. The values of C, which are characteristic for the switching of the polarization, were interpolated and are plotted as a function of the switching electric field in Figures 11a and b.

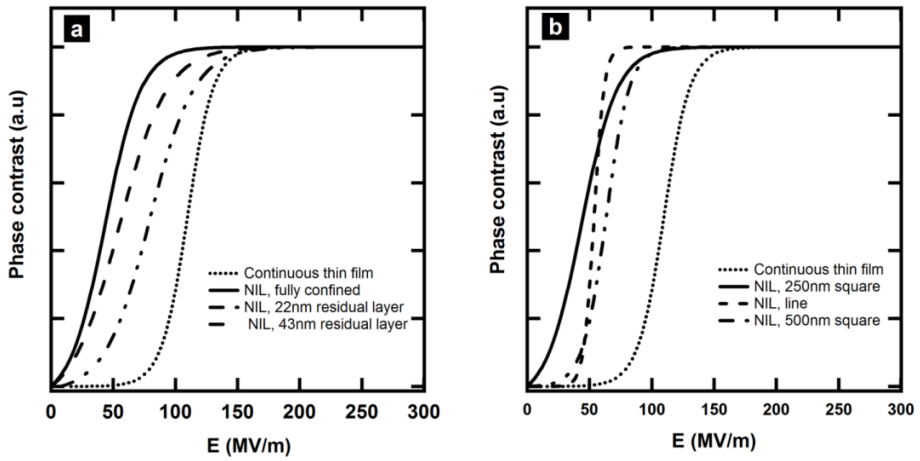

Figure 4.11: (a) PFM phase contrast vs the switching electric field (a) of annealed continuous ultrathin films (dotted line), of an array of fully confined nanopillars of 250 nm side (solid line), of an array of nanopillars of 250 nm side with 22 nm thick residual layer (broken dotted line), and with 43 nm thick residual layer (broken line). **(b)** PFM phase contrast vs the switching electric field of an annealed continuous thin film (dotted line), of an array of fully confined nanopillars of 250 nm side (solid line), of an array of fully confined nanopillars of 500 nm side (broken dotted line), and of imprinted lines (broken line).

Contrarily to the case of PHLs, this parameter is obtained from averages performed over regions containing many nanopillars. As shown in Figure 4.11a, the switching curve of an array of fully confined nanopillars of 250 nm side reaches its saturation plateau at a lower electric field than continuous thin films. Specifically, full confinement of the nanopillars decreases the half-reversal field from 110 $MV.m^{-1}$ for the continuous thin film to 55 $MV.m^{-1}$. This is in

agreement with the observation from PHLs that fully confined nanopillars have a lower coercive field. These lower switching and coercive field values enable easy writing and reading of information on ferroelectric memories.

The switching curves of partially confined nanopillars rest intermediate between fully confined and continuous thin film samples. However, one should be aware that the electric field is heterogeneous over the P(VDF-TrFE) sample, because the thickness of the polymer varies from 22 or 43 nm (over the residual films) to 122 or 143 nm (over the nanopillars). As a result, the electric field which was calculated from the applied voltage using only the thickness of the nanodots is not an exact value over the whole sample, and might actually be quite larger. Hence, the switching curves of these samples having residual layers should only be taken as qualitative.

The polarization switching of imprinted samples of different size and shape was also studied by PFM imaging. Figure 4.11b shows that imprinted pillars of (500 nm)^2 footprint have only a slightly higher half-reversal field (63 MV.m^{-1}) than (250 nm)^2 imprinted squares (55 MV.m^{-1}). The half-reversal field of imprinted lines is also significantly lower (54 MV.m^{-1}). These results are thus not in complete agreement with the PFM phase PHLs, which we ascribe to the heterogeneity of the field over these complex nanostructures. This problem of heterogeneity does however not affect the PHLs, which were performed in the center of the nanopillars and will therefore be used for further discussion.

4.4.1 Correlation between ferroelectric properties and structure

Previously, we had already shown that nanoimprinting could decrease the coercive field E_c of P(VDF-TrFE) significantly [28]; here we have investigated the effect of the remaining residual layer, cavity size and shape, and imprinting temperature, on the structure and electrical properties of the nanostructures. In this section, we attempt to correlate in more detail structure and coercive field. The coercive field reflects how easy the dipoles and ferroelectric domains can be switched, and it should thus depend on several structural factors, including, but not limited to, crystal and dipole orientation, inter-chain distance, domain size, and inter-domain interactions or coupling. It is thus unlikely that a single structural factor would be able to explain all our results.

A first factor to consider is the relative orientation of the dipole moments (aligned along the *b* axis) and of the axis of rotation of the dipole moments (the chain *c* axis) with respect to the vertically-applied electric field. If the *c* axis is tilted by an angle θ away from the vertical electric field, while the *b* axis is rotated about *c* by an angle ϕ away from the plane containing the *c* axis and the electric field, the potential energy of the dipole in the field is $U_d = E.m.\sin\theta.\cos\phi$, where E is the amplitude of the external electric field, and m the one of the molecular dipole moment. If we accept that the rotation of the dipole moment about the chain axis requires to reach a threshold energy U_T, corresponding to energy barriers in the crystal, the coercive field, which measures the force required to start the dipole rotation process, is proportional to $U_T/(m.\sin\theta.\cos\phi)$. A sample with its *a* and *c* axes perfectly in the plane of the substrate would have ϕ=0 and θ=90°, corresponding to the lower possible value

of switching field. A sample with its *c* axis perfectly vertical would have θ=0° and a theoretically infinite coercive field. In agreement with this, the sample that was imprinted above the melting temperature, which precisely has a strongly vertical *c* axis, did not show hysteresis loops when probed by PFM (Appendix, Figure B2). The sample imprinted in full confinement in the paraelectric phase at 125°C has its *a* axis strongly in-plane, implying ϕ=0. This again is in favor of lower coercive fields, the more so that the *c* axis itself will be more in-plane, in agreement with the observed low E_c. Within this very simple model, it becomes then easy to understand why partially confined nanopillars and continuous films have a higher E_c, which is due in part to the presence of more mixed polymer chain orientations, leading to an average weaker interaction between the applied electric field and the more randomly oriented crystals.

However, other factors also certainly play a role, as testified by the fact that samples having similar orientations as probed by FTIR do not have the same coercive field. This is for instance the case for the big pillars and the lines imprinted in full confinement, and the smaller pillars imprinted in partial confinement. We note however that these samples, although being of similar crystallinity, objectively differ in the average length of their crystalline lamellae, and that the general trend is for samples with shorter lamellae also to have lower coercive fields. It might thus be that the nucleation of ferroelectric domains is favored by the presence of crystal surfaces, acting as nucleation centers for dipole switching. This remains hypothetical, since the two observations might simply not directly depend on each other but depend instead on another, still hidden parameter. Nevertheless, this demonstrates clearly the need to decrease the lateral size of confined nanostructures for optimum structure and therefore ferroelectric properties.

4.5 Conclusions

We have demonstrated that by using nanoimprint lithography (NIL) a variety of nanostructured patterns can be transferred from a hard mold to ferroelectric P(VDF-TrFE) by imprinting in its paraelectric phase below the melting temperature. When the sample is imprinted in conditions leading to complete confinement, in cavities of size lower than the natural lamellar length observed in a continuous thin film, we observed a strong preferential orientation of the crystallographic *a* axis parallel to the Si substrate, and lamellae of significantly reduced length. These changes resulted in a strongly decreased coercive field, and accelerated ferroelectric switching, which we ascribed in part to the improved coupling between the electric field and the properly-oriented dipole moments. When decreasing the confinement either by leaving a residual film connecting the nanopillars, or by increasing the lateral side of the nanopillars above the natural lamellar length, or by using line molds where confinement only exists in one direction, or by using continuous films, the preferential orientation becomes less visible and the lamellar length increase, resulting in increased coercive and (sometimes to a lesser extent) switching fields. Interestingly, it appears that the longer the crystalline lamellae, the higher the coercive field. In addition, we found that if the sample is imprinted in the melt, a flat-on setting of the crystalline lamellae ensues, with a strongly vertical chain axis which is unfavorable for ferroelectric properties probed with a vertical electric field. The same was found for a continuous thin film, but nanoimprinting was found to exacerbate this preferential orientation. These results reveal that nanoprocessing parameters like the degree of geometric confinement and imprinting temperature are crucial in controlling the crystal

orientation and therefore ferroelectric properties. Our work should thus be of importance for the realization of low voltage, all organic flexible memories and devices.

4.6 Acknowledgment

Financial support was provided by the Fund for Research in Engineering and Agriculture (FRIA), the Belgian National Research Foundation (FNRS), the Louvain Foundation (Mécénat Solvay) and the Belgian Federal Science Policy (IAP P7/05). ZH acknowledges financial support from the National Natural Science Foundation of China (Nos. 91027040, 21074084) and the Natural Science Foundation of Jiangsu Province of China (No. BK2010213). The authors would like to thank I. Huynen for discussions on electric field calculations by Comsol.

Chapter 4

Bibliography

1. Evans, P.R., X. Zhu, P. Baxter, M. McMillen, J. McPhillips, F.D. Morrison, J.F. Scott, R.J. Pollard, R.M. Bowman, and J.M. Gregg, *Toward Self-Assembled Ferroelectric Random Access Memories: Hard-Wired Switching Capacitor Arrays with Almost Tb/in.2 Densities.* Nano Letters, **2007**. 7, 1134-1137.

2. Das, S. and J. Appenzeller, *FETRAM. An Organic Ferroelectric Material Based Novel Random Access Memory Cell.* Nano Letters, **2011**. 11, 4003-4007.

3. Scott, J.F., *Applications of modern ferroelectrics.* Science, **2007**. 315, 954-9.

4. Furukawa, T., *Ferroelectric properties of vinylidene fluoride copolymers.* Phase Transitions, **1989**. 18, 143-211.

5. Brondijk, J.J., K. Asadi, P.W.M. Blom, and D.M. de Leeuw, *Physics of organic ferroelectric field-effect transistors.* Journal of Polymer Science Part B: Polymer Physics, **2012**. 50, 47-54.

6. Naber, R.C.G., C. Tanase, P.W.M. Blom, G.H. Gelinck, A.W. Marsman, F.J. Touwslager, S. Setayesh, and D.M. de Leeuw, *High-performance solution-processed polymer ferroelectric field-effect transistors.* Nat Mater, **2005**. 4, 243-248.

7. Heremans, P., G.H. Gelinck, R. Müller, K.-J. Baeg, D.-Y. Kim, and Y.-Y. Noh, *Polymer and Organic Nonvolatile Memory Devices†.* Chemistry of Materials, **2010**. 23, 341-358.

8. Naber, R.C.G., K. Asadi, P.W.M. Blom, D.M. de Leeuw, and B. de Boer, *Organic Nonvolatile Memory Devices Based on Ferroelectricity.* Advanced Materials, **2010**. 22, 933-945.

9. Youn Jung, P., B. In-sung, K. Seok Ju, C. Jiyoun, and P. Cheolmin, *Control of thin ferroelectric polymer films for non-volatile memory applications.* Dielectrics and Electrical Insulation, IEEE Transactions on, **2010**. 17, 1135-1163.

10. Yang, Y., J. Ouyang, L. Ma, R.J.H. Tseng, and C.W. Chu, *Electrical Switching and Bistability in Organic/Polymeric Thin Films and Memory Devices.* Advanced Functional Materials, **2006**. 16, 1001-1014.

11. Lovinger, A.J., *Ferroelectric Polymers.* Science, **1983**. 220, 1115-1121.

12. Kepler, R.G. and R.A. Anderson, *Ferroelectric polymers.* Advances in Physics, **1992**. 41, 1-57.

13. Zhang, Q.M., H. Xu, F. Fang, Z.-Y. Cheng, F. Xia, and H. You, *Critical thickness of crystallization and discontinuous change in ferroelectric behavior with thickness in ferroelectric polymer thin films.* Journal of Applied Physics, **2001**. 89, 2613-2616.

14. Guo, D., I. Stolichnov, and N. Setter, *Thermally induced cooperative molecular reorientation and nanoscale polarization switching behaviors*

of ultrathin poly(vinylidene fluoride-trifluoroethylene) films. J Phys Chem B, **2011**. 115, 13455-66.

15. Guo, D. and N. Setter, *Impact of Confinement-Induced Cooperative Molecular Orientation Change on the Ferroelectric Size Effect in Ultrathin P(VDF-TrFE) Films.* Macromolecules, **2013**. 46, 1883-1889.

16. Wu, Y., Q. Gu, G. Ding, F. Tong, Z. Hu, and A.M. Jonas, *Confinement Induced Preferential Orientation of Crystals and Enhancement of Properties in Ferroelectric Polymer Nanowires.* ACS Macro Letters, **2013**. 2, 535-538.

17. Jung, H.J., J. Chang, Y.J. Park, S.J. Kang, B. Lotz, J. Huh, and C. Park, *Shear-Induced Ordering of Ferroelectric Crystals in Spin-Coated Thin Poly(vinylidene fluoride-co-trifluoroethylene) Films.* Macromolecules, **2009**. 42, 4148-4154.

18. Kang, S.J., I. Bae, Y.J. Shin, Y.J. Park, J. Huh, S.-M. Park, H.-C. Kim, and C. Park, *Nonvolatile Polymer Memory with Nanoconfinement of Ferroelectric Crystals.* Nano Letters, **2010**. 11, 138-144.

19. Lutkenhaus, J.L., K. McEnnis, A. Serghei, and T.P. Russell, *Confinement Effects on Crystallization and Curie Transitions of Poly(vinylidene fluoride-co-trifluoroethylene).* Macromolecules, **2010**. 43, 3844-3850.

20. García-Gutiérrez, M.-C., A. Linares, J.J. Hernández, D.R. Rueda, T.A. Ezquerra, P. Poza, and R.J. Davies, *Confinement-Induced One-*

Dimensional Ferroelectric Polymer Arrays. Nano Letters, **2010**. 10, 1472-1476.

21. Hong, C.-C., S.-Y. Huang, J. Shieh, and S.-H. Chen, *Enhanced Piezoelectricity of Nanoimprinted Sub-20 nm Poly(vinylidene fluoride–trifluoroethylene) Copolymer Nanograss.* Macromolecules, **2012**. 45, 1580-1586.

22. Martinez-Tong, D.E., M. Soccio, M.C. Garcia-Gutierrez, A. Nogales, D.R. Rueda, N. Alayo, F. Perez-Murano, and T.A. Ezquerra, *Improving information density in ferroelectric polymer films by using nanoimprinted gratings.* Applied Physics Letters, **2013**. 102, 191601.

23. Kang, S.J., Y.J. Park, J.Y. Hwang, H.J. Jeong, J.S. Lee, K.J. Kim, H.C. Kim, J. Huh, and C. Park, *Localized Pressure-Induced Ferroelectric Pattern Arrays of Semicrystalline Poly(vinylidene fluoride) by Microimprinting.* Advanced Materials, **2007**. 19, 581-586.

24. Zhang, L., S. Ducharme, and J. Li, *Microimprinting and ferroelectric properties of poly(vinylidene fluoride-trifluoroethylene) copolymer films.* Applied Physics Letters, **2007**. 91, 172906.

25. Hu, Z., G. Baralia, V. Bayot, J.-F. Gohy, and A.M. Jonas, *Nanoscale Control of Polymer Crystallization by Nanoimprint Lithography.* Nano Letters, **2005**. 5, 1738-1743.

26. Hu, Z., B. Muls, L. Gence, D.A. Serban, J. Hofkens, S. Melinte, B. Nysten, S. Demoustier-Champagne, and A.M. Jonas, *High-Throughput Fabrication of Organic Nanowire Devices with Preferential Internal*

Alignment and Improved Performance. Nano Letters, **2007**. 7, 3639-3644.

27. Hu, Z. and A.M. Jonas, *Control of crystal orientation in soft nanostructures by nanoimprint lithography.* Soft Matter, **2010**. 6, 21.

28. Hu, Z., M. Tian, B. Nysten, and A.M. Jonas, *Regular arrays of highly ordered ferroelectric polymer nanostructures for non-volatile low-voltage memories.* Nat Mater, **2009**. 8, 62-7.

29. Matsushige, K., S. Imada, and T. Takemura, *Temperature Effect on Ferroelectric Polarization Switching in Poly(vinylidene fluoride).* Polym J, **1981**. 13, 493-499.

30. Kobayashi, M., K. Tashiro, and H. Tadokoro, *Molecular Vibrations of Three Crystal Forms of Poly(vinylidene fluoride).* Macromolecules, **1975**. 8, 158-171.

31. Prabu, A.A., J.S. Lee, K.J. Kim, and H.S. Lee, *Infrared spectroscopic studies on crystallization and Curie transition behavior of ultrathin films of P(VDF/TrFE) (72/28).* Vibrational Spectroscopy, **2006**. 41, 1-13.

32. Cormia, R.L., F.P. Price, and D. Turnbull, *Kinetics of Crystal Nucleation in Polyethylene.* Journal of Chemical Physics, **1962**. 37, 1333-1340.

33. Montenegro, R. and K. Landfester, *Metastable and Stable Morphologies during Crystallization of Alkanes in Miniemulsion Droplets.* Langmuir, **2003**. 19, 5996-6003.

34. Taden, A. and K. Landfester, *Crystallization of Poly(ethylene oxide) Confined in Miniemulsion Droplets.* Macromolecules, **2003**. 36, 4037-4041.

35. Reiter, G., G. Castelein, P. Hoerner, G. Riess, A. Blumen, and J.-U. Sommer, *Nanometer-Scale Surface Patterns with Long-Range Order Created by Crystallization of Diblock Copolymers.* Physical Review Letters, **1999**. 83, 3844-3847.

36. Massa, M.V. and K. Dalnoki-Veress, *Homogeneous Crystallization of Poly(Ethylene Oxide) Confined to Droplets: The Dependence of the Crystal Nucleation Rate on Length Scale and Temperature.* Physical Review Letters, **2004**. 92, 255509.

37. Mao, D., M.A. Quevedo-Lopez, H. Stiegler, B.E. Gnade, and H.N. Alshareef, *Optimization of poly(vinylidene fluoride-trifluoroethylene) films as non-volatile memory for flexible electronics.* Organic Electronics, **2010**. 11, 925-932.

38. Givargizov, E.I., *Graphoepitaxy as an approach to oriented crystallization on amorphous substrates.* Journal of Crystal Growth, **2008**. 310, 1686-1690.

39. Kalinin, S.V., A.N. Morozovska, L.Q. Chen, and B.J. Rodriguez, *Local polarization dynamics in ferroelectric materials.* Reports on Progress in Physics, **2010**. 73, 056502.

40. Soergel, E., *Piezoresponse force microscopy (PFM).* Journal of Physics D: Applied Physics, **2011**. 44, 464003.

Chapter 5

The Curie Transition of Nanoconfined Ferroelectric Poly(Vinylidene Fluoride-*ran*-Trifluoroethylene)

Hailu G. Kassa,[1] Laurianne Nougaret,[1] Ronggang Cai,[1] Alessio Marrani,[2] Bernard Nysten,[1] Zhijun Hu, [3] and Alain M. Jonas[1]

(1) Université catholique de Louvain, Croix du Sud 1/L7.04.02, B1348 Louvain-la-Neuve, Belgium

(2) Solvay Specialty Polymers Italy S.P.A., Viale Lombardia, n° 20, 20021 Bollate (MI), Italy

(3) Soochow University, Suzhou 215006 (China)

This chapter describes the thermal behavior of fully confined P(VDF-TrFE) nanodots fabricated by nanoimprint lithography (NIL). The thermal stability of the nanodots of varying lateral size and height are investigated using piezoresponse force microscopy (PFM) and are compared to the continuous thin films and bulk samples. Results presented in this chapter are submitted for publication. To preserve the clarity of the chapter some selected characterization results are presented at the end of the chapter.

Chapter 5

5.1 Abstract

The Curie transition of nanodots of varying dimensions made by nanoimprinting ferroelectric poly(vinylidene fluoride-*ran*-trifluoroethylene), P(VDF-TrFE), is studied by Piezoresponse Force Microscopy, PFM, and compared to the Curie transition of the bulk material measured by calorimetry. No significant shift of the Curie transition temperature is found for poled nanodots down to a mass as small as *ca.* 560 attograms, corresponding to the volume of a cube of 68 nm side containing *ca.* 1500 chains only. This indicates that the thermal data retention capability of P(VDF-TrFE) is not significantly modified compared to the bulk polymer, which is crucial for the fabrication of reliable non-volatile memories of very high density. These results obtained on nanodots standing in air are contrasted to the ones reported for P(VDF-TrFE) confined by the hard walls of nanocavities.

5.2 Introduction

Ferroelectric polymers such as polyvinylidene fluoride (PVDF) and its copolymers with trifluoroethylene [1] (P(VDF-TrFE)) are gaining renewed attention for the development of next generation low-cost, large-area and flexible organic memory devices, since their permanent polarization can easily be switched by applying an external electric field [2-4]. P(VDF-TrFE) crystallizes predominantly in a phase similar to the polar β phase of PVDF, resulting in a ferroelectric material with a remnant polarization of *ca.* 70 mC/m^2 and a coercive field of *ca.* 50 MV/m [5-7]. P(VDF-TrFE)-based organic

memories have been typically designed as capacitors [8, 9], ferroelectric field-effect transistors [10-12], and blend diodes [13-17].

In order to realize memories of very large storage density, it is required to confine the ferroelectric material in tiny independent nanodots, a process which can be realized by nanoimprint lithography (NIL). We and others have recently reported that, when confining P(VDF-TrFE) in its paraelectric phase into the nanocavities of a NIL mold, preferred crystallographic orientation and eventually a significant decrease of the coercive field of the nanodots ensued [18, 19]. The beneficial structural effect of nanoimprinting was also demonstrated for other semicrystalline polymers [20], including electroluminescent and semiconducting ones [21-23]. Similar structural improvements are also observed when confining P(VDF-TrFE) in the nanochannels of an organosilicate replica of a lamellar block copolymer [24], or when crystallizing P(VDF-TrFE) in the pores of an aluminum oxide membrane [25]. However, the nanodots produced by NIL are interesting for the fabrication of memory devices only inasmuch as the thermal properties of the ferroelectric material are preserved. This is however not granted, since it was reported that nanoconfining ferroelectric polymers can result in thermal properties that may be significantly different from the ones of the bulk [25-29]. Here we demonstrate that, for free-standing nanodots of average lateral size down to *ca.* 68 nm, containing about 1500 polymer chains only, the thermal data retention capability of P(VDF-TrFE) is not significantly modified compared to the bulk polymer.

More specifically, we investigate the Curie transition of nanodots of P(VDF-TrFE), which marks the transition from a ferroelectric crystalline phase to a more disordered paraelectric state accompanied by conformational changes [30]. Data stored in the ferroelectric material are progressively lost when heating the

material in the range of its Curie transition temperature, T_{Cur}. It is known that the Curie transition temperature of P(VDF-TrFE) depends on the size of the ferroelectric domains, which varies with annealing and poling conditions, due to the contribution of depolarization energy in the total free-energy density of the material [31]. In the present study, conditions are selected to pole nanodots in a single ferroelectric domain state (which is the state of interest for a memory device), of which the thermal stability is then studied down to sizes of a few tens of nanometres.

The Curie transition of P(VDF-TrFE) was previously studied in thin and ultrathin films, which are effectively systems confined in one dimension. Jin *et al.*[28] reported a dramatic decrease of T_{Cur} for spin-coated films below 100 nm thickness; this observation was ascribed to a decreased crystallinity and crystal perfection in thinner films, rather than to the intrinsic effect of confinement on ferroelectric properties; different average crystal orientations might also be a further reason for the variations of properties with film thickness [32, 33]. In contrast, ultrathin films obtained by Langmuir-Blodgett deposition were shown to exhibit two Curie transitions [27]. The temperature location of the first one decreased by less than 10°C with film thickness and was attributed to layers in the interior of the film, whereas the second one appeared close to room temperature, and was attributed to surface layers. Similar observations were drawn regarding the Curie transition of nanowires or nanotubes of P(VDF-TrFE) prepared by impregnating with the molten polymer the open porosity of an aluminum oxide membrane (two-dimensional confinement) [25, 29]: the authors again showed the presence of two Curie transitions. The first one (hereafter called the 'bulk' Curie transition) was only very weakly affected by the confinement and was ascribed to the polymer away from the surfaces. The lower second one was broad and found only in the nanopores of *ca.* 15 nm diameter; it

was consistently attributed to the polymer in contact with the alumina walls. Recently, the same authors reported a complete suppression of the 'bulk' Curie transition upon heating, when the porosity of the alumina membrane was filled by dilute solutions of the polymer, resulting in *ca.* 80 attograms only of P(VDF-TrFE) in each pore (presumably not forming a continuous structure) [26]. Only the broad, low temperature transition remained in this case, which might be explained by the strong domination of surface layers in these samples.

It thus appears very likely that P(VDF-TrFE) in contact with solid surfaces exhibits a strongly reduced Curie transition; hence, samples confined in small containers display one or two Curie transitions depending on the relative amount of polymer in contact with surfaces. However, the behavior of nanoconfined P(VDF-TrFE) in the quasi-absence of solid walls remains as yet unknown. Hence, in this paper, we concentrate on nanodots of P(VDF-TrFE) obtained by nanoimprinting and demolding, a process which effectively confines the polymer in the three spatial dimensions and leaves only one side in contact with a solid substrate, then measure the data retention versus temperature by Piezoresponse Force Microscopy (PFM) to evaluate the location of the Curie transition. We show that, down to volumes as small as *ca.* $(68\ \text{nm})^3$, no substantial variation of the Curie transition can be detected for our samples compared to the bulk material, suggesting that P(VDF-TrFE)/gas interfaces are not significantly affecting strongly-confined systems.

5.3 Materials and Methods

The poly(vinylidene fluoride-*ran*-trifluoroethylene) P(VDF-TrFE) sample containing 30 weight % of TrFE units and a weight-average molar mass of *ca.* 230 000, was from Solvay Specialty Polymers. The polymer was dissolved in

cyclohexanone with varying concentrations, and spin-coated at different speeds for 1 min on a highly-doped Si (100) substrate (resistivity 0.3-0.5 Ω.cm). Thin films, of *ca.* 30 - 95 nm starting thickness (ellipsometry-determined values), were nanoimprinted in the paraelectric liquid crystalline phase of P(VDF-TrFE) at 125°C and 60 bars with an Obducat imprinter. Previous work by Balta Calleja *et al.* showed that the hardness of P(VDF-TrFE) is significantly reduced in the paraelectric crystalline state [7]. This reduced hardness allows us to imprint the polymer below the melting temperature, which is required to preserve ferroelectric properties [18]. After 10 min imprinting time, the system was cooled to room temperature, producing arrays of nanodots (Figure 5.1, left). The SiO_2 hard molds with square nanocavities of different dimensions were home-made by electron beam lithography (EBL), followed by lift-off and reactive ion etching procedures. The lateral sizes of the mold cavities ranged from 82 nm to 550 nm, and their depth was either 100 nm or 150 nm. In order to separate the mold easily after imprinting, it was coated with a monolayer of perfluorodecyldimethylchlorosilane deposited from the liquid phase. The topography of the imprinted nanostructures was inspected using atomic force microcopy (AFM) in tapping mode.

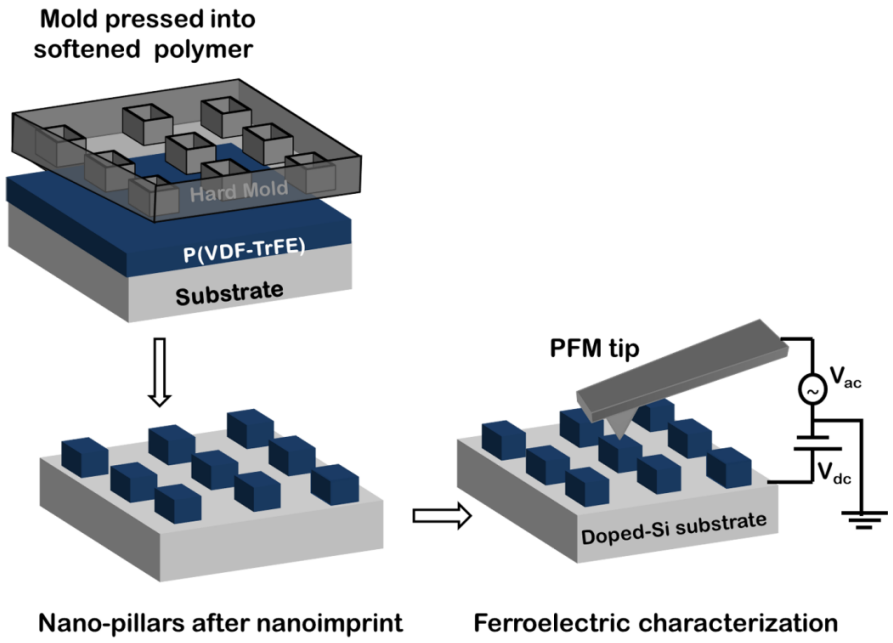

Figure 5.1. Schematic description of the nanopattern fabrication by imprinting the P(VDF-TrFE) in complete confinement (left), followed by local poling and PFM measurement of the resulting nanodots (right).

5.4 Results and Discussion

The initial film thickness of the P(VDF-TrFE) samples was selected in order to ensure nanoimprinting in complete confinement, *i.e.*, in the absence of a continuous polymer film connecting neighbouring cavities of the mold, considering the geometric characteristics of the molds. The expected dot height d after imprint can be obtained as $p^2/l^2.d_o$, where d_o is the initial film thickness, p is the repeat period, and l the lateral side of the (most often square) cavities. Full confinement is achieved when $p^2/l^2.d_o \leq h$, where h is the depth of the square

cavities. For example, our mold of smaller cavity size (in this case, close to circles of *ca.* 82 nm diameter; Figure S5.4, Supplementary Information) has a cavity depth h = 150 nm, and a relative surface of the cavities on the mold close to 0.37; therefore, imprinting films of d_o= ~25-30 nm starting thickness gives rise to isolated dots of *ca.* π $(41)^2$ x 60 = $(68)^3$ nm^3 in size (Figure 5.2).

As shown in the AFM phase image of Figure 5.2 (bottom), each nanodot is totally isolated from the others, with the presence of only a few and discontinuous polymer filaments between the individual pillars. This demonstrates that the topmost part of the hard mold was in contact with the Si substrate during imprinting, as required for complete confinement of the dots. Such conditions of full confinement have been shown before to result in preferential crystallographic orientation, subsequently improving the local ferroelectric property of P(VDF-TrFE) nanodots [18]. During the course of this work, we found clear indications that a change of orientation occurs for the very strongly confined nanodots compared to what we reported before for less strongly confined nanodots [18, 19], with as a consequence an increase of the coercive field; this is detailed in the Supporting Information, Figures S5.6 and S5.7, to keep the focus of the chapter on its main objective.

Using similar imprinting conditions with molds bearing square cavities of different dimensions, and by calibrating the initial film thickness to ensure full confinement, dots of 135 x 135 x 100 nm^3, 250 x 250 x 100 nm^3, and 550 x 550 x 130 nm^3 dimensions were also fabricated (AFM images not shown here). Because the aim of this paper is to investigate the impact of dot size on the Curie transition of imprinted P(VDF-TrFE) samples, special emphasis was given to compute accurate values for the dot dimensions. The lateral sizes were obtained from an analysis of the autocorrelation of SEM images of the molds, because dilation effects by the tip effectively prevented us to use AFM on the imprinted

nanodots for measuring accurately lateral sizes (Supporting Information, Figures S5.1-S5.5). The vertical sizes were obtained from the histograms of pixel height of AFM images of the nanodots.

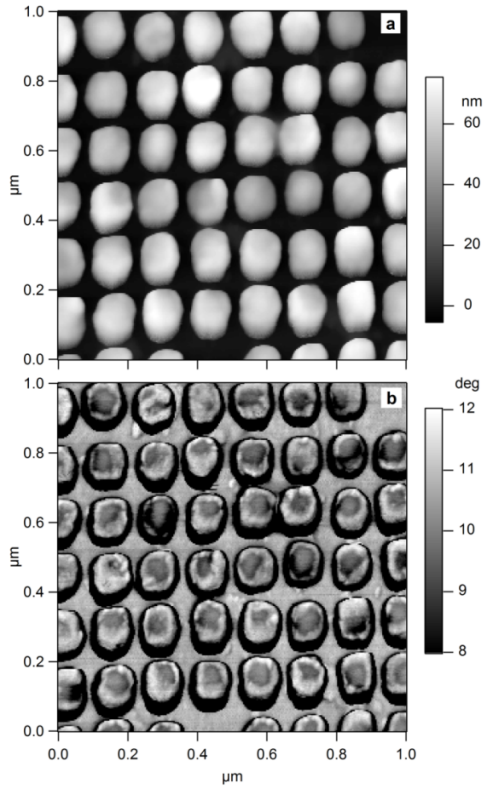

Figure 5.2. AFM tapping mode height (top) and phase (bottom) images for a sample of P(VDF-TrFE) imprinted using the mold with the smaller cavity sizes. The imprinted dots are roughly circular and have an average diameter of 82 nm. The lateral size of the dots in the AFM images appears overestimated due to dilation effects by the AFM tip; an image of the mold is given in Supplementary Information. The average height of the dots computed from the histograms of height of the topography image is 60 nm.

The ferroelectric properties of the samples were determined versus temperature by Piezoresponse Force Microscopy [33-35], PFM (Figure 5.1, right, and Supplementary Information). Because the Curie transition temperature of P(VDF-TrFE) depends on ferroelectric domain size [31], it is important to control this parameter. Large domains can typically be obtained by annealing the samples in the paraelectric phase [31], and/or by poling them with a voltage well above the switching voltage [36]. In our study, we combined the two effects: we imprinted in the paraelectric phase, and we poled the nanodots up- or downwards at room temperature before studying their properties. This gives rise to nanodots uniformly polarized in one direction, effectively corresponding to single domain nanodots as shown in the Supplementary Information (Figure S5.8), which is typically what is needed for a nanodot-based memory.

More precisely, in order to determine the Curie transition temperature, the polarization of the samples was first locally oriented upwards by scanning the PFM tip over an area of 5 x 5 μm^2, using a poling voltage of -10 V. Then, the samples were poled with a positive 10 V voltage over a 2 x 2 μm^2 region written within the negatively-poled square, in order to orient the polarization downwards. Maps of the polarization were then measured in PFM mode for increasing temperatures, applying a sinusoidal voltage $V_{AC} = V_0 \cos(\omega t)$ of small amplitude on the PFM tip. Due to the converse piezoelectric effect, the alternating electric field generates an oscillating deformation of the sample in the direction perpendicular to the electric field, $A(t) = A_{piezo} \cos(\omega t + \phi_{piezo})$, which is detected by the vertical deflection of the cantilever having its tip in contact with the sample. In this way, maps of the PFM amplitude A_{piezo} and of the PFM phase ϕ_{piezo} can be drawn simultaneously.

The PFM amplitude varies moderately depending on the direction of poling, whereas the phase angle is more sensitive. For this reason, only the PFM phase images are used here to study the ferroelectric contrast of nanodots as a function of temperature. Figure 5.3 illustrates a typical measurement of PFM topography and phase images for a sample where regions have been poled up- and downwards. The topography is strongly distorted above the Curie transition, due to the P(VDF-TrFE) being in the softer paraelectric phase, which is of lower mechanical strength (Figure 3, top) [7]. The phase angle maps of Figure 5.3 also show the expected contrast depending on poling direction, with brighter (darker) colors corresponding to upwards (downwards)-pointing polarization.

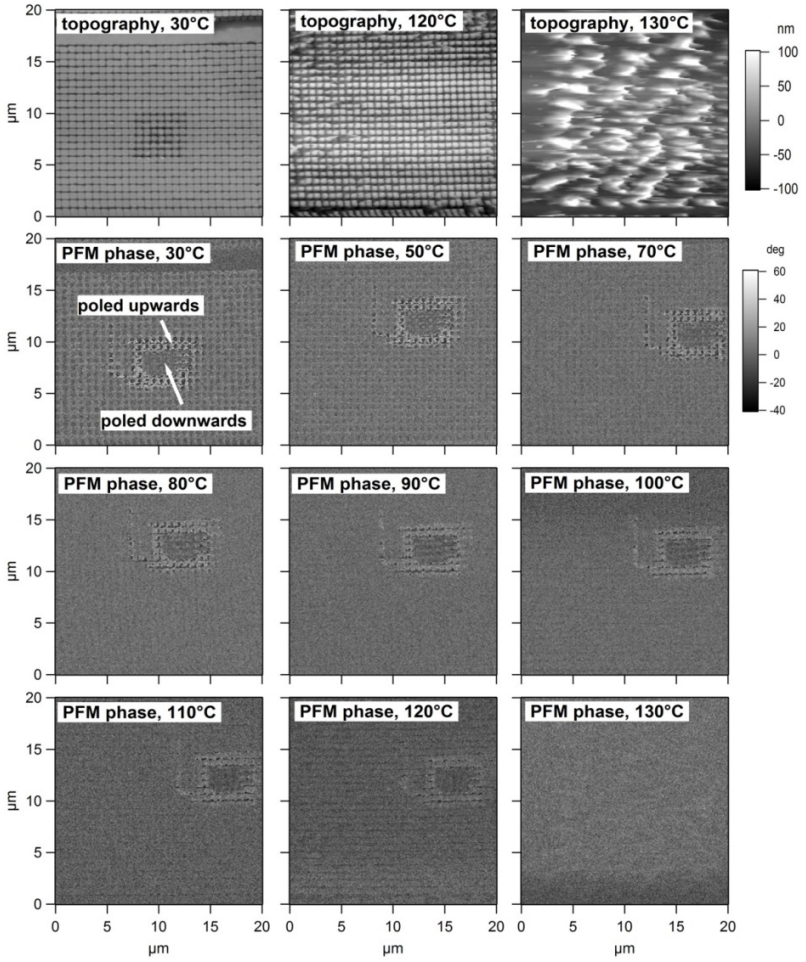

Figure 5.3. PFM topography images (top row) and piezoresponse phase images (three lower rows) of an array of P(VDF-TrFE) dots of 550 nm lateral side, poled at room temperature (20°C) then imaged at increasingly higher temperatures. The regions poled with a negative and positive poling voltages appear as brighter and darker regions, respectively. The temperatures of acquisition are given in each sub-panel. The progressive fading of the PFM phase contrast is clear.

The PFM phase images of Figure 5.3 fade at higher temperature, testifying for the progressive loss of data retention when the sample nears T_{Cur}. In order to quantitatively compare the different samples, we defined the "PFM phase contrast" as the absolute value of the difference of average PFM phase of the dots in the upward- (ϕ^+) and downward-poled (ϕ^-) regions. The average phase is taken from the distributions of pixel phase of the PFM phase images (Figure 5.4). For some samples, the distribution of pixel phase had to be described by the sum of two gaussians, corresponding to the phase over the grooves and over the dots, respectively. For many samples, however, only one gaussian was needed, either because the contrast between grooves and dots was not strong enough, or because the tip did not penetrate deep enough in the grooves due to the large size of the AFM tip. Here, we have used the value of average phase associated with the dots only to obtain quantitative information about the ferroelectric transition of our samples. Of note, theoretically, the phase signal should be either 0 or 180° depending on whether the average dipole moment points down or up, respectively [35]. However, other sources of electromechanical coupling frequently add up in the total signal [34]; as a result the measured phase angles are in the present case between -40 and 60° over the poled regions (Figure 5.3 and 5.4).

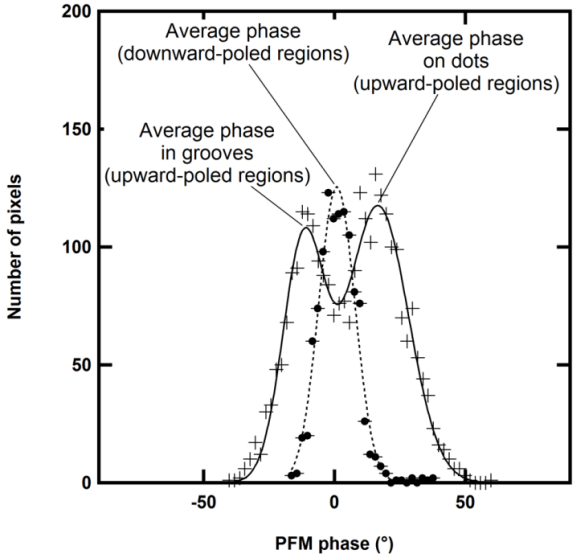

Figure 5.4. Typical distributions of PFM phase for the pixels of a PFM phase image (for dots of 550 nm lateral side, measured at 30°C), illustrating two cases of possible distributions, mono- or bi-modal. The two distributions correspond to regions poled upwards or downwards, as indicated. The difference of average PFM phase over the dots, between the two differently-poled regions, defines the PFM contrast.

The variations of the phase contrast (abs(ϕ^+ - ϕ^-)) of the nanoimprinted dots and continuous thin film samples are reported in Figure 5 (left) versus the temperature T during a stepwise heating scan. The data are compared to the thermogram (10°C/min heating scan) obtained by differential scanning calorimetry (DSC) for a non-poled bulk sample annealed at 125°C after having been cooled from the melt at -10°C/min.

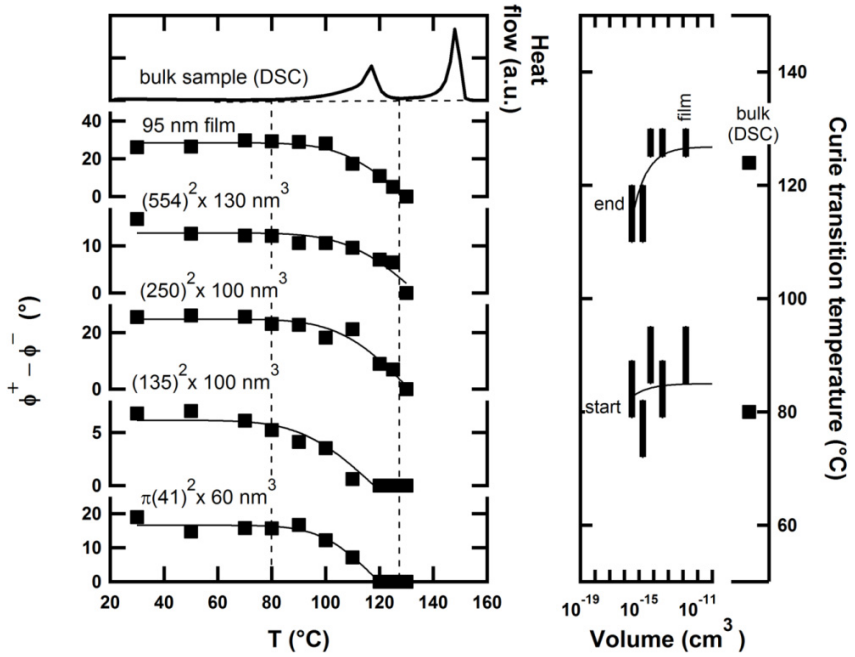

Figure 5.5. (Left) Piezoelectric phase contrast, abs(ϕ^+ - ϕ^-), of P(VDF-TrFE) samples imprinted in nanodots of varying sizes, and of a continuous thin film, determined from PFM maps like the ones shown in Figure 5.3, and compared to (top) the DSC thermogram of the same sample in the bulk annealed at 125°C. The volumes of the dots are indicated in the graph. (Right) The starting and ending temperatures of the loss of PFM contrast as a function of the volume of P(VDF-TrFE) nanodots. The volume for the continuous film sample was fixed arbitrarily to fit in the graph. The squares indicate the start and end of the Curie peak in the DSC thermogram of the bulk sample.

The DSC thermogram indicates that the Curie transition occurs over some temperature interval in the bulk sample. This is due to a distribution of domain quality in the sample, arising from the numerous defects of the polymer morphology, resulting from chemical heterogeneity (regioregularity, comonomer distribution) and from the intrinsic semicrystalline nature of crystalline polymers. Therefore, the ending temperature of the transition is typical for better organized regions, and can thus be taken as a more significant indicator for the Curie transition. For the imprinted samples, the PFM contrast used in the present study is the difference between the average PFM phase on differently-poled regions. For depolarized regions, this difference should be zero. Hence, the phase contrast is proportional to the average surface of the dots which remains polarized; in other words, it should be proportional to the volume of material still polarized. Therefore, its information content is similar to the one provided by DSC, explaining why it varies over a similar range of temperature as the DSC Curie peak. Likewise, the ending temperature of the transition measured by PFM should be taken as a more significant indicator for the Curie transition.

As compared to the Curie transition temperature of P(VDF-TrFE) in the bulk and the one of the continuous thin film, nanoimprinted dots of different sizes are seen to be weakly affected by the confinement, with a decrease of max. 10°C for the most confined sample (*ca.* 82 nm dot diameter and *ca.* 60 nm height) (Figure 5.5). The dots of the most confined sample have a volume corresponding to about 1500 chains only (as computed from the volume, the density assumed to be *ca.* 1.78 g/cm^3, and the average molar mass by weight of the chains). Hence, even a very strong confinement is seen to hardly change significantly the 'bulk' Curie transition. Serghei *et al.* recently showed that the 'bulk' Curie transition was completely suppressed on heating for P(VDF-TrFE) samples deposited from very dilute solutions in Al_2O_3 nanopores [26]. The weight of these samples was

estimated to be *ca.* 80 attograms, which is not orders of magnitude lower than the 560 attograms of our smaller nanodots that do not show any evidence for a disappearance of the 'bulk' Curie transition. It is likely that this is due to the fact that our systems are not in contact with hard walls: the hindrance to chain mobility and dipole switching is thus much smaller in our case of confinement with gas/solid interfaces compared to solid/solid interfaces.

As mentioned in the introduction, previous measurements made on thin films (2D confinement) [27, 28] or systems confined in alumina oxide nanocavities (either in long nanotubes - 1D confinement [25, 29]; or as dilute deposits in cylindrical nanopores [26]) also indicated the apparition of a low temperature Curie transition ascribed to the layers of P(VDF-TrFE) in contact with solid surfaces; reports indicate this transition to be in the [20,80]°C range [25], [20,40]°C range [27], or [-30,20]°C range [26]. Again, we did not note any significant sign for the presence of a second Curie transition in the temperature range of our study (from 30°C up), suggesting that it is either too weak to be detected, or that it simply does not appear for our samples for which 5 out of 6 bounding interfaces are in contact with air. This again points to the strong difference existing between confinement by hard walls, and 'self-confinement'. On the other hand, it must also be stressed that we studied the Curie transition of poled samples, having large domain sizes, whereas the previously reported works were performed on non-poled samples for which the domain size could be much lower [36].

5.5 Conclusion

Summarizing, for our very confined and poled systems where the confinement is essentially performed by fluid (gas) interfaces, the 'bulk' Curie transition of P(VDF-TrFE) is not modified strongly, and the sample preserves essentially the same thermal behaviour as the bulk samples (within 10°C) down to nanodots of *ca.* 560 attograms, corresponding to the volume of a cube of 68 nm side containing *ca.* 1500 chains only. The disappearance of the Curie transition noticed in [26] is thus most probably originating from interactions between the P(VDF-TrFE) and the alumina surfaces, which do not exist in our samples. This indicates the huge influence of interfaces for confined ferroelectric polymers, and demonstrates that ferroelectric properties can be preserved for samples three-dimensionally confined in small cubes of only of few tens of nm in size, which is of direct interest for the fabrication of ferroelectric plastic memories of very high density.

5.6 Supporting Information

5.6.1 Characterization of Nanoimprinting Molds

The dimensions of the cavities of the molds were obtained from scanning electron microscopy (SEM) images. The SEM was calibrated with a reference grid. The autocorrelation images were computed as described previously [37, 38], and analysed to obtain statistically-relevant values. The repeat periods were obtained by taking the average length of the sides of the first unit cell of the autocorrelation function.

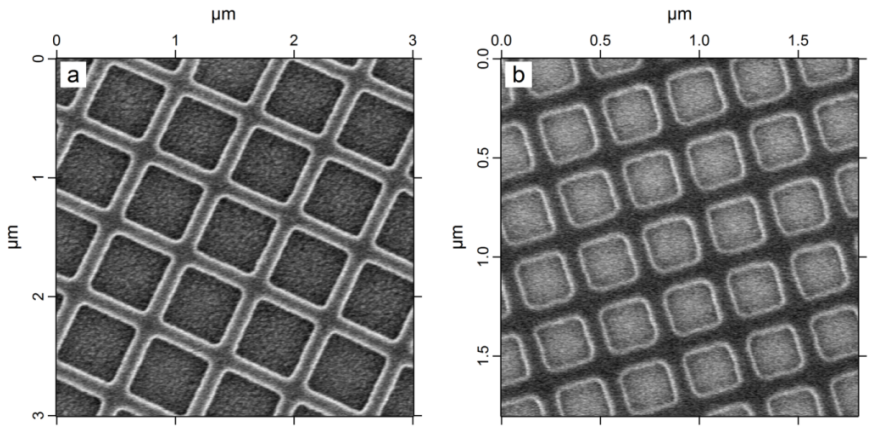

Figure S5.1. SEM image of imprinting SiO_2 hard molds containing square cavities with dimensions (a) ~550 x 550 nm^2 and (b) ~250 x 250 nm^2.

For the two molds of larger hole size with a period of *ca*. 660 nm (Figure S5.1a) and a period of *ca*. 340 nm (Figure S5.1b), the holes appeared as square in shape. Because the emission of secondary electrons is strongly increased at the

edges of the holes, the holes are surrounded by lines of higher intensity, which give rise in the autocorrelation images to strongly-marked correlation lines between the edges of the holes (Figure S5.2). The average length of the sides of the holes was thus obtained from these lines, as shown by the green circles in Figures S5.2a and S5.2b, providing values of 554 nm and 250 nm for the two molds of larger hole size, respectively. This method effectively corresponds to defining the edges of the holes as being located in the middle of the lines of higher emitted intensity in the direct images. A direct evaluation on profiles of intensity from the SEM images gave identical values (within ~2%), although less statistically-relevant since the autocorrelation image concentrates near the origin of space the information of all unit cells taken together.

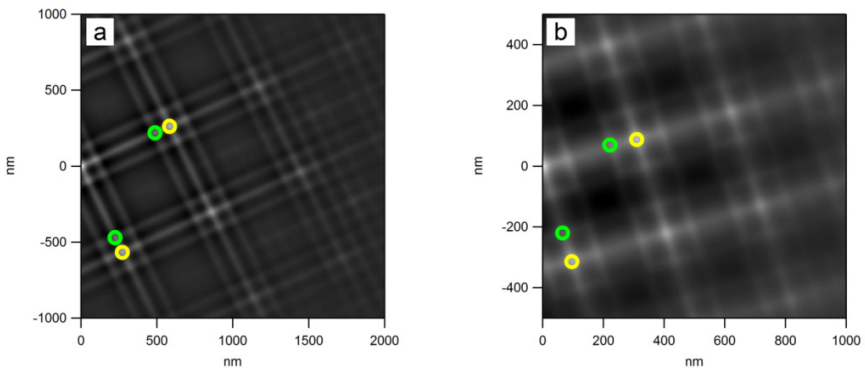

Figure S5.2. Autocorrelation of the SEM images of Figure S5.1 for (a) ~550 x 550 nm^2 and (b) ~250 x 250 nm^2 imprinting SiO_2 molds with square cavities. The green circles give the size of the holes, whereas the period along the two crystallographic axes of the 2D unit cell is indicated by the yellow circles.

The same kind of analysis was used for a third mold of smaller square cavities (Figure S5.3), where 193 and 135 nm were found as the period and size of holes, respectively.

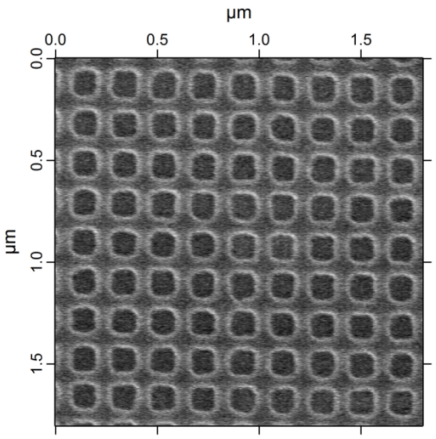

Figure S5.3. SEM image of imprinting SiO2 hard mold consisting of square cavities with a dimension of ~135 x 135 nm^2.

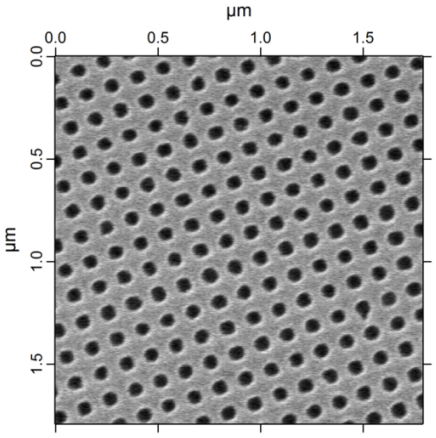

Figure S5.4. SEM image of imprinting SiO_2 hard mold of circular cavities with a surface of π $(41)^2$ nm^2.

Finally, for the mold of even smaller hole size, the shape appears to be more rounded and in many cases close to circular (Figure S5.4). Therefore, the correlation lines between the edges of the holes do not appear anymore in the

autocorrelation image. However, in the diagonal direction of the unit cell, the size of the holes is much lower than the distance between the holes, allowing us to perform a more refined interpretation of the autocorrelation image. We took a profile of the autocorrelation in this direction (green line in Figure S5.5a, and profile in Figure S5.5b), from which the average size of the holes can be obtained as indicated. We found 77 nm and 86 nm, using the profiles from two different images, leading to an average value of 82 nm for the diameter of the circular average hole. Direct measurement of two holes gave 86 nm for the diameter, which is close (but less accurate). In this way, the exact sizes of all mold cavities were determined with good precision.

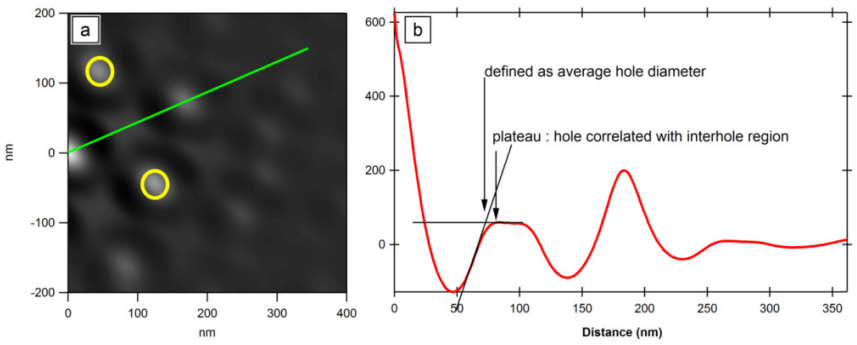

Figure S5.5. (a) Autocorrelation of the SEM image of Fig.S4, for an imprinting mold of approximately circular cavities with a surface of π $(41)^2$ nm^2. The yellow circles indicate the ends of the vectors of the 2D unit cell. (b) Line profile taken along the green line in (a), together with its interpretation.

5.6.2 Characterization of the Crystallographic Orientation after NIL

The crystal orientation of imprinted P(VDF-TrFE) samples was investigated by Fourier-transform infrared microscopy (continuμm microscope from Thermo Scientific) in transmission mode (Figure S5.6). A detailed description about the quantitative analysis of the infrared spectra can be found chapter 4.

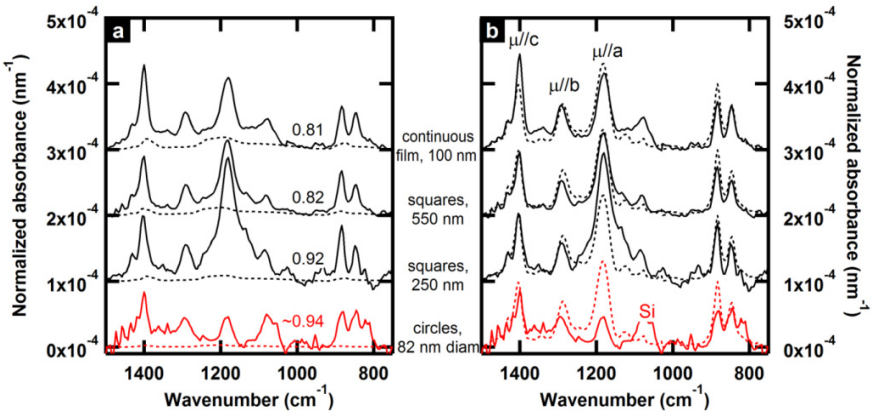

Figure S5.6. (a) Thickness-normalized infrared transmission spectra of P(VDF-TrFE) thin films, imprinted with a mold of square cavities of varying size as indicated. The dashed line is the amorphous component; the numbers are the crystallinity. (b) Corresponding thickness-normalized infrared spectra of the crystalline component, scaled to unit crystallinity. The dashed line is the spectrum of a reference spin-coated sample.

Figure S6 shows that the imprinted dots with a diameter of 82 nm (the red trace) display a reduced absorption peak at ~1180 cm-1 (μ_a // a), indicating a more out

of plane (away from the substrate) orientation of the crystallographic *a* axis compared to the imprinted dots of 250 nm lateral size, and also compared to a continuous film. Clearly, the orientation of the crystals depends in a complex way on the size of the nanodots: whereas the *a* axis tends to align more in the plane of the substrate when going from a continuous film to dots of 250 nm lateral side as reported in chapter 4, the trend is reversed when going to even smaller dot sizes. This is most probably due to the relative influence of surfaces in the alignment process arising during confinement. Complementary experiments would be of interest to obtain a more complete picture; this was not attempted here, considering that the precision on the 82 nm dots remains low, since there is very little material in the beam.

5.6.3 Ferroelectric Characterization

The ferroelectric properties of the samples were determined versus temperature by Piezoresponse Force Microscopy [33-35], PFM, using an Agilent 5500 microscope equipped with a Mac III triple lock-in amplifier (Agilent), and with a hot-stage controlled by a 321 Autotuning Temperature Controller (Lakeshore). The DC bias voltages were applied on the sample substrate and the AC biases were applied to the PFM probe (Si cantilever with 0.02-0.77 N/m nominal bending rigidity, coated with conductive boron-doped diamond, CDT-CONTR from Nanosensors). The samples were first locally poled by scanning a small region using poling voltages of +/-10 V and a scan rate of 0.8 lines/s. Maps of the polarization were then measured by PFM by scanning the sample over the written squares while applying to the PFM tip a sinusoidal voltage $V_{AC} = V_0 \cos(\omega t)$ with $V_0 = 0.5$ V and $\omega \sim 628 \times 10^3$ s^{-1} close to the resonance frequency of the tip when in contact with the sample.

Piezoresponse hysteresis loops (PHLs) were also measured on the samples as described in earlier in chapter 4 (Figure S5.7, left), and used to obtain the value of coercive field (E_c) of the imprinted P(VDF-TrFE) samples as a function of applied electric field (Figure S5.7, right).

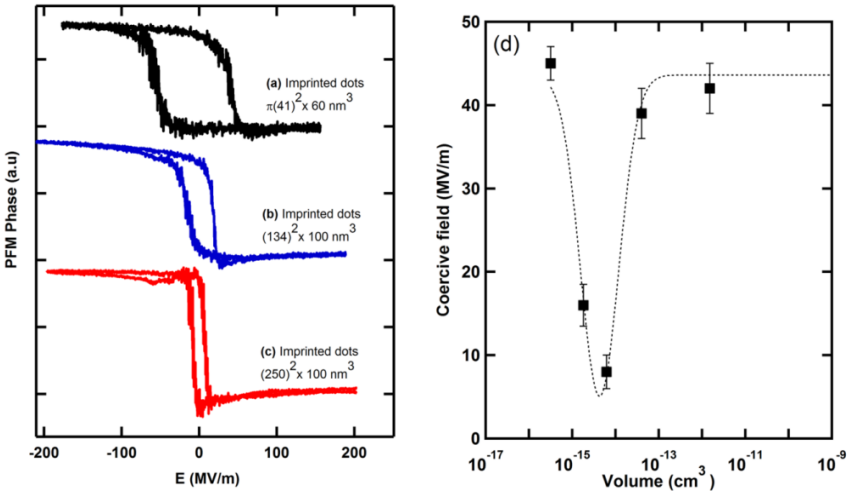

Figure S5.7. PFM-phase PHLs of an array of fully confined nanopillars of 82 nm (a), 134 nm (b), and 250 nm lateral side. (d) The coercive field of these samples versus the volume of P(VDF-TrFE) nanodots.

In the higher range of sizes, we find the expected decrease of coercive field upon increased confinement, as reported earlier in chapter 4 [18] and by us before [19]. However, for the smaller nanodots, the coercive field now increases when the size decreases; this is a range which was not explored in our previous studies. The higher coercive field of imprinted dots of 82 nm in diameter with 60 nm height (~45 $MV.m^{-1}$) compared to the 100 nm thick fully confined dots of 250 nm side (~8 $MV.m^{-1}$), can be correlated to the microstructure of the

corresponding samples. The differently oriented crystals (Figure S5.6), and thus the differently oriented dipole moments (which are aligned perpendicular to the chain axis) of imprinted dots of 82 nm in diameter, apparently lead to an average weaker interaction with the vertically-applied electric field, and as a result to a higher coercive field, close to the one of continuous thin films of P(VDF-TrFE) sample. A detailed discussion about the interaction of the applied electric field with the dipole moment of the ferroelectric polymers can be found in chapter 4 of this thesis. Compared to this previous work, the smaller dots tested in the present work clearly behave differently from what we expected, both as regards crystallographic orientation and coercive field. We note however that we never ventured into such small sizes before; apparently, when decreasing the size of the dots to below 100 nm, a new regime of properties and orientation appears, which was not yet explored until now. Further studies are clearly required to elucidate this new behavior of extremely confined P(VDF-TrFE).

5.6.4 Domain Size of Poled Nanodots

The size of ferroelectric domains was evaluated by PFM at a higher resolution than for the measurement of the loss of contrast with temperature. The samples were poled in the PFM with a 10 V bias applied to the tip, then imaged in PFM mode. Figure S5.8 presents the PFM topography, and the PFM amplitude and phases, for the samples of larger dot size (550 and 250 nm lateral size). The phase is essentially uniform over one dot, confirming that the dots can be considered as single domain after poling. Note that the topography of the 550 nm-side dots shows an irregular top surface, due to the fact that the bottom of the holes of the molds were not in contact with the top of the dots for this specific sample.

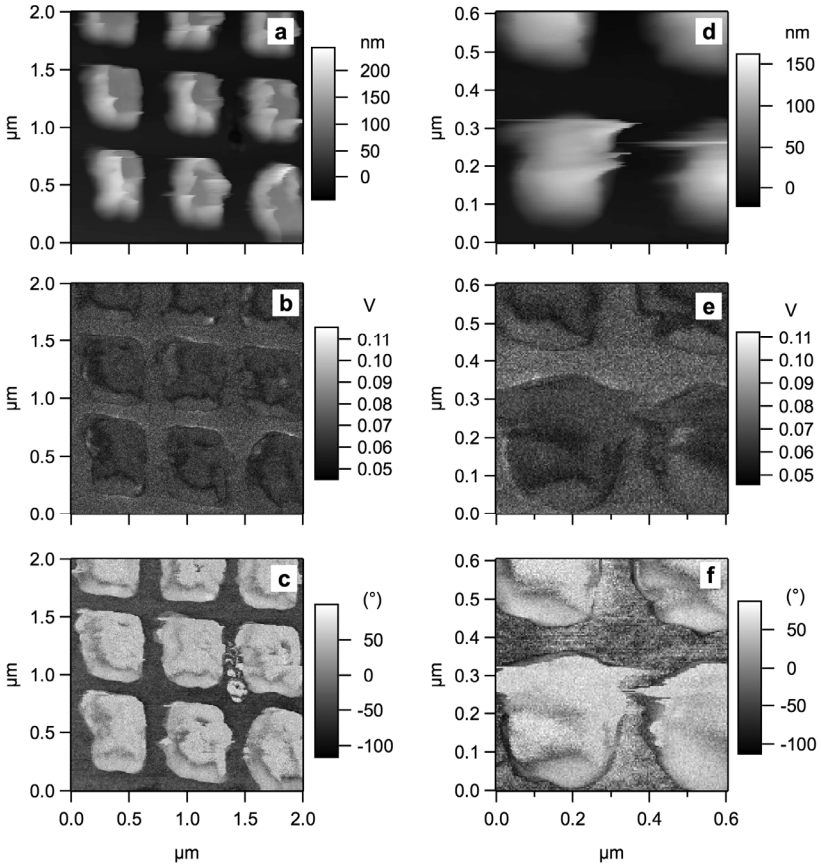

Figure S5.8. PFM topography (a,d), PFM amplitude (b,e) and PFM phase (c,f) of nanodots of 550 nm (a-c) and 250 nm (d-f) lateral size, after poling by 10 V. The phase is uniform over the dots, indicating that the nanodots are essentially single domains after poling.

5.7 Acknowledgments

Financial support was provided by the Fund for Research in Engineering and Agriculture (FRIA), the Belgian National Research Foundation (FNRS), the EU Program FP7/2007-2013 (MOMA, agreement n° 248092), the Belgian Federal Science Policy (IAP P7/05), and the F.R.S.-FNRS.

Chapter 5

Bibliography

1. Lovinger, A.J., *Ferroelectric Polymers.* Science, **1983**. 220, 1115-1121.

2. Naber, R.C.G., K. Asadi, P.W.M. Blom, D.M. de Leeuw, and B. de Boer, *Organic Nonvolatile Memory Devices Based on Ferroelectricity.* Advanced Materials, **2010**. 22, 933-945.

3. Heremans, P., G.H. Gelinck, R. Müller, K.-J. Baeg, D.-Y. Kim, and Y.-Y. Noh, *Polymer and Organic Nonvolatile Memory Devices.* Chemistry of Materials, **2011**. 23, 341-358.

4. Ling, Q.-D., D.-J. Liaw, C. Zhu, D.S.-H. Chan, E.-T. Kang, and K.-G. Neoh, *Polymer electronic memories: Materials, devices and mechanisms.* Progress in Polymer Science, **2008**. 33, 917-978.

5. Kepler, R.G. and R.A. Anderson, *Ferroelectric Polymers.* Advances in Physics, **1992**. 41, 1-57.

6. Furukawa, T., *Ferroelectric Properties of Vinylidene Fluoride Copolymers.* Phase Transitions, **1989**. 18, 143-211.

7. Baltá Calleja, F.J., A.G. Arche, T.A. Ezquerra, C.S. Cruz, F. Batallán, B. Frick, and E.L. Cabarcos, *Structure and Properties of Ferroelectric Copolymers of Poly(vinylidene fluoride).* Advances in Polymer Science, **1993**. 108, 1-48.

8. Khan, M.A., U.S. Bhansali, and H.N. Alshareef, *Fabrication and Characterization of All-Polymer, Transparent Ferroelectric Capacitors on Flexible Substrates.* Organic Electronics, **2011**. 12, 2225-2229.

9. Tripathi, A.K., A.J.J.M. van Breemen, J. Shen, Q. Gao, M.G. Ivan, K. Reimann, E.R. Meinders, and G.H. Gelinck, *Multilevel Information Storage in Ferroelectric Polymer Memories.* Advanced Materials, **2011**. 23, 4146-4151.

10. Naber, R.C.G., C. Tanase, P.W.M. Blom, G.H. Gelinck, A.W. Marsman, F.J. Touwslager, S. Setayesh, and D.M. de Leeuw, *High-Performance Solution-Processed Polymer Ferroelectric Field-Effect Transistors.* Nature Materials **2005**. 4, 243-248.

11. Jung, S.-W., J.-K. Lee, Y.S. Kim, S.-M. Yoon, I.-K. You, B.-G. Yu, and Y.-Y. Noh, *Top-Gate Ferroelectric Thin-Film-Transistors with P(VDF-TrFE) Copolymer.* Current Applied Physics, **2010**. 10, e58-e61.

12. Lee, K.H., G. Lee, L. Kimoon, O. Min Suk, and I. Seongil, *Flexible Low Voltage Nonvolatile Memory Transistors with Pentacene Channel and Ferroelectric Polymer.* Applied Physics Letters, **2009**. 94, 093304-093304-3.

13. Asadi, K., T.G. de Boer, P.W.M. Blom, and D.M. de Leeuw, *Tunable Injection Barrier in Organic Resistive Switches Based on Phase-Separated Ferroelectric–Semiconductor Blends.* Advanced Functional Materials, **2009**. 19, 3173-3178.

14. Asadi, K., P.W.M. Blom, and D.M. de Leeuw, *The MEMOLED: Active Addressing with Passive Driving.* Advanced Materials, **2011**. 23, 865-868.

15. Asadi, K., D.M. de Leeuw, B. de Boer, and P.W.M. Blom, *Organic Non-Volatile Memories from Ferroelectric Phase-Separated Blends.* Nature Materials **2008**. 7, 547-550.

16. Asadi, K., M. Li, P.W.M. Blom, M. Kemerink, and D.M. de Leeuw, *Organic Ferroelectric Opto-Electronic Memories.* Materials Today, **2011**. 14, 592-599.

17. Nougaret, L., H.G. Kassa, R. Cai, T. Patois, B. Nysten, A.J.J.M. van Breemen, G.H. Gelinck, D.M. de Leeuw, A. Marrani, Z. Hu, and A.M. Jonas, *Nanoscale Design of Multifunctional Organic Layers for Low-Power High-Density Memory Devices.* ACS Nano, **2014**, DOI: 10.1021/nn406503g.

18. Kassa, H.G., R. Cai, A. Marrani, B. Nysten, Z. Hu, and A.M. Jonas, *Structure and Ferroelectric Properties of Nanoimprinted Poly(vinylidene fluoride-ran-trifluoroethylene).* Macromolecules, **2013**. 46, 8569-8579.

19. Hu, Z., M. Tian, B. Nysten, and A.M. Jonas, *Regular Arrays of Highly Ordered Ferroelectric Polymer Nanostructures for Non-Volatile Low-Voltage Memories.* Nature Materials **2009**. 8, 62-7.

20. Hu, Z., G. Baralia, V. Bayot, J.-F. Gohy, and A.M. Jonas, *Nanoscale Control of Polymer Crystallization by Nanoimprint Lithography*. Nano Letters, **2005**. 5, 1738-1743.

21. Hu, Z. and A.M. Jonas, *Control of Crystal Orientation in Soft Nanostructures by Nanoimprint Lithography*. Soft Matter, **2010**. 6, 21-28.

22. Hu, Z., B. Muls, L. Gence, D.A. Serban, J. Hofkens, S. Melinte, B. Nysten, S. Demoustier-Champagne, and A.M. Jonas, *High-Throughput Fabrication of Organic Nanowire Devices with Preferential Internal Alignment and Improved Performance.* Nano Letters, **2007**. 7, 3639-3644.

23. Hlaing, H., X. Lu, T. Hofmann, K.G. Yager, C.T. Black, and B.M. Ocko, *Nanoimprint-Induced Molecular Orientation in Semiconducting Polymer Nanostructures.* ACS Nano, **2011**. 5, 7532-7538.

24. Kang, S.J., I. Bae, Y.J. Shin, Y.J. Park, J. Huh, S.-M. Park, H.-C. Kim, and C. Park, *Nonvolatile Polymer Memory with Nanoconfinement of Ferroelectric Crystals.* Nano Letters, **2010**. 11, 138-144.

25. Lutkenhaus, J.L., K. McEnnis, A. Serghei, and T.P. Russell, *Confinement Effects on Crystallization and Curie Transitions of Poly(vinylidene fluoride-co-trifluoroethylene).* Macromolecules, **2010**. 43, 3844-3850.

26. Serghei, A., W. Zhao, D. Miranda, and T.P. Russell, *Curie Transitions for Attograms of Ferroelectric Polymers.* Nano Letters, **2013**. 13, 577-580.

27. Bune, A.V., V.M. Fridkin, S. Ducharme, L.M. Blinov, S.P. Palto, A.V. Sorokin, S.G. Yudin, and A. Zlatkin, *Two-dimensional Ferroelectric Films.* Nature, **1998**. 391, 874-877.

28. Jin, X.Y., K.J. Kim, and H.S. Lee, *Grazing Incidence Reflection Absorption Fourier Transform Infrared (GIRA-FTIR) Spectroscopic Studies on the Ferroelectric Behavior of Poly(vinylidene fluoride–trifluoroethylene) Ultrathin Films.* Polymer, **2005**. 46, 12410-12415.

29. Serghei, A., J.L. Lutkenhaus, D.F. Miranda, K. McEnnis, F. Kremer, and T.P. Russell, *Density Fluctuations and Phase Transitions of Ferroelectric Polymer Nanowires.* Small, **2010**. 6, 1822-1826.

30. Lovinger, A.J., T. Furukawa, G.T. Davis, and M.G. Broadhurst, *Crystallographic Changes Characterizing the Curie Transition in Three Ferroelectric Copolymers of Vinylidene Fluoride and Trifluoroethylene: 1. As-Crystallized Samples.* Polymer, **1983**. 24, 1225-1232.

31. Li, G.R., N. Kagami, and H. Ohigashi, *The Possibility of Formation of Large Ferroelectric Domains in a Copolymer of Vinylidene Fluoride and Trifluoroethylene.* Journal of Applied Physics, **1992**. 72, 1056-1061.

32. Guo, D., I. Stolichnov, and N. Setter, *Thermally Induced Cooperative Molecular Reorientation and Nanoscale Polarization Switching*

Behaviors of Ultrathin Poly(vinylidene fluoride-trifluoroethylene) Films. Journal of Physical Chemistry B, **2011**. 115, 13455-13466.

33. Wu, Y., X. Li, Y. Weng, Z. Hu, and A.M. Jonas, *Orientation of Lamellar Crystals and its Correlation with Switching Behavior in Ferroelectric P(VDF-TrFE) Ultra-Thin Films.* Polymer, **2014**. 55, 970-977.

34. Sergei, V.K., N.M. Anna, C. Long Qing, and J.R. Brian, *Local Polarization Dynamics in Ferroelectric Materials.* Reports on Progress in Physics, **2010**. 73, 056502.

35. Kalinin, S.V., E. Karapetian, and M. Kachanov, *Nanoelectromechanics of Piezoresponse Force Microscopy.* Physical Review B, **2004**. 70, 184101.

36. Sharma, P., T.J. Reece, S. Ducharme, and A. Gruverman, *High-Resolution Studies of Domain Switching Behavior in Nanostructured Ferroelectric Polymers.* Nano Letters, **2011**. 11, 1970-1975.

37. Haubruge, H.G., X.A. Gallez, B. Nysten, and A.M. Jonas, *Image Analysis of Transmission Electron Micrographs of Semicrystalline Polymers: a Comparison with X-Ray Scattering Results.* Journal of Applied Crystallography, **2003**. 36, 1019-1025.

38. Pratt, W.K., *Digital Image Processing*. 1991, Wiley: New York.

Chapter 6

Conclusion and Perspectives

The functional properties of polymer materials open up new dimensions for some promising applications. Among these materials, ferroelectric polymers can be used for the fabrication of cheap and highly flexible non-volatile memory devices. In this context, this thesis contributed indirectly to the realization of such kind of memory devices by studying the structural, ferroelectric, and thermal behavior of nanodots of P(VDF-TrFE) copolymer. More specifically, in this thesis we fabricated ferroelectric nanostructures by nanoimprint lithography, developed appropriate structural and ferroelectric characterizations techniques, and made the link between the various imprinting process parameters and the subsequent structural and ferroelectric properties of P(VDF-TrFE).

Chapter 6

The relatively easy nanoimprint lithography technique (NIL) is extremely interesting to improve or control the crystal orientation of P(VDF-TrFE), besides to producing nanometer size patterns. Before this thesis, the improved crystallographic orientation was shown to result into a dramatic decrease of coercive field, which is a characteristic of a typical ferroelectric material, making them interesting for low-voltage memory applications. However, understanding the exact reasons for these interesting properties still needed extensive investigation of the correlation between the material, the imprinting processes, and subsequent structural or ferroelectric properties. In addition, the thermal stability of the fabricated nanostructures was not studied. In this context, the objectives of this thesis were then to make progress into these issues.

The first challenge in pursuing these objectives was fabricating nanostructures of various dimensions and finding appropriate characterization methodologies. Fabricating and characterizing nanometer sized structures is one technological challenge by itself; however, doing so on polymer materials was even more challenging. This is because most of the materials studied and techniques developed in the field of ferroelectric materials are essentially for traditional or conventional inorganic materials. Thus, producing nanometer sized ferroelectric structures and developing their characterization in our laboratory setting was one challenge and was also one of the targets of this thesis. Nanodots of P(VDF-TrFE) were fabricated by nano-imprint lithography (NIL), a technique that uses hard molds to emboss the heated polymer film under sufficient pressure. The nano-featured hard molds were produced as part of this thesis with another lithography technique, namely electron beam lithography (EBL). By optimizing some of the process parameters of EBL, hard SiO_2 NIL molds containing nanocavities of different lateral size and shape were prepared. The nanocavities of the hard molds were then used to create pillars of P(VDF-TrFE) copolymers.

Chapter 6

Standard atomic force microscopy (AFM) and Fourier-transform infrared (FTIR) microscopy were used to perform morphology and microstructure characterizations respectively. Furthermore, as an integral part of this thesis, we have developed and presented in detail the piezoresponse force microscopy (PFM) technique as a main tool for the local ferroelectric characterization of our samples.

Once the nanostructures were produced and the characterization tools were developed, we investigated in details the influence of nanoprocessing conditions during NIL on the final properties of P(VDF-TrFE) patterns. One typical parameter that we investigated was the nature of confinement which was achieved either by leaving or not a thin residual film connecting the pillars during the embossing procedure, while imprinting at a temperature between the Curie and meting point. For cavities of ~250 nm lateral size, the FTIR and AFM results revealed that fully confined (no residual layer) P(VDF-TrFE) pillars display a strong preferential orientation of their crystallographic *a* axis parallel to the Si substrate, and crystalline lamellae of significantly reduced length, compared to the partially confined (with residual layer) pillars of the same dimensions or those of continuous thin films. On the other hand, imprinting in complete confinement using bigger square cavities (550 nm lateral size) or in two dimensional confinement using lines molds (200 nm wide) results in an increase of the lamellar length, without strong preferential orientation compared to the annealed continuous ultrathin P(VDF-TrFE) sample. Interestingly, we found that if the sample is imprinted in the melt, the chain axis is found to be vertically aligned with respect to the substrate, ensuing a flat-on setting of the crystalline lamellae, with a clear loss of ferroelectric properties when probed with a vertical electric field.

Overall, the direction of the crystallographic axes with respect to the Si substrate and the length of crystalline lamellae were found to correlate with the ferroelectric properties of the resulting nanostructures. By probing the samples with a vertical electric field, the coercive field was found to decrease for nanopillars with the *a* axis strongly in-plane, which usually also leads to the *c* axis (chain) aligned more parallel to the substrate, and shorter lamellae length, such as in the samples imprinted below the melting temperature in three dimensional complete confinement and with smaller lateral size (250 nm). In this thesis, we have demonstrated that the optimal coupling between the polarization vector (perpendicular to the chain axis) and the electric field vector is the main reason for the lower value of coercive field. However, other factors were also proposed to contribute to the value of the coercive field such as the length of the lamellae. These detailed investigations clearly confirmed that the improvement of crystal orientation and subsequent ferroelectric properties of nanostructures is not only just because they were simply embossed; rather, it was because the nanoprocessing parameters like the degree of geometric confinement and also imprinting temperature played a crucial role in controlling the structural and ferroelectric properties of P(VDF-TrFE) copolymers. However, we are still not in a position to fully understand these correlations, nor indeed to provide a complete picture of crystal orientation. Further study by electron diffraction, or grazing angle synchrotron x-ray scattering (with a microspot), would be useful to progress in this description.

The thermal stability of the fully confined nanodots was then studied by investigating the Curie transition, which is characteristic to ferroelectric materials. The Curie transition temperatures were obtained by successively heating poled regions, followed by PFM mapping, and were compared with the bulk P(VDF-TrFE) sample. Our results demonstrated that the Curie transitions

of three dimensionally confined nanodots of diameter between 80 - 550 nm and height in the range of 60 - 130 nm are not significantly different from that of continuous thin films and bulk samples. Typically the smallest confined dots are equivalent to *ca.* 560 attograms of matter, corresponding to the volume of a cube of 68 nm side containing *ca.* 1500 chains only. We have also shown that the crystal orientation and therefore the ferroelectric properties of the smallest nanodots (80 nm wide) deviates from those of the 250 nm wide dots, indicating the presence of a possible critical size-related change in the ferroelectric properties of imprinted P(VDF-TrFE) nanostructures. However, the actual reason for the size-related change in the property of nanoconfined ferroelectric structures requires further investigation.

To sum up, our work illustrates how the nanoprocessing conditions are correlated to the structural and ferroelectric behavior of imprinted ferroelectric polymers, and how the thermal stability of these structures are not considerably affected during the embossing procedure. Obviously, this knowledge is significantly important for the fabrication of ferroelectric plastic memories of high flexibility, high density, and of low voltage. To mention one application, as an example, I have collaborated in a project to fabricate non-volatile memory diodes from nanoimprinted P(VDF-TrFE) and semiconductor layers. There is also an ongoing research in our group to fabricate FeFET memories from imprinted nanopatterns.

The future research work in the field of nanoimprint lithography and ferroelectric polymers is promising. For instance, imprinting even smaller size dots (below 80 nm) could be explored, since we have already shown that by decreasing the dot sizes from 250 nm to 80 nm, a dramatic change in the structural and ferroelectric properties of the nanostructures ensued. In other words, it could be interesting to investigate in detail even more confined dots to

clarify whether there are other size-related changes in their microstructure and ferroelectric properties, or not. In addition, the study of confinement could be extended to crystallized materials in embossing cavities of more complex shapes. However, the main challenge remains the fabrication of hard molds containing smaller cavity sizes and complex shapes. In this regard, block copolymer lithography technology could be optimized to achieve cavities of a few tens of nanometer. Alternatively, alumina (Al_2O_3) membranes with ordered nanoholes down to several tens of nanometers in size could be used as a mask to fabricate hard NIL molds, without the use of expensive lithography tools. NIL on other polymer resists is already shown to produce patterns of less than 10 nm in diameter. However, the adhesion problem between the mold and polymer films will be the most critical issue during NIL when smaller cavity size molds are used, since the surface to volume ratio increases.

In addition, adapting the NIL technique to study the effect of confinement in other functional polymers is also among the few perspectives of NIL. The PFM technique, which we used as reliable tool for investigating the local ferroelectric properties of our samples, could also be used to explore ferroelectricity in other new materials, both organic and inorganic ones. Overall, by combining the low-cost, high resolution, and high throughput nanostructure fabrication capabilities of NIL with the functional properties of polymers, potentially improved and ultimately interesting properties could be found in the future. The open cavities between the nanoimprinted pillars could also be filled with another polymer, which can produce new and potentially interesting functional properties from the combination of the two materials. For instance, the open cavities between our ferroelectric polymer nanostructures could be filled by either magnetic materials or semiconducting polymers, allowing us to achieve multiferroic layers or multifunctional organic layers which can be used for a variety of applications.

Appendix

Appendix A

A.1 Alternative Mold Fabrication

One of the initially experimented ways of obtaining molds of square nano-cavities was by a direct exposure of squares (Figure 3.3). The main advantage sought out of this route was to eliminate the lift-off procedure, after the metal evaporation step. However, aligning the metal source to cover only the top of unexposed resist was difficult, leading to the presence of non-uniform square cavities.

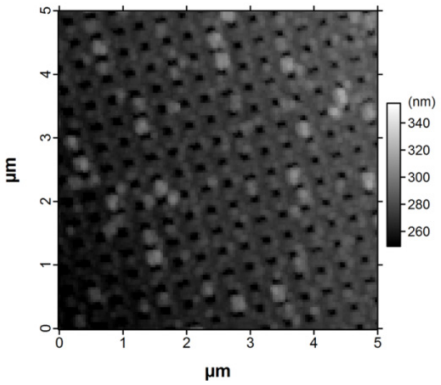

Figure A.1: AFM topography image of square cavity mold fabricated by electron beam lithography (EBL) achieved by irradiating designed square patterns as shown in Figure 3.3 (a).

Furthermore, with this kind of design, the protrusion of the imprinting features has the same height as the outside of the imprinting area, making it difficult to penetrate through the polymer/resist during the nano-embossing process. For this reason, only the second route was used to fabricate good quality and reliable molds.

A.2 EBL Dose Selection

Selecting the appropriate electron dose during the exposure step of EBL is quite critical on determining the size, shape, and quality of the final mold. We can see from Figure A.2 that dose of 140 $\mu C/cm^2$ is not large enough to irradiate and thus it did not isolate fully the unexposed islands whereas dose 220 $\mu C/cm^2$ produces over-exposure, and thus different shape than the originally designs square patterns.

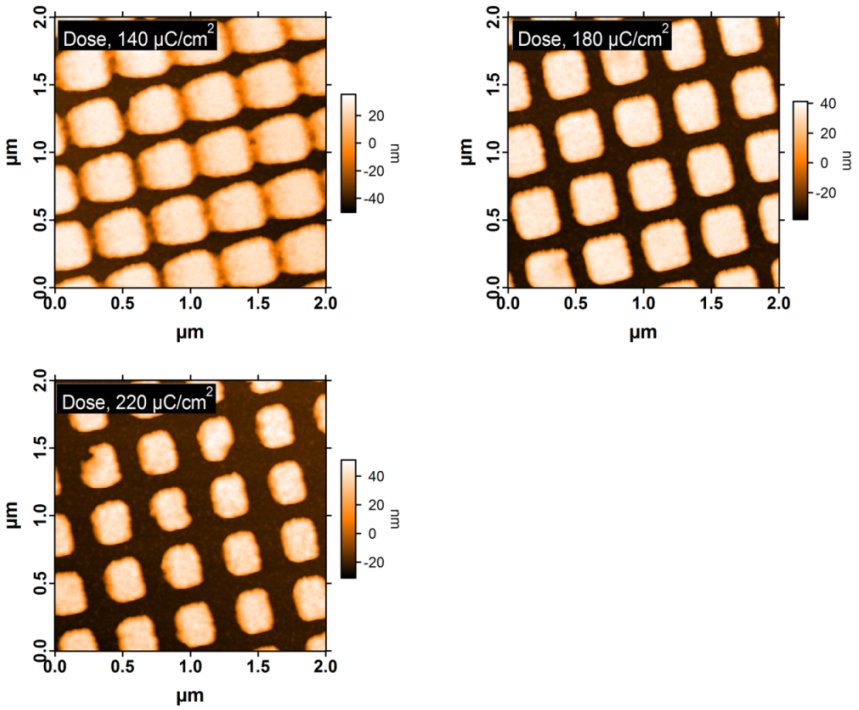

Figure A.2: AFM topography image of exposed resist after development of the resist with different electron exposure doses as given in each sub-panel.

On the other hand, exposing the intersecting lines with a dose of 180 µC/cm^2 gives reasonably good square patterns (Figure A.2), and this value of the dose is also used to perform EBL in our mold fabrication process.

A.3 EBL Development Time for mold resist process

Solving the shortcut problem during the development processes was solved by reducing the time of development in MIBK: IPA solvent from 90 seconds (Figure A.3,left) to 60 seconds (Figure A.3, right). Keeping the exposed patterns for a shorter time in the developer led to a shorter interaction time between the

solvent and the developed resist, preventing the creation of an undercut in the bottom resist layer, as confirmed by the AFM images of Figure A.3.

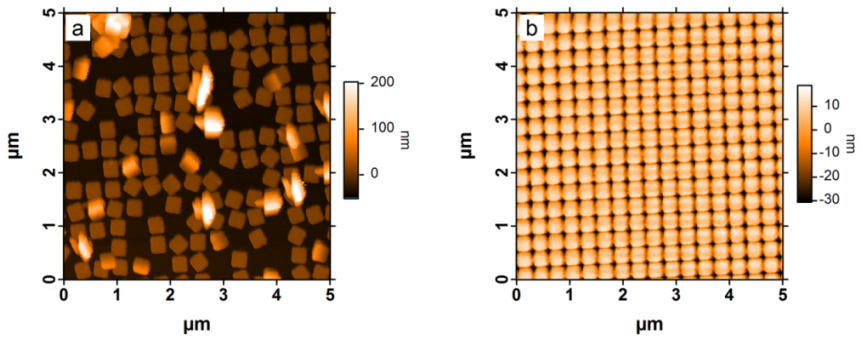

Figure A.3: AFM height image of developed bilayer resist for 90 seconds (left) and 60 seconds (right)

A.4 Block copolymer lithography (BCL) Hole Sizes

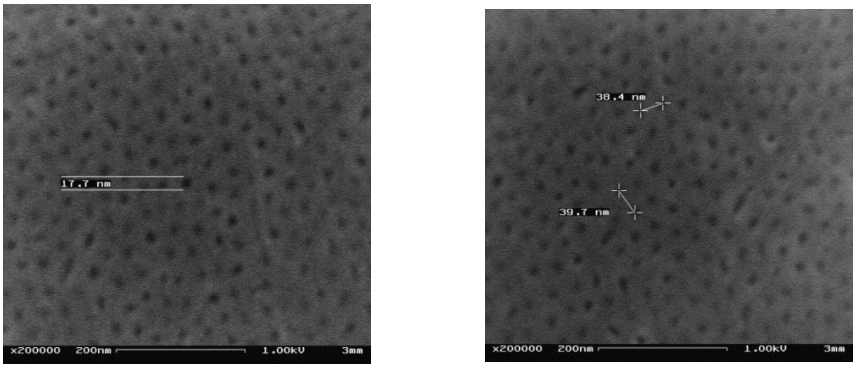

Figure A.4: SEM images of the solvent-annealed block copolymer thin film. The diameter of one random circle is ~18 nm and the separation distance between two circles is ~39 nm.

A.4 Piezoresponse hysteresis loops (PHLs): effect of repeated sweeping.

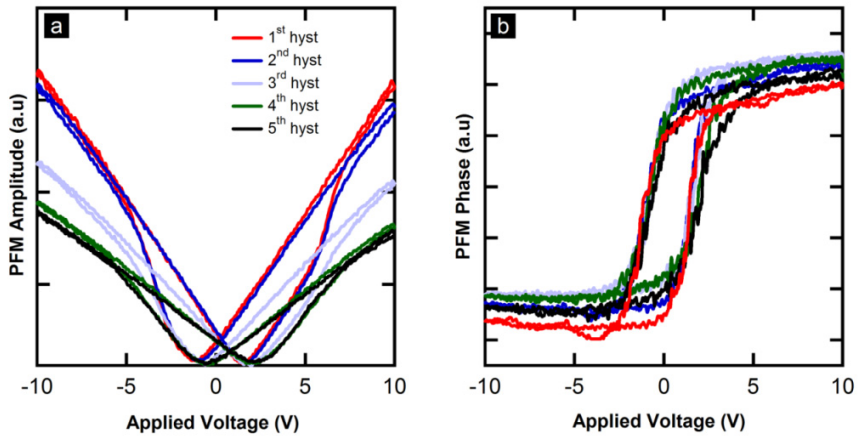

Figure A.5: PHL amplitude (a) and phase (b) as a function of symmetric bias voltage of an annealed continuous P(VDF-TrFE) thin film, showing identical hysteresis loops after the third symmetric sweeping voltage.

Appendix B

B.1 Atomic force microscopy (AFM) topography image of a sample imprinted in partial confinement.

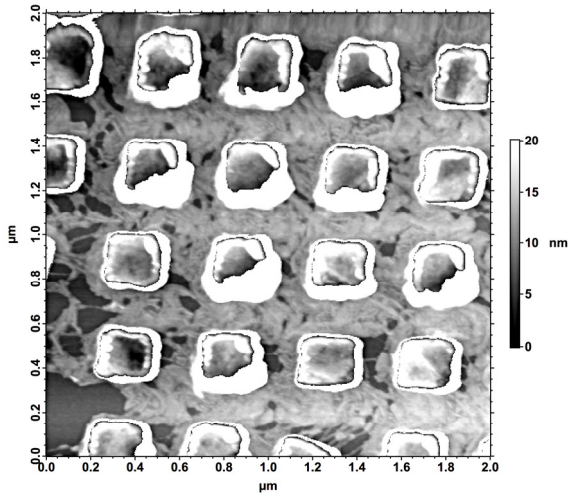

Figure B.1: AFM morphology of an array of $(250\ nm)^2$ imprinted P(VDF-TrFE) nanopillars in the partial confinement regime with 22 nm residual layer thickness (combined height image of the topmost and bottom part of the nanoimprinted structures, with 90 nm difference between the two gray levels). Note the partially-dewetted residual layer.

B.2 Piezoresponse Force Microscopy (PFM) hysteresis loop after imprinting from the melt.

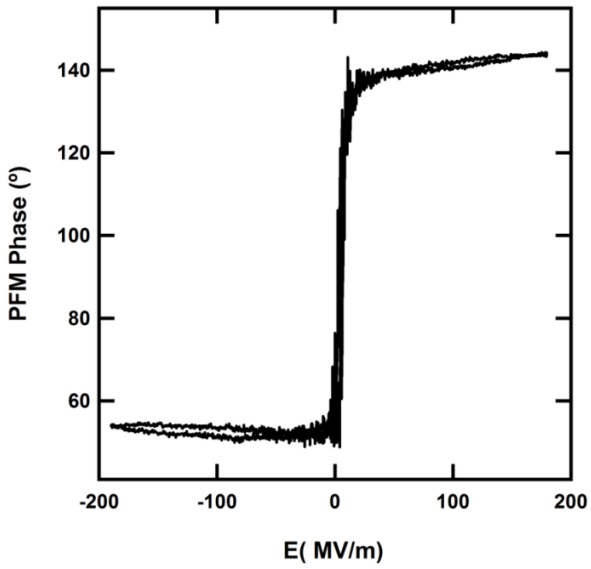

Figure B.2: Piezoresponse Force Microscopy (PFM) hysteresis loop (phase) of an array of fully confined P(VDF-TRFE) nanopillars of 250 nm side and 100 nm height, imprinted above the melting point at 160°C.